

DISSERTATION

submitted to the
combined Faculties for the Natural Sciences and for Mathematics
of the Ruperto-Carola University of Heidelberg, Germany
for the degree of
Doctor of Natural Sciences

Put forward by

Tanja Uhrig (geb. Gaa), M.Sc.
born in Schwetzingen

Oral examination: 17 June 2020

Quantitative Dynamic Contrast-Enhanced Perfusion MRI

-

A Phantom and in Vivo Study

Referees: Prof. Dr. Lothar R. Schad
Prof. Dr. Peter Bachert

Quantitative dynamische kontrastverstärkte Perfusions MRT - eine Phantom- und in Vivo Studie

Die Quantifizierung der Gewebepfusion mit der Magnetresonanztomographie (MRT) ist von großem medizinischen Wert für die Tumordiagnose, die Behandlungsplanung und die Therapiekontrolle. Ziel dieser Arbeit war es, die Durchführbarkeit der Perfusionsquantifizierung mit Hilfe der dynamischen kontrastverstärkten (DCE) MRT in Kombination mit pharmakokinetischer Modellierung zu evaluieren sowie Limitationen und Verbesserungen zu finden. Im ersten Teil wurde ein multimodales Perfusionsphantom entwickelt, das die menschliche Physiologie auf Kapillarebene nachahmt und den intra- und extravaskulären Raum simuliert. Dies ermöglicht die Anwendung eines Zwei-Kompartiment-Modells, das zu Perfusionsparametern führt, von denen unter anderem der Plasmafluss PF sowohl innerhalb einer Messreihe ($PF = (91 \pm 7) \text{ ml}/100 \text{ ml}/\text{min}$) als auch in der Wiederholung nach einer Woche ($PF = (91 \pm 26) \text{ ml}/100 \text{ ml}/\text{min}$) reproduzierbare Werte zeigt. Ein zuverlässiger Vergleich ist nicht nur zwischen MRT und DCE-Computertomographie (CT) ($PF = (94 \pm 53) \text{ ml}/100 \text{ ml}/\text{min}$), sondern auch zur alternativen MRT-Perfusionstechnik Arterial Spin Labeling (ASL) ($PF = (99 \pm 36) \text{ ml}/100 \text{ ml}/\text{min}$) möglich. Eine schnelle zeitliche Auflösung durch eine hohe Abtastrate, die für eine exakte Modellierung unabdingbar ist, wurde durch die Implementierung der parallelen Bildgebung erreicht und führte zu einer signifikanten Reduktion der Abweichung innerhalb einer Messung um 30%. Im zweiten Teil zeigte eine in vivo-Perfusionsstudie von Rektum Karzinomen, dass die bilaterale Auswahl der arteriellen Eingangsfunktion und die Verwendung von Zwei-Kompartiment-Modellen einen signifikanten Einfluss auf die Quantifizierung der Perfusionsparameter mit Abweichungen des PF von bis zu 30 ml/100 ml/min haben. Die Bedeutung der Auswahl des Gewebebereichs bei heterogenen Tumoren wurde gezeigt, da sich die Parameter innerhalb eines Tumors um bis zu 36% unterscheiden. Die Kombination der Ergebnisse aus der Phantom- und der Patientenstudie zeigt somit neue und vielversprechende Strategien zur Quantifizierung der DCE-MRI in der Zukunft auf.

Quantitative Dynamic Contrast-Enhanced Perfusion MRI - A Phantom and in Vivo Study

The quantification of tissue perfusion with magnetic resonance imaging (MRI) is of great medical value for tumor diagnosis, treatment planning and therapy control. The aim of this work was to evaluate the feasibility as well as to find limitations and improvements of perfusion quantification using dynamic contrast-enhanced (DCE) MRI in combination with pharmacokinetic modeling. In the first part, a multimodal perfusion phantom mimicking human physiology at capillary level and simulating intra- and extravascular space was developed. This enables the application of a dual compartment model leading to perfusion parameters of which among others the Plasma Flow PF shows reproducible values both within a series of measurements ($PF = (91 \pm 7) \text{ ml}/100 \text{ ml}/\text{min}$) and in the repetition after one week ($PF = (91 \pm 26) \text{ ml}/100 \text{ ml}/\text{min}$). A reliable comparison not only between MRI and DCE computer tomography (CT) ($PF = (94 \pm 53) \text{ ml}/100 \text{ ml}/\text{min}$), but also to the alternative MRI perfusion technique Arterial Spin Labeling (ASL) ($PF = (99 \pm 36) \text{ ml}/100 \text{ ml}/\text{min}$) is applicable. Fast temporal resolution through a high sampling rate, indispensable for exact modeling, was achieved by the implementation of parallel imaging and led to a significant reduction of the intra measurement deviation by 30%. In the second part, an in vivo perfusion study of rectal carcinomas showed that the bilateral selection of the arterial input function and the use of dual compartment models have a significant influence on the quantification of perfusion parameters with deviations of the PF of up to 30 ml/100 ml/min. The importance of tissue ROI selection in heterogeneous tumors has been shown, as the parameters within a tumor differ by up to 36%. The combination of the findings of the phantom and the patient study reveals new and promising strategies for quantifying DCE-MRI in the future.

Contents

1	Introduction	1
2	Theoretical Background	7
2.1	Nuclear Magnetic Resonance	7
2.1.1	Spin and Magnetic Moment	8
2.1.2	Zeeman Effect	9
2.1.3	Macroscopic Magnetization	9
2.1.4	Radio Frequency Excitation	11
2.1.5	Relaxation	12
2.1.6	Bloch Equations	13
2.1.7	Signal Detection	14
2.2	Magnetic Resonance Imaging	15
2.2.1	Spatial Encoding	15
2.2.2	K-Space Sampling	17
2.2.3	Standard Acquisition Techniques	19
2.2.4	Signal and Contrast	21
2.3	Computer Tomography	22
2.3.1	X-Rays	23
2.3.2	Photon Matter Interaction	23
2.3.3	Signal Acquisition	25
2.3.4	Image Reconstruction and Hounsfield Units	26
2.4	Perfusion Imaging	27
2.4.1	Tissue Perfusion	28
2.4.2	Tracer Kinetics	28
2.4.3	Dynamic Contrast Enhanced Techniques	31
2.4.4	Arterial Spin Labeling	31
3	Materials and Methods	35
3.1	DCE MR and CT Imaging	35
3.1.1	MR Scanners and Coils	35
3.1.2	MR Sequences	37
3.1.3	MR Contrast Agent	40
3.1.4	CT Scanner and Sequence	41
3.1.5	CT Contrast Agent	42
3.1.6	Application of Perfusion Models	43
3.2	DCE Perfusion Phantom Study	46
3.2.1	Phantom Design	46

3.2.2	Imaging Protocol	49
3.2.3	Feasibility	49
3.2.4	Reproducibility	51
3.2.5	Temporal Resolution and PAT	51
3.2.6	Application for ASL	53
3.2.7	Application for DCE CT	54
3.3	DCE in Vivo Study in Rectal Cancer Patients	55
3.3.1	Patients	55
3.3.2	Data Acquisition	55
3.3.3	Bilateral Blood Supply and AIF Selection	56
3.3.4	Compartment Models and Model Free Approach	58
3.3.5	2D and 3D Evaluation	58
3.3.6	Comparison DCE CT	59
4	Results	61
4.1	Contrast Agent Calibration	61
4.2	DCE Perfusion Phantom Study	63
4.2.1	Phantom design	63
4.2.2	Feasibility	63
4.2.3	Reproducibility	64
4.2.4	Temporal Resolution and PAT	68
4.2.5	Application for ASL	68
4.2.6	Application for DCE CT	69
4.3	DCE in vivo Study in Rectal Cancer Patients	74
4.3.1	Bilateral Blood Supply and AIF Selection	74
4.3.2	Compartment Models and Model Free Approach	79
4.3.3	2D and 3D Evaluation	84
4.3.4	Comparison DCE CT	84
5	Discussion	87
5.1	DCE Perfusion Phantom Study	87
5.2	DCE in Vivo Study in Rectal Cancer Patients	92
6	Conclusion	99
	List of Figures	101
	List of Tables	103
	Acronyms	104
	References	107

Introduction 1

Magnetic resonance imaging (MRI) is a powerful non-invasive and radiation-free medical imaging technique known for its excellent soft tissue contrast. Its versatile contrast-creating mechanism has made a variety of MRI imaging techniques such as functional imaging possible. In contrast to morphological imaging, which provides information about anatomy, functional imaging can represent tissue physiology such as diffusion, oxygenation and perfusion. The development of new scanner hardware and faster imaging methods in recent years have made functional imaging even more feasible not only for static body regions such as the the brain, but also for abdominal imaging, despite organ movement.

This thesis deals with the technique of perfusion imaging in MRI. Perfusion generally describes the process of supplying oxygen and nutrients to the capillary bed of a particular tissue and supports the removal of metabolic waste products. Thus, it provides information about the condition of the organ and often indicates impaired function or vascular diseases. Possible clinical applications of perfusion measurements include ischemia, cardiac infarction or epilepsy and, as it detects changes in blood flow and blood supply, targeting of tumor areas. Although several techniques for measuring perfusion have been developed, they are all based on the tracking and monitoring of a specific indicator or tracer in the form of a bolus. For instance, single-photon emission computed tomography (SPECT) and positron emission tomography (PET) use tracers that emit photons and positrons, iodinated contrast agents (CA) are used to change the beam attenuation in the CT. However, the methods mentioned above include either the use of radioactive substances or X-rays.

Tissue perfusion and permeability can be measured non-invasively by dynamic contrast enhanced (DCE) MRI ([Brix et al., 1991](#)). A bolus of paramagnetic CA is injected as a tracer for the determination of hemodynamic parameters by analyzing the signal variation with respect to time. This method enables the determination of quantitative microvascular parameters such as blood flow, blood volume, transit time and the permeability from arteries into tissue ([Koh et al., 2011](#)). These parameters can then support the differentiation of malignant and benign tumors ([DeVries et al., 2014](#); [Oberholzer et al., 2013](#)) or the evaluation of tumor response after therapy and also possibly predict therapy outcome ([Ceelen et al., 2006](#); [Zahra et al., 2007](#)).

However, quantitative dynamic perfusion measurements are not yet fully established in the clinical routine. Reproducibility and comparison of quantitative parameters is difficult due to non-standardized examinations and data analysis (Zöllner et al., 2016a). For this reason, quantification is often omitted for a faster but less powerful qualitative or semiquantitative evaluation method. This is regrettable precisely because no or hardly any additional measuring time would be required for a quantitative evaluation of the necessary data, whereas the information content of the individual measurement could be massively improved.

The steps required are the rapid measurement of time-variable changes in T_1 relaxation times and the use of kinetic modeling processes with accurate determination of the arterial information, analysis software that allows the input of various MRI devices and validated statistical tools for the evaluation of tissue heterogeneity (Khalifa et al., 2014). Highly specific approaches to solve some of these challenges have already been published. However, most of them are of theoretical nature (Yankeelov et al., 2005), validated by simulation (Ning et al., 2018) or have not been integrated into the clinical process but have only been considered in an isolated setting (Otazo et al., 2010). Furthermore, the lack of a gold standard for the determination of perfusion values makes the evaluation of new methods difficult. PET scanning with ^{15}O -labeled water (Detre et al., 1992) so far represents a form of gold standard. However, due to its high invasiveness caused by the radioactive tracer and its short half-life, it is rarely used in practice.

Research in this thesis was pursued in two directions in order to investigate the feasibility of quantification, detect limitations and develop improvements. In the first part, a perfusion phantom setup was developed and in the second part, a retrospective rectum cancer perfusion study was analyzed.

Part 1: Perfusion phantom setup

Quantification of perfusion data from DCE MRI is of high interest e.g. for comparison between patients, different measurements and machines. Studies to validate new methods need to be carried out. However, due to the administration of CA, volunteer studies are ethically difficult to realize. In patients, previous diseases lead to a lack of ground truth data, which makes comparative measurements difficult. In previous studies, simulations (Zwick et al., 2010) and ex-vivo measurements with organs (Sauerbrey et al., 2014) were done. However, these approaches either do not provide experimental data or the measurement setup is relatively complicated and reproducibility is limited. Therefore, phantoms are employed to investigate the reproducibility of perfusion parameters by imitating tissue on a capillary level. Compared to previously presented phantoms modeling solely the capillaries (Gaass et al., 2017; Knight et al., 2017), it is proposed to use of a dialysis filter that has a semipermeable capillary membrane which can be crossed by MR CA in this study. This way, a dual compartment model (2CM) that represents anatomical conditions more accurately by simulating intravascular and extravascular space can be applied.

The aim is to establish a quantitative, reproducible workflow to ensure comparison and standardization of perfusion measurements using DCE MRI.

Initially the feasibility of the phantom was tested. The material properties were examined during the measurement to ensure that the CA can move as expected. The distribution of CA in the experimental setup was observed with the aim to determine arterial input functions (AIF) and tissue signal curves.

Fitting the dual CM on the perfusion signal allows the pixel wise calculation of perfusion maps describing the plasma flow (PF), the plasma volume (PV) and the mean transit time (MTT). Furthermore, the permeability, i.e. the exchange characteristics between the two chambers across the membrane in the form of extraction fraction (EF) and permeability surface area product (PSAP) can be investigated and the calculation accuracy can be determined. In contrast to other phantoms, the setup offers the possibility to repeat the measurement several times consecutively during a measurement cycle and after several days without any changes in the tissue structure. The reproducibility of these two scenarios was evaluated using the perfusion and permeability maps.

The quality of the AIF and the goodness of the CM fit is severely affected by the temporal resolution T_s of signal sampling, especially when applying pharmacokinetic models. It is commonly recommended that T_s should be smaller than 10 s ([Shukla-Dave et al., 2019](#)); yet, no consensus on the optimal T_s exists. In order to increase the sampling resolution, accelerated parallel acquisition technique (PAT) can be used. However, a compromise between acquisition speed and image quality must always be found, since the signal to noise ratio (SNR) decreases with greater parallelization ([Li et al., 2012](#)). It was therefore examined in more detail how parallel imaging affects the two opposite effects of higher sampling rate and deterioration due to SNR loss on the calculation of the perfusion parameters.

A comparison with other perfusion measurement methods was pursued as an alternative to the missing gold standard. The phantom construction was chosen to ensure suitability for Arterial Spin Labeling (ASL), an alternative technique to determine the PF in MRI ([Petersen et al., 2006](#)), and dynamic contrast enhanced Computer Tomography (CT).

ASL does not require an external administration of CA. Therefore its use can be beneficial in certain circumstances, e.g. intolerance of CA. In fact, ASL is indeed often used for brain measurements, but much more complicated to use in the remaining body parts. A comparability of both the DCE MRI and ASL technique would be particularly useful for follow-up measurements, but is not yet clinically available.

Also dynamic contrast enhanced computer tomography (CT) combined with tracer kinetic modeling allows for the determination of quantitative perfusion parameters. CT perfusion measurements have not played a relevant role in the past due to high dose levels. However, new technical developments are now making them more and more conceivable. Increased speed of data acquisition as

well as modern imaging technologies both are contributing to the reduction of the required radiation dose (Miles et al., 2012). The advantage of CT perfusion values is their robustness and reproducibility due to the linear signal intensity characteristics of the Hounsfield (HU) scale. For financial reasons or due to incompatibilities with CA or other pathologies, the CT and MRI measurements are sometimes interchanged for the same diagnosis in everyday clinical practice. A comparability between the two modalities is, however, not yet given. In a few studies, results were compared retrospectively, however no standardized procedures to acquire and evaluate MRI and CT data are used (Eastwood et al., 2003; Fieselmann et al., 2011). Comparisons have also been made in phantom studies, but few with quantitative evaluation using a phantom with two compartments (Otton et al., 2013). Since these are particularly suitable for the description of the tissues physiology, the perfusion phantom was used in CT where feasibility and reproducibility was investigated and in a last step compared with the results obtained in the MR measurements.

Part 2: Retrospective Rectum Cancer Perfusion Study

DCE perfusion measurements in patients with rectal cancer are employed in clinical routine to acquire pretreatment scans (DeVries et al., 2001). It has achieved broad acceptance not only for local staging of primary rectal cancer prior to treatment but also to predict treatment outcome (Attenberger et al., 2014). Recently, several authors have demonstrated the additional value of functional MRI parameters comprising perfusion parameters such as PF or MTT (Koh et al., 2013). However, such quantitative analysis underlies the well-known issues related to perfusion imaging (Oberholzer et al., 2013), especially with regard to correct modeling of the pharmacokinetics.

Particularly, selecting an adequate AIF is critical to obtain accurately calculated parameters (Calamante, 2013). The selection of the AIF becomes essential for rectum imaging since on the one hand both left and right iliac arteries supply the rectum and thus the tumor with blood, contributing to the perfusion. On the other hand stenosis in these arteries is commonly reported, affecting physiology and thus blood supply. Recent studies neglected this problem and rather just selected either left or right supplying vessel in one of the rectum supplying arteries or its branches in their analysis (Attenberger et al., 2014), (Koh et al., 2013), (Oberholzer et al., 2013). The influence of selecting the AIF in either left or right iliac artery on parameters obtained by perfusion analysis was investigated with three different pharmacokinetic approaches: a model independent algorithm, and two different CM.

DCE MRI combined with tracer kinetic modeling allows for the determination of quantitative perfusion parameters. Either semi quantitative analysis (Kremser et al., 2007), the model free deconvolution algorithm (Østergaard et al., 1996b) or the Tofts-model (Tofts, 2010) has been applied in literature, the latter one is most widely used in clinical routine (Ceelen et al., 2006; Tong et al., 2015). However, these approaches either do not model the structure of the tissue (deconvolution) or are limited by not directly providing values for PF and MTT (Tofts model). In contrast, multi-compartment models can fulfill

these requirements ([Sourbron, 2010](#)). The selection of an adequate pharmacokinetic model is crucial to derive the correct perfusion information from the image data to understand microvascular physiology ([Donaldson et al., 2010](#)). Currently, there is no systematic method for the identification of the most specific model with regard to clinical usefulness ([Ingrisch and Sourbron, 2013](#)). It is therefore important to compare existing models and assess their quality in describing the acquired signal. The aim of this study was to compare the fast deconvolution approach (FD) ([Østergaard et al., 1996b](#)) as a model free method to two different compartment models, the dual compartment uptake model (2CU) and the dual compartment exchange model (2CX) with regard to the impact on perfusion parameters.

Tumor tissue is often heterogeneous, the form of heterogeneity is decisive for the further therapy decision ([Sanghera et al., 2012](#)). Yet, most perfusion MRI studies currently focus exclusively on one specific slice of the tumor for parameter calculation ([Koh et al., 2013](#)), differing pathologies in other parts of the tumor may not be detected. Furthermore, the choice of one particular slice depends on the performing physician. Luckily, 3D perfusion MR imaging data is often already available enabling volume-resolved quantitative parameters mapping. In the aim of a better treatment prediction, the influence of volume based evaluation of perfusion parameters of the rectal tumor compared to the data obtained by selecting a single slice was investigated.

For analyses on patient data the same issues apply as described above for phantom measurement: the lack of a gold standard. DCE CT is applicable to rectal cancer patients as shown in several studies ([Koh et al., 2013](#); [Sahani et al., 2005](#)). Thus a retrospective study in which CT perfusion data were also acquired within a comparable time frame was chosen for this thesis. These were evaluated as similarly as possible to achieve a comparison in quantification with DCE imaging of the rectum.

Theoretical Background 2

Perfusion imaging in this thesis is performed with the imaging modalities MRI and CT. Both enable quantitative measurements of morphological and functional tissue characteristics providing information about the tissue physiology. This enables the examination and differentiation of diseased tissue and subsequent therapy planning. MRI is based on the principle of Nuclear Magnetic Resonance (NMR), which will be explained in the first part of the following section. NMR signal generation can be understood using the quantum mechanical description of spins and nuclear magnetism. The signal is created by stimulating the spin system with matching radiofrequency waves in a magnetic field. This procedure has been further developed to obtain medical information from the tomographic imaging technique MRI by spatially encoding the origin of the measured signals. The fundamentals of MR sequences for signal generation and location as well as contrast generation are explained in the second part. In CT, on the other hand, the different absorption characteristics of X-rays in various tissues in the body are used to generate tomographic images using complex reconstruction techniques which are introduced thereafter. The two imaging techniques offer specific advantages and disadvantages in both general and perfusion imaging. The background of perfusion imaging, various techniques and the standard workflow in both modalities are briefly introduced in the last part of this theoretical background chapter.

2.1 Nuclear Magnetic Resonance

NMR is based on interactions of protons and other nuclei with a magnetic field. These nuclei possess an intrinsic nuclear spin, a fundamental physical property used for signal acquisition. Showing this in an experiment, [Bloch et al. \(1946\)](#) and [Purcell et al. \(1946\)](#) were honored with the Nobel Prize in Physics in 1952. All nuclei with nuclear spin different from zero can be used for signal acquisition in principle, however the high occurrence of hydrogen in the body and the physical properties of its nucleus make it the most relevant one for MRI in the clinical routine. This section gives an overview over the basic principles of NMR. The reader is referred to the work of [Abragam \(1961\)](#), [Haacke et al. \(1999\)](#) and [Levitt \(2001\)](#) for a more detailed description.

2.1.1 Spin and Magnetic Moment

Atomic nuclei are composed of protons and neutrons. These elementary particles possess a quantum property called spin, which is an intrinsic form of angular momentum. The respective quantum number is $s = 1/2$. If a nucleus has an odd number of protons and/or neutrons, their spins do not cancel each other out. The nuclear spin \vec{I} is then unequal to zero. The spin is proportional to a magnetic moment

$$\vec{\mu} = \gamma \vec{I} \quad (2.1.1)$$

with the proportionality constant γ being the nucleus-specific gyromagnetic ratio

$$\gamma = \frac{g_I \mu_N}{\hbar}. \quad (2.1.2)$$

Here, g_I is the element specific gyromagnetic factor or Landé factor and \hbar the reduced Planck constant $\hbar = h/2\pi = 1.0545 \cdot 10^{-34}$ Js. The nuclear magneton μ_N can be expressed as

$$\mu_N = \frac{e\hbar}{2m_p} \quad (2.1.3)$$

with the elementary charge $e = 1.602 \cdot 10^{-19}$ C and the proton mass $m_p = 1.67 \cdot 10^{-27}$ kg. Due to the very high natural occurrence in the human body and the large gyromagnetic ratio of $\gamma = 267.51 \cdot 10^6 \frac{\text{rad}}{\text{s}\cdot\text{T}}$ of the hydrogen nucleus, it has a good sensitivity and thus offers ideal conditions in NMR experiments.

As the nuclear spin corresponds to an angular momentum, its quantum mechanical operator \hat{I} fulfills the commutation rules

$$[\hat{I}_i, \hat{I}_j] = i\hbar \epsilon_{ijk} \hat{I}_k, \quad (2.1.4)$$

$$[\hat{I}_i, \hat{I}^2] = 0 \quad (2.1.5)$$

with ϵ_{ijk} being the permutation or Levi-Civita symbol. Since \hat{I}_z and \hat{I}^2 interchange, mutual eigenstates $|I, m\rangle$ exist and form a complete basis which is solely determined by the two quantum numbers I and m . The derived eigenequations are

$$\hat{I}_z |I, m\rangle = \hbar m |I, m\rangle \quad (2.1.6)$$

$$\hat{I}^2 |I, m\rangle = \hbar^2 I(I+1) |I, m\rangle. \quad (2.1.7)$$

The nuclear spin quantum number I describes the permitted spin states of the nucleus that are $I = 0, \frac{1}{2}, 1, \frac{3}{2}, \dots$ and for hydrogen it is $I = 1/2$. The magnetic quantum number m describes the spatial orientation in respect to the z-axis with the values $m = -I, -I+1, \dots, I-1, I$. Consequently, the values $m = -1/2$ and $m = +1/2$ can be derived for hydrogen. Thus, for each spin state I there are generally $(2I+1)$ discrete states of m . Protons therefore have two spin states: the spin up $|1/2, +1/2\rangle$ and the spin down $|1/2, -1/2\rangle$ state. Without an external magnetic field, these eigenstates $|I, m\rangle$ are degenerated, i.e. they share the same energy level.

2.1.2 Zeeman Effect

If a magnetic flux is present, the degeneration is resolved and the energy states can be distinguished. Provided that the nomenclature used in NMR refers to magnetic flux density as magnetic field, the interaction of the nuclear spin with the applied magnetic field can be described by the following Hamiltonian

$$\hat{H} = -\hat{\mu}\vec{B} = -\gamma\hat{I}\vec{B}. \quad (2.1.8)$$

If we assume a constant magnetic field in the z-direction $\vec{B} = (0, 0, B_0)$, as it is commonly the case in an NMR experiment, this simplifies to

$$\hat{H}_z = -\gamma\hat{I}_z B_0. \quad (2.1.9)$$

With the previously introduced eigenvalue equation in [Equation 2.1.6](#) and the time-independent Schrödinger equation

$$\hat{H}|I, m\rangle = E_m|I, m\rangle, \quad (2.1.10)$$

the energy states E_m can be calculated

$$E_m|I, m\rangle = -\gamma\hat{I}_z B_0|I, m\rangle = -m\hbar\gamma B_0|I, m\rangle. \quad (2.1.11)$$

The formation of the two separated energy levels $E_{+1/2}$ (parallel to \vec{B}_0) and $E_{-1/2}$ (antiparallel to \vec{B}_0) due to an external magnetic field is called the Zeeman effect, depicted in [Figure 2.1](#). The difference in energy between the two energy states in the hydrogen atom is

$$\Delta E_m = E_{-1/2} - E_{+1/2} = \gamma\hbar B_0. \quad (2.1.12)$$

The size of the energy gap between the two states is thus proportional to the applied magnetic field B_0 . To induce a transition between the higher and lower energy state, a photon with the energy $\hbar\omega$ must be absorbed or emitted according to the Planck Einstein relation $E = \hbar\omega$. Electromagnetic waves orthogonal to the magnetic field B_0 must hence be applied with a frequency that satisfies the following equation

$$\hbar\omega_0 = \gamma\hbar B_0. \quad (2.1.13)$$

This leads to the equation for the Larmor frequency

$$\omega_L = \omega_0 = \gamma B_0. \quad (2.1.14)$$

It is proportional to the magnetic field strength and the gyromagnetic ratio and at $B_0 = 3$ T the Larmor frequency amounts to $f_L = \frac{\omega_L}{2\pi} = 127.7$ MHz.

2.1.3 Macroscopic Magnetization

In order to obtain a measurable NMR signal, a large quantity of protons is regarded instead of a single one. In a thermal equilibrium, the population

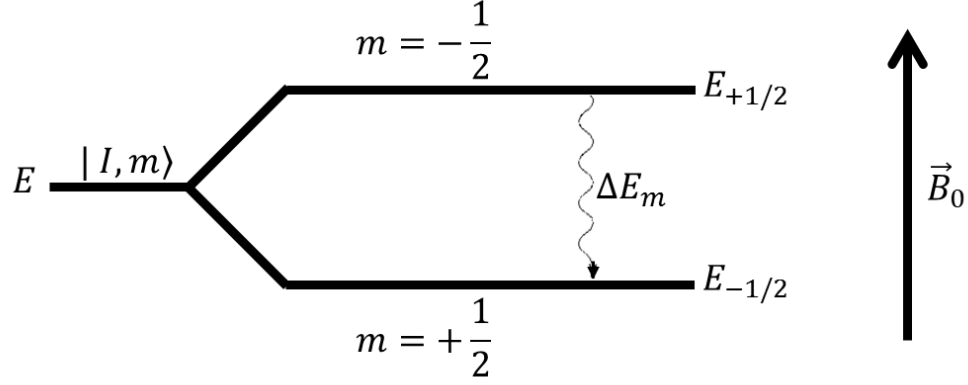


Figure 2.1: Zeeman energy splitting in a hydrogen atom. By applying an external magnetic field B_0 , the previously degenerated energy levels are divided into two states $E_{+1/2}$ and $E_{-1/2}$. The spin up and spin down state are formed with an energy difference ΔE_m , which can be overcome by photon absorption or emission proportional to the Larmor frequency ω_L .

probability p_m of the corresponding Zeeman energy states is described by the Boltzmann statistics

$$p_m = \frac{1}{Z} e^{-\frac{E_m}{k_B T}}, Z = \sum_{m=-I}^I e^{-\frac{E_m}{k_B T}} \quad (2.1.15)$$

with $k_B = 1.38 \cdot 10^{-23}$ J/K being the Boltzmann constant. In the next step, the probabilities for $m = \pm 1/2$ and thus the number of spins parallel n_{\uparrow} and antiparallel n_{\downarrow} to the static field, can be calculated

$$\frac{n_{\downarrow}}{n_{\uparrow}} = e^{\frac{\Delta E}{k_B T}} = e^{-\frac{\hbar \gamma B_0}{k_B T}}. \quad (2.1.16)$$

It is remarkable that at room temperature and a field strength of $B_0 = 3$ T only 2 in 10^5 spins generate a surplus in the parallel state. Solely this small difference in the occupation probabilities produces the net magnetization M_0 , aligned along the external magnetic field, which causes the NMR signal. This magnetization is described as the average magnetic dipole moment density in a certain volume V , which can then be transformed with the use of [Equation 2.1.5](#) to

$$\vec{M} = \frac{1}{V} \sum_{\text{protons}} \hat{\mu}_z = \frac{1}{V} \sum_{n=1}^N \gamma \langle \hat{I}_z \rangle_n = \frac{N \gamma \hbar}{V} \sum_{m=-I}^I m p_m. \quad (2.1.17)$$

At body temperatures, $k_B T \gg \hbar \omega_0$ can be assumed. Using this assumption, the exponential term in [Equation 2.1.15](#) can be expanded in a Taylor series and Curie's law is obtained

$$M_0 \approx \frac{N}{V} B_0 \frac{I(I+1) \gamma^2 \hbar^2}{3 k_B T}. \quad (2.1.18)$$

M_0 is the net magnetization available for the NMR signal. It is hence proportional to the field strength of the main magnetic field B_0 , the spin density $\rho = N/V$, and to the square of the gyromagnetic ratio γ .

2.1.4 Radio Frequency Excitation

Nuclear spins in the magnetic field B_0 are precessing with the Larmor frequency and so does their magnetic moment

$$\frac{d\hat{\mu}}{dt} = \hat{\mu} \times \gamma \vec{B}_0. \quad (2.1.19)$$

However, looking at a spin ensemble in thermal equilibrium, the spins are orientated in random directions, showing only a small net magnetization in z-direction. All other parts add up to zero since the spins have no phase coherence and thus statistically cancel each other out. There is no transverse magnetization and in this condition it is not possible to measure an NMR signal.

An electromagnetic high frequency field, the so called \vec{B}_1 -field or radio frequency (RF)-field can be applied. It is perpendicular to the net magnetization, which leads to an energy transfer to the spin system by resonant absorption with the Larmor frequency. Referring to [Equation 2.1.19](#), the total magnetization can then be described by

$$\frac{d\vec{M}}{dt} = \vec{M} \times \gamma (\vec{B}_0 + \vec{B}_1). \quad (2.1.20)$$

Given that the applied high frequency field is a left circularly polarized RF-field with frequency ω_1 in the x-y-plane

$$\vec{B}_1(t) = \begin{pmatrix} B_1 \cos(\omega_1 t) \\ -B_1 \sin(\omega_1 t) \\ 0 \end{pmatrix} \quad (2.1.21)$$

it leads to

$$\frac{d\vec{M}}{dt} = \vec{M} \times \gamma \begin{pmatrix} B_1 \cos(\omega_1 t) \\ -B_1 \sin(\omega_1 t) \\ B_0 \end{pmatrix}. \quad (2.1.22)$$

The precession of magnetization around the respective magnetic fields \vec{B}_0 and \vec{B}_1 generates a complicated equation of motion, which can be simplified by introducing a new reference system. For this purpose a rotating frame with the direction of the constant magnetic field \vec{B}_0 as rotation axis and the rotation frequency $\Omega = (0, 0, -\omega_1)$ is most convenient

$$\frac{d\vec{M}'}{dt} = \vec{M}' \times \gamma \begin{pmatrix} B_1 \\ 0 \\ B_0 - \frac{\omega_1}{\gamma} \end{pmatrix} = \vec{M}' \times \gamma \vec{B}_{\text{eff}}. \quad (2.1.23)$$

This formula shows that by selecting $\omega_1 = \gamma B_0$ for the frequency of the applied \vec{B}_1 -field, the influence of the \vec{B}_0 -field disappears. There is now a precession around \vec{B}_1 only. In order to tilt the magnetization vector by a specific angle and thus generate a magnetization in the transverse plane, the RF-pulse must be applied with a certain strength and duration. This angle is called the flip angle α

$$\alpha = \int_0^t \gamma B_1 dt'. \quad (2.1.24)$$

2.1.5 Relaxation

The magnetization vector can be divided into a longitudinal component M_z and a transverse component M_{xy} . The magnetization is only manipulated as long as the B_1 -field is switched on. When this field is deactivated, the excitation stops and the magnetization returns to its initial equilibrium state of the lowest possible energy. During this time, the spins interact with their environment and the surrounding spins leading to two effects: The spin-lattice relaxation, also referred to as T_1 or longitudinal relaxation and the spin-spin relaxation, also referred to as T_2 or transverse relaxation.

Spin-Lattice Relaxation

To return to the initial value M_0 in thermal equilibrium, an energy transfer of the spins through interaction in the form of vibrations and rotations with the surrounding atoms of the proton takes place

$$\frac{dM_z}{dt} = \frac{1}{T_1} \cdot (M_0 - M_z). \quad (2.1.25)$$

The differential equation can be solved by an exponential function with the relaxation constant T_1

$$M_z(t) = M_z(0) \cdot e^{-t/T_1} + M_0 \cdot (1 - e^{-t/T_1}). \quad (2.1.26)$$

The T_1 relaxation time depends on the energy transport between spins and the tissue environment. Therefore it is varying in different kinds of human tissue. Furthermore, it is influenced by the magnetic field strength B_0 , as the latter is related to the Larmor frequency of the spins, which determines the effectiveness of the energy exchange between spins and the environment. Typical values can be found in [Table 2.1](#).

Spin-Spin Relaxation

Directly after the excitation pulse, the spins are phase coherent, resulting in a magnetization component M_{xy} in the transverse plane. Each spin is exposed to a locally dependent magnetic field, composed of applied B_0 -field and magnetic moments of other atoms in the surrounding area. These slight differences in the magnetic field randomly changing over time cause the resonant frequency of the spins to shift minimally, resulting in an irreversible dephasing of them. The magnetization component M_{xy} thus decreases with time which can be described similarly to the spin-lattice relaxation by

$$\frac{d\vec{M}_{xy}}{dt} = -\frac{1}{T_2} \cdot \vec{M}_{xy}. \quad (2.1.27)$$

The solution is an exponential function decay with the spin-spin relaxation time T_2

$$\vec{M}_{xy}(t) = \vec{M}_{xy}(0) \cdot e^{-t/T_2}. \quad (2.1.28)$$

Table 2.1: Typical relaxation times T_1 and T_2 of 1H for different tissue types at magnetic field strength $B_0 = 3$ T published by [De Bazelaire et al. \(2004\)](#) and [Stanisz et al. \(2005\)](#).

tissue	T_1 (ms)	T_2 (ms)
brain - grey matter	1820	99
brain - white matter	1084	69
kidney - cortex	1142	76
kidney - medulla	1545	81
subcutaneous fat	382	68
muscle	900	50
blood	1932	275

Spin-spin relaxation depends mainly on the molecules surrounding the spin system and, in contrast to T_1 , is mostly independent of the magnitude of the applied magnetic field. The dephasing process of the transverse component of magnetization is much faster compared to spin-lattice relaxation as shown in [Table 2.1](#) for typical biological tissues. The course of the magnetization trajectory with the representation of the two magnetization components is given in [Figure 2.2](#).

In reality, in addition to atomic and nuclear interactions and the associated relaxation processes, there are always inhomogeneities in the static magnetic field or differences in susceptibility of nearby atoms causing the dephasing in the transversal plane to be accelerated. The actual decay constant is then called T_2^* and is composed of the previously explained T_2 effect and the reversible effect T_2'

$$\frac{1}{T_2^*} = \frac{1}{T_2} + \frac{1}{T_2'}. \quad (2.1.29)$$

These additional macroscopic field inhomogeneities, however, are static and can be corrected by applying a 180° pulse, which compensates the dephasing and isolates the T_2 effect. A more detailed theoretical description of relaxation processes can be found in the Bloembergen-Purcell-Pound (BPP) theory ([Bloembergen et al., 1948](#)).

2.1.6 Bloch Equations

To mathematically represent the initially described interaction of the spins with the magnetic field but also the interaction of the spins with the environment due to spin lattice and spin spin interaction, Bloch formulated equations of motion for the magnetization \vec{M} , the so-called Bloch equations

$$\frac{d}{dt}M_x = \gamma(\vec{M} \times \vec{B})_x - \frac{M_x}{T_2} \quad (2.1.30)$$

$$\frac{d}{dt}M_y = \gamma(\vec{M} \times \vec{B})_y - \frac{M_y}{T_2} \quad (2.1.31)$$

$$\frac{d}{dt}M_z = \gamma(\vec{M} \times \vec{B})_z - \frac{M_0 - M_z}{T_1}. \quad (2.1.32)$$

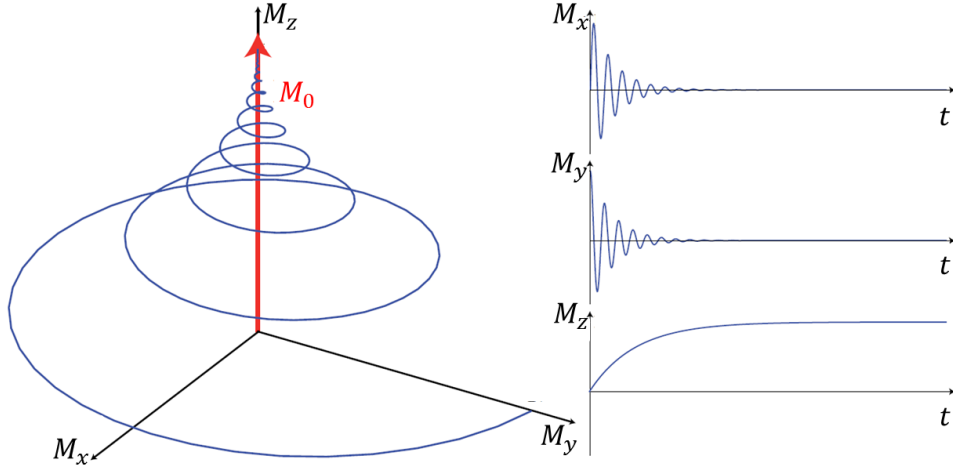


Figure 2.2: The relaxation trajectory of the magnetization vector after a 90° excitation. The transverse magnetization component M_{xy} decays with an exponential function dependent on the relaxation time T_2 as described in Equation 2.1.28, the longitudinal magnetization M_z recovers exponentially to its initial value M_0 according to Equation 2.1.26 with the relaxation time T_1 . Image adapted from Krämer (2014).

The solutions of the z-component of the Bloch equations can be found in Equation 2.1.26. The x- and y-components can be combined into a single component with a real and an imaginary part

$$M_+(t) = M_x(t) + iM_y(t) \quad (2.1.33)$$

resulting in the differential equation

$$\frac{dM_+}{dt} = -\left(i\omega_0 + \frac{1}{T_2}\right) \cdot M_+. \quad (2.1.34)$$

When solving the rewritten $M_+(t)$ component, we obtain

$$M_+(t) = M_+(0) \cdot e^{-i(\omega_0 t + \varphi_0) - t/T_2} \quad (2.1.35)$$

from which the amplitude $|M_+(t)|$ and phase $\varphi(t)$ of the NMR signal can be extracted

$$|M_+(t)| = |M_+(0)| \cdot e^{-t/T_2} \quad (2.1.36)$$

$$\varphi(t) = \omega_0 t + \varphi_0. \quad (2.1.37)$$

2.1.7 Signal Detection

To measure an NMR signal, a magnetization component orthogonal to the main magnetic field is required. Thus, the magnetization vector is excited to obtain a transverse component in the x-y-plane. A receiving coil of size \vec{A} can now be mounted perpendicular to the main magnetic field. The rotating net magnetization produces a change of the magnetic flux $\frac{d\phi}{dt}$ in the coil which generates a voltage U_{ind} according to Faraday's law of induction

$$U_{\text{ind}} = -\frac{d\phi}{dt} = -\frac{d}{dt} \int_{A_{\text{coil}}} \vec{B} \cdot d\vec{A}. \quad (2.1.38)$$

The signal in the receiving coil and thus the magnetization can be determined by using the reciprocity law. It states that the reception sensitivity of a coil corresponds to the magnetic flux density created by the same coil with a unit current (Biot-Savart law). The voltage induced in the coil is therefore

$$U_{\text{ind}} = -\frac{d}{dt} \int_{A_{\text{sample}}} \vec{B}_1 \cdot \vec{M}_0 \, dV. \quad (2.1.39)$$

The measurement of an NMR signal is possible during the decay of the transverse component as described in [Equation 2.1.28](#). The precession of the magnetization in the x-y-plane induces a voltage in the receiving coil. Due to dephasing of the spins, this oscillating signal decays over time, which is referred to as free induction decay (FID) proportional to the spin density $\rho(\vec{r})$

$$U_{\text{ind}} \propto S(t) = S_0 \cdot \int_V \rho(\vec{r}) e^{-i\omega_{\text{RF}}t} e^{-t/T_2} \, dV. \quad (2.1.40)$$

2.2 Magnetic Resonance Imaging

By transferring the NMR phenomenon described above into medical diagnostics, MRI can provide a non-invasive representation of the internal body structures. Paul C. Lauterbur and Sir Peter Mansfield received the Nobel Prize for Physiology or Medicine 2003 for this development ([Lauterbur et al., 1973](#); [Mansfield, 1977](#)). The determination of the spatial position of an NMR signal by addition of gradient fields as well as mathematical methods for a fast conversion of NMR signals into image data enabled a spatially encoded representation of the NMR signal. In the following, the basic principles of MR imaging technology are described, i.e. the spatial encoding methods, the readout technique and finally the parameters that are decisive for the image quality.

2.2.1 Spatial Encoding

Gradients

For the generation of an MR image, the NMR signal must be linked to a point in space. This is referred to as spatial encoding and is made possible by additional magnetic field gradients \vec{G} superimposed on the main magnetic field.

$$\vec{G} = \left(\frac{\partial B_z}{\partial x}, \frac{\partial B_z}{\partial y}, \frac{\partial B_z}{\partial z} \right). \quad (2.2.1)$$

Thereby it is achieved that the Larmor frequency introduced in [Equation 2.1.14](#) becomes location dependent

$$\omega(\vec{r}) = \gamma B(\vec{r}) = \gamma \left(B_0 + \vec{r} \cdot \vec{G}(\vec{r}) \right). \quad (2.2.2)$$

To choose a slice in the object, this relationship is applied for the so-called slice selection. Positioning within this slice is determined with two independent approaches, frequency encoding and phase encoding.

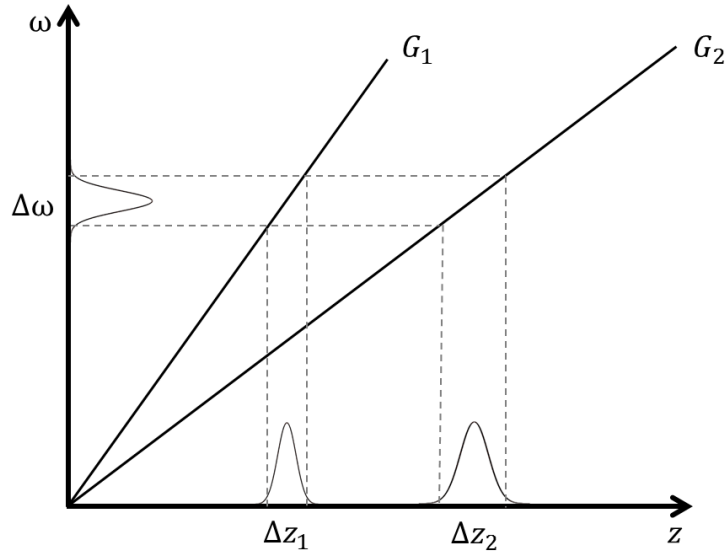


Figure 2.3: Relation of the bandwidth $\Delta\omega$ of the RF excitation pulse, the gradient strength in z-direction G_z with $G_1 > G_2$ and the resulting slice thickness Δz with $\Delta z_1 < \Delta z_2$. Larger gradient strength thus leads to a smaller slice thickness.

Slice Selection

A gradient G_z in the same direction as the main magnetic field B_0 leads to a precession frequency dependent on the z-position

$$\omega(z) = \gamma(B_0 + G_z \cdot z). \quad (2.2.3)$$

If an RF excitation pulse is applied subsequently, only the spins at the distinct z-position resonant to the applied frequency are excited. Since no RF excitation pulse is arbitrarily sharp but rather has a bandwidth of $\Delta\omega$, the excited slice has a thickness of

$$\Delta z = \frac{\Delta\omega}{\gamma G_z}. \quad (2.2.4)$$

Figure 2.3 shows how the resulting slice thickness Δz varies with the bandwidth $\Delta\omega$ of the RF excitation pulse and the gradient strength in the z-direction G_z .

Phase Encoding

After the slice selection has been carried out, the remaining two dimensions must be encoded. In phase encoding, a linearly varying gradient in the y-direction G_y is applied in a period τ before the signal readout. The magnetization thus receives an additional phase $\Delta\Phi$, which varies depending on the position in y-direction

$$\Delta\Phi = \tau\Delta\omega(y) = \tau\gamma G_y y. \quad (2.2.5)$$

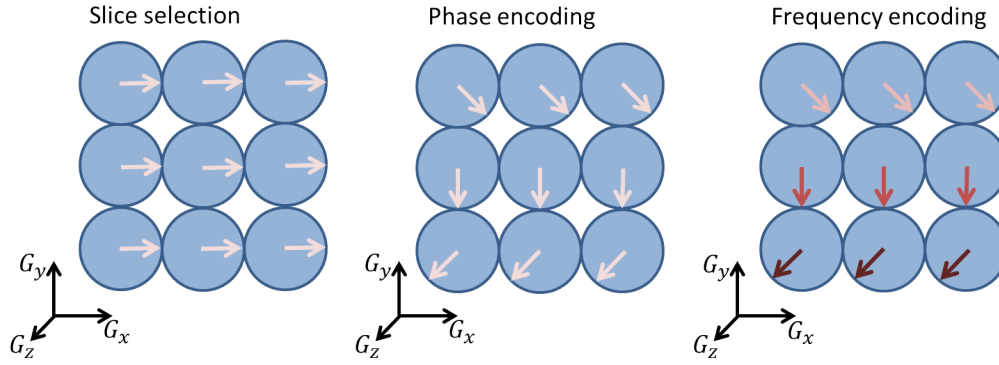


Figure 2.4: Slice selection with z-gradient and application of phase encoding gradient in y-direction and frequency encoding gradient in x-direction for distinct association of local information of the signal.

Frequency Encoding

In order to encode the third spatial dimension unambiguously, the so-called frequency encoding is used. A frequency encoding gradient G_x , also called readout gradient, is switched on during the readout. Thus each x-position is assigned a certain Larmor frequency

$$\omega(x) = \gamma (B_0 + G_x \cdot x). \quad (2.2.6)$$

Combining these two approaches results in the scheme illustrated in [Figure 2.4](#). Phase encoding prior to readout is repeated n times with G_y being incremented from $-G_y$ to $+G_y$. This means each line scanned in y-direction has a different phase gradient superimposed with the frequency encoding information that is applied during the readout. Important to note: The resolution in y-direction is thus directly related to the required number of phase encoding steps and consequently to the measurement duration.

2.2.2 K-Space Sampling

The process of encoding has led to an accumulated signal consisting of individual components with different frequencies and amplitudes. To decompose this complex signal again, a mathematical concept referred to as Fourier Transformation is used which transforms a spatially dependent signal in a frequency dependent one ([Figure 2.5](#)). The wavenumber \vec{k} is defined as

$$\vec{k}(t) = \frac{\gamma}{2\pi} \int_0^t \vec{G}(t) dt \quad (2.2.7)$$

depending on the gradients used for the spatial encoding. The signal equation ([Equation 2.1.40](#)) can then be rewritten and simplified to

$$\mathcal{F}(S(\vec{x})) = S(\vec{k}) \propto \int S(\vec{r}) e^{-2\pi i \vec{k} \cdot \vec{r}} d^3\vec{r}. \quad (2.2.8)$$

The different frequency-phase patterns in the sample, generated by the gradient fields, can now be linked to a so called k-space location. The entire k-space

can be scanned systematically by changing the gradient moment in x- and y-direction. The use of an inverse Fourier Transformation subsequently allows the reconstruction of the signal information for each spatial position in the image

$$\mathcal{F}^{-1}(S(\vec{k})) = S(\vec{x}) \propto \int S(\vec{k}) e^{2\pi i \vec{k} \cdot \vec{r}} d^3 \vec{k}. \quad (2.2.9)$$

In practice, however, the k-space cannot be sampled continuously but in discrete steps. For the most common method, cartesian sampling, $S(\vec{k})$ is sampled with steps of Δk_x in frequency encoding direction and Δk_y in phase encoding direction. For frequency encoding, a constant gradient G_x is applied for a period of time Δt_x . During this time N_x data points can be recorded. For phase encoding, however, the gradient is always switched on for a constant time t_y , but for each line in k-space, the amplitude of the gradient varies resulting in N_y steps of the increment Δk_y to cover the k-space

$$\Delta k_x = \frac{\gamma}{2\pi} G_x \Delta t_x \quad (2.2.10)$$

$$\Delta k_y = \frac{\gamma}{2\pi} \Delta G_y t_x. \quad (2.2.11)$$

The size of the recorded area of the sample is called field of view (FOV) and is determined by the width of the sampling steps $\Delta k_{x,y}$ in k-space. The spatial resolution of the final MR image depends on how many sampling steps $N_{x,y}$ this FOV is divided into

$$\Delta x = \frac{1}{k_{x,\max}} = \frac{\text{FOV}}{N_x} = \frac{2\pi}{\gamma G_x \Delta t_x N_x} \quad (2.2.12)$$

$$\Delta y = \frac{1}{k_{y,\max}} = \frac{\text{FOV}}{N_y} = \frac{2\pi}{\gamma \Delta G_y t_y N_y}. \quad (2.2.13)$$

It is important to set a sufficiently high sampling rate, because according to the Nyquist sampling theorem the sampling rate must be at least twice the highest frequency contained within that signal, otherwise under-sampling will cause image artifacts. Consequently, depending on the desired spatial resolution and FOV, a certain number of frequency and phase encoding steps is necessary, which, for the latter, affects the duration of the measurement time. Short measurement times are crucial in clinical applications. Therefore, a number of adjustments have been proposed to reduce this time. Here, the individual regions of the k-space have a major influence. Scanning the center of the k-space reveals the low frequencies that mainly contribute to the contrast of the image. In the outer k-space, instead, the high frequencies provide information about the details of the image. By adjusting the switching of the gradients and the RF-pulses in their strength and order, arbitrary trajectories can be traversed in k-space, theoretically. On this basis, a large number of k-space sampling trajectories were developed, selectable according to the desired measurement characteristics. A certain type of trajectory is called a sequence and can be visualized in sequence diagrams for better understanding.

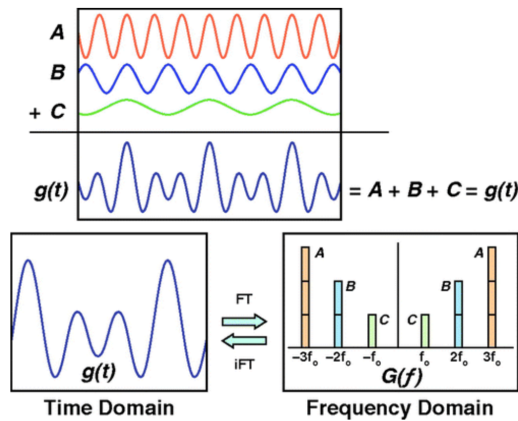


Figure 2.5: The accumulated signal consisting of individual components (A, B, C) with different frequencies and amplitudes in the time domain $g(f)$ is decomposed via a Fourier Transformation to a frequency spectrum $G(f)$ with delta functions. The frequency of the individual component can be found on the x-axis, the amplitude on the y-axis. Figure adapted from [Gallagher et al. \(2008\)](#).

2.2.3 Standard Acquisition Techniques

Spin Echo

The spin echo sequence developed by [Hahn \(1950\)](#) starts with a 90° excitation pulse which is applied simultaneously to the slice selection gradient. This excitation pulse leads to a flipping of the magnetization into the transverse plane. The spins, initially in phase, begin to change their precession frequency due to the spin-spin interaction effects described in [Equation 2.1.27](#) and thus get out of phase. The total magnetization in the transverse plane consequently begins to decay with T_2^* . A 180° refocusing pulse is therefore applied after $TE/2$, which mirrors the position of the individual spins on the x-y-plane. The phase shift is getting compensated until all spins are back in phase. This event is called an echo which occurs after the time TE ([Figure 2.6](#)). TE is also referred to as echo time and is defined as the time interval from the excitation of the sample to the echo. Static inhomogeneities in the main magnetic field and susceptibility artifacts are compensated by this refocusing technique, therefore the measured signal only depends on T_2 . In order to cover the complete k-space, a further line is recorded after the repetition time TR with changed strength of the phase encoding gradient. Thus, the desired number of phase encoding steps determines the duration of the acquisition time.

Gradient Echo

The main difference between a gradient echo sequence and the spin echo sequence is the sole use of a magnetic field gradient for echo generation instead of additionally using a refocusing pulse. After the initial pulse for the generation of a transversal component, first a gradient is applied, which leads to a dephasing of the spins. A gradient with exactly the same magnitude but opposite polarity then leads to rephasing and thus to an echo ([Figure 2.6](#)). Like

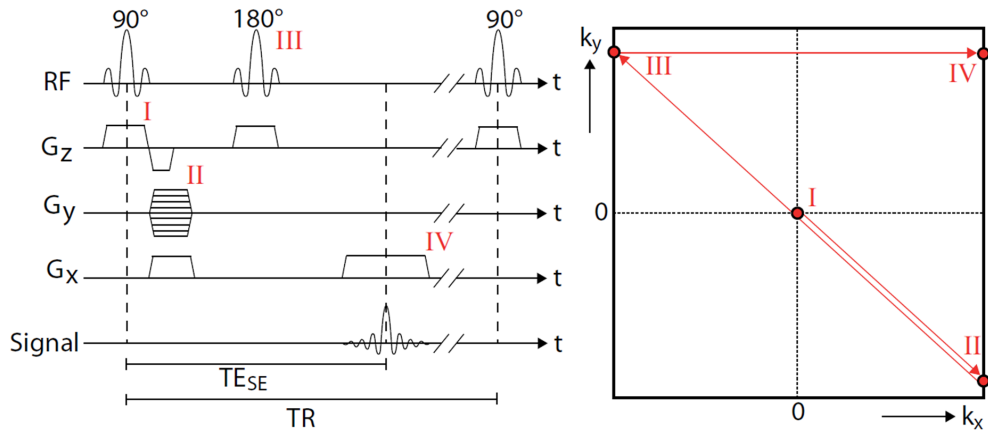


Figure 2.6: Gradient scheme of the spin echo sequence with according k-space trajectory. Together with the slice selection gradient in z-direction, a 90° excitation pulse is applied, flipping the magnetization in the transverse plane. Then phase encoding in the y-direction is applied. Dephasing due to T_2^* is reversed by a 180° refocusing pulse after $TE/2$. The inversion of the precession direction leads to an echo at $t = TE$, the T_2 decay of the signal can be measured. During readout, frequency encoding is done in x-direction. Scheme adapted from [Mie \(2011\)](#).

the spin echo sequence, each line in k-space must be recorded with a changed phase encoding gradient. The major advantage of the gradient echo sequence is the fast switching of the gradients instead of using a long 180° pulse. This makes it possible that a 90° pulse is not necessarily used as the initial pulse, but that angles $\alpha < 90^\circ$ are also sufficient to generate a measurable signal in the transverse plane. Furthermore, one initial pulse can be used to measure an echo several times by repeating the gradient sequence (Multi Echo). This also leads to considerable time savings. However, in contrast to the spin echo sequence, magnetic field inhomogeneities are not compensated. The signal is thus defined by a T_2^* decay.

Inversion Recovery

First, the magnetization is inverted by the so-called inversion pulse, a 180° RF-pulse that flips the magnetization to point along the negative z-axis. According to [Equation 2.1.26](#), the magnetization is returning to its equilibrium state depending on the T_1 relaxation time of the corresponding tissue. For signal generation, the existent longitudinal magnetization is rotated into the transverse plane by means of a 90° RF-pulse at a certain point in time and subsequent echo generation with a 180° RF-pulse using the same method as for the spin echo. The duration from start of recovery until signal readout is defined as the inversion time TI. The measurement is repeated selecting different TIs. This leads to the sampling of the magnetization curve starting with a negative magnetization and following the recovery until the former positive net magnetization is reached again.

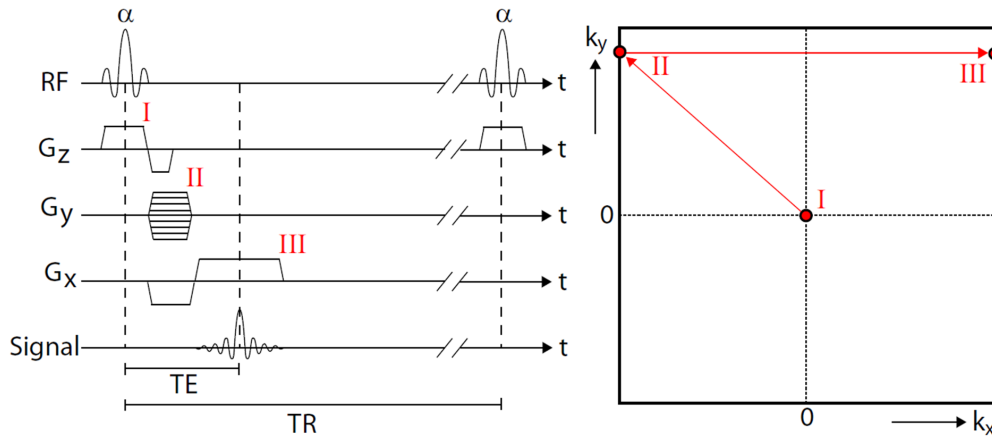


Figure 2.7: Gradient scheme of the gradient echo sequence with according k-space trajectory. A flip angle smaller than $\alpha < 90^\circ$ can be applied to create a transverse magnetization component. It is applied together with the slice selection gradient in z-direction. While phase encoding is applied in y-direction, dephasing and rephasing is performed by an additional gradient in x-direction. Scheme adapted from [Mie \(2011\)](#).

2.2.4 Signal and Contrast

T_1 - and T_2 -weighting

MRI is characterized among other things by the ability to achieve good contrasts in the tissue. In general, the image contrast is determined by T_1 , T_2 and the proton density (PD). By appropriate selection of sequence parameters, however, one of the contrasts can be emphasized. By modifying the parameters echo time TE and repetition time TR, a T_1 -, T_2 - or PD-weighted contrast can be generated. If a short TE is selected, the time of dephasing and rephasing of the spins in the transverse plane before the signal acquisition is short. Therefore the influence of T_2 is rather small. Conversely a long TE leads to a T_2 -weighting. Most MR scans use multiple excitations repeated after TR. A short TR leads to the fact that the equilibrium magnetization for the next acquisition phase is not yet completely reached. Tissue with short T_1 can already reveal more equilibrium magnetization in the same time than tissue with long T_1 . This is reflected in the signal intensity and thus leads to a T_1 -weighting. If, on the other hand, a long TR is selected, all spins are already in equilibrium during the following excitation, so the signal becomes T_1 independent. In [Figure 2.8](#) these effects are illustrated by exemplary MR images. Optimum contrast is achieved when TE and TR are approximately in the order of T_2 and T_1 respectively. In addition, several other contrasts can be generated, such as PD-weighted contrast for long TR and long TE but also other tissue specifications can be emphasized by setting additional parameters. Susceptibility contrasts as well as diffusion- or perfusion-weighted images are feasible, all of which can be selected according to the clinical objective.

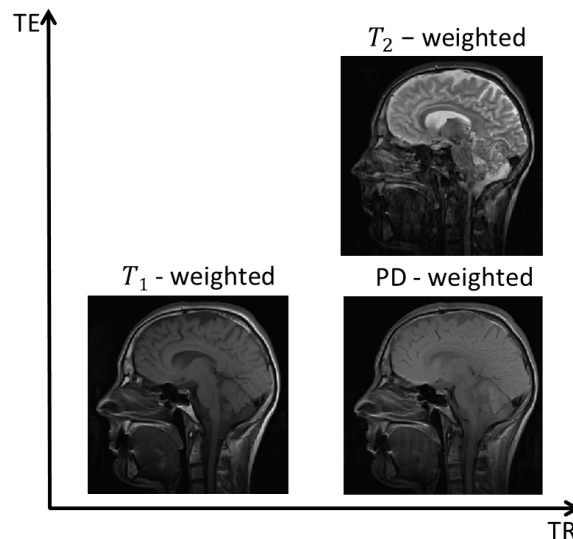


Figure 2.8: T_1 -, T_2 - and PD-weighted image of an exemplary sagittal brain slice. The obtained image contrast is dependent on the duration of TE and TR.

Image Quality

Image quality does not depend solely on the contrast of the signal. In addition, there is a statistical noise associated with each physical measurement. This noise is caused by the measured object and the used electronics and is reflected, for example, in a deterioration of quantitative measurements. Therefore it makes sense to consider the signal to noise ratio (SNR) when assessing the image quality and to take actions for noise reduction, e.g. in hardware design. The SNR can moreover be influenced by the measurement parameters as it depends on the imaging time, the readout bandwidth and the resolution.

The SNR of an image decreases with higher spatial resolution, since only a reduced number of protons can contribute to the signal. This effect has to be balanced with the increased level of detail achieved by high spatial resolution and the avoidance of partial volume effects. Partial volume effects occur when two or more objects are located within a voxel. The measured signal intensity is then composed of the signal components of the individual objects, their edges become blurred. Especially when measuring small vessels, as is necessary in perfusion imaging, it is important to avoid this effect.

2.3 Computer Tomography

With the discovery of X-rays by [Röntgen \(1896\)](#), the foundation was set for an imaging technique in which the inside of a body can become visible. The development into a computer tomography system took place several decades later. [Radon \(1917\)](#) had already provided the mathematical basis for this years before with the description of the Radon transformation. [Cormack \(1973\)](#) and

Hounsfield (1973) further developed the filtered back-projection, which allows cross-sectional images of the human body by means of absorption differences of X-rays in tissue and subsequent image reconstruction methods. In 1979, they were jointly awarded the Nobel Prize for Physiology or Medicine. This section gives a brief overview of the CT fundamentals. Further explanations are provided by Buzug (2011).

2.3.1 X-Rays

X-rays are generated with an X-ray tube. It emits an X-ray spectrum by stopping the free thermal electrons accelerated from the cathode to the anode. The emitted radiation consists mainly of Bremsstrahlung, which generates a continuous radiation spectrum through scattering processes (Figure 2.9). The so called characteristic radiation are discrete emission lines, generated by detached electrons from the anode material by collision processes. Dropping of the electrons from the outer shell onto this free space releases a specific energy that corresponds to the energy difference of the two discrete levels involved in the transition.

2.3.2 Photon Matter Interaction

The photons penetrating the body interact with it through different physical processes. The attenuation of the initial intensity I_0 is determined by Lambert Beer's law

$$I(x) = I_0 \cdot e^{-\mu x} \quad (2.3.1)$$

with the attenuation coefficient μ . It is mainly composed of Rayleigh and Compton scattering as well as the photoelectric effect in medical X-ray imaging.

Rayleigh Scattering

Rayleigh scattering is the elastic scattering of electromagnetic waves by particles whose diameter is small compared to the wavelength λ , i.e. the scattering of light at small molecules. An interaction with a bound electron is assumed. The elastic scattering process preserves the energy of the photon, but since there is a change of direction, the photon can no longer be used in reconstruction processes for imaging.

Compton Scattering

Compton scattering describes the scattering of a photon with a quasi-free electron. However, the collision is inelastic and part of the energy or linear momentum is transferred from the photon to the electron. The photon with the remaining energy is then moving in a different direction than the original one.

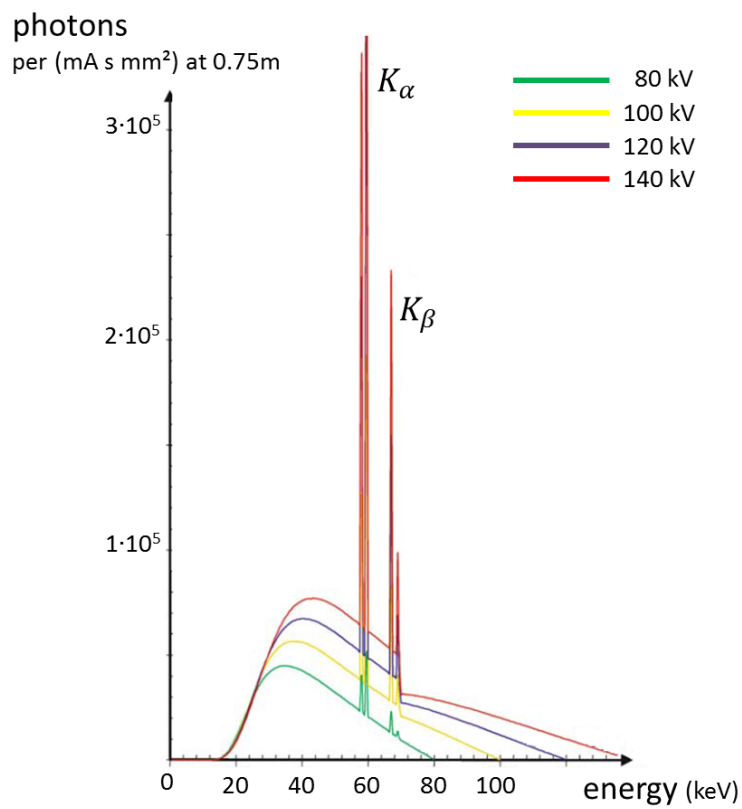
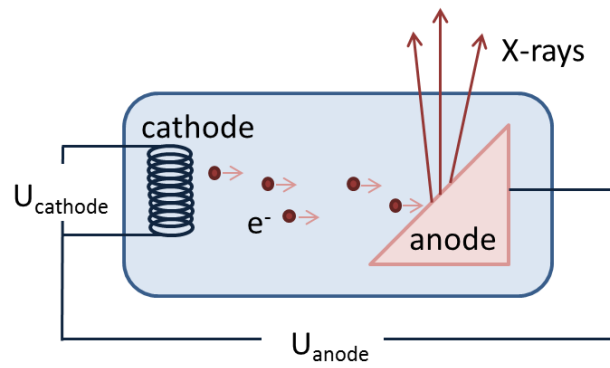


Figure 2.9: X-ray tube and X-ray spectra of a tungsten anode for different anode voltages with the continuous bremsstrahl spectra as well as the characteristic emission lines (Buzug, 2011).

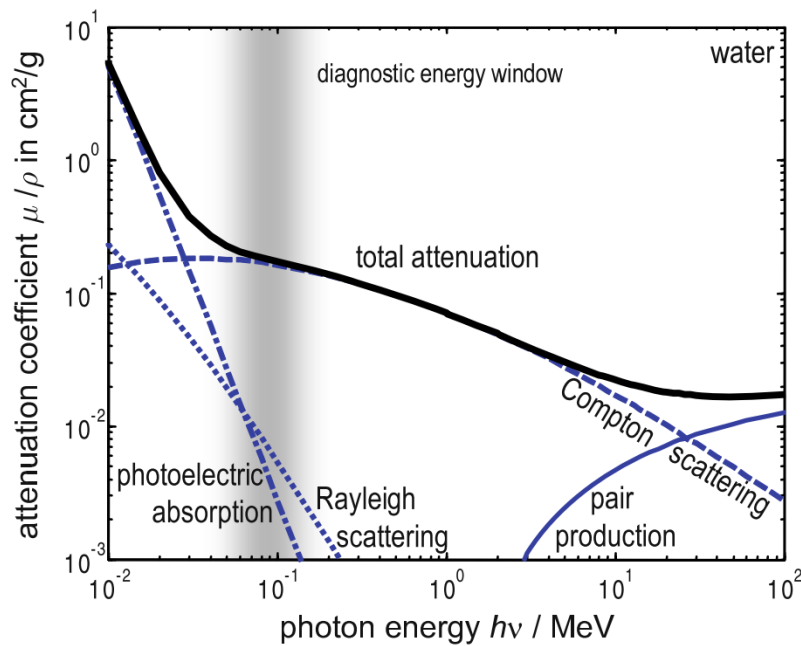


Figure 2.10: Superposition of the several absorption processes Rayleigh scattering, Compton scattering and photoelectric effect leads to the attenuation profile of X-rays in water. The diagnostic energy window (50-140 keV) is marked in grey. Image originates from [Buzug \(2011\)](#).

Photoelectric Effect

In addition to the scattering processes of the X-ray quanta, they can also be completely absorbed. An electron is released from its bond in the atom by capturing the incident photon. To do this, the photon must have at least the binding energy of the electron, the remaining energy being converted into kinetic energy of the emitted electron.

The described interaction processes and the Lambert Beer's law in [Equation 2.3.1](#) lead to the fact that the attenuation on a macroscopic scale depends on the wavelength λ of the photon and the order number Z , the density ρ and the thickness x of the absorber. The mass attenuation coefficient in water for typical clinical photon energies is given in [Figure 2.10](#).

2.3.3 Signal Acquisition

In this first generation of CT devices, the beam emitted by the radiation source is collimated into a fine needle beam. On the opposite side of the object, a single detector can measure the attenuated beam. This process is repeated for different angles and, in order to cover the entire object as efficiently as possible, the beam is also shifted tangentially. The absorption coefficient is variable within the object, and the intensity measured by the detector is a superposition of these attenuations.

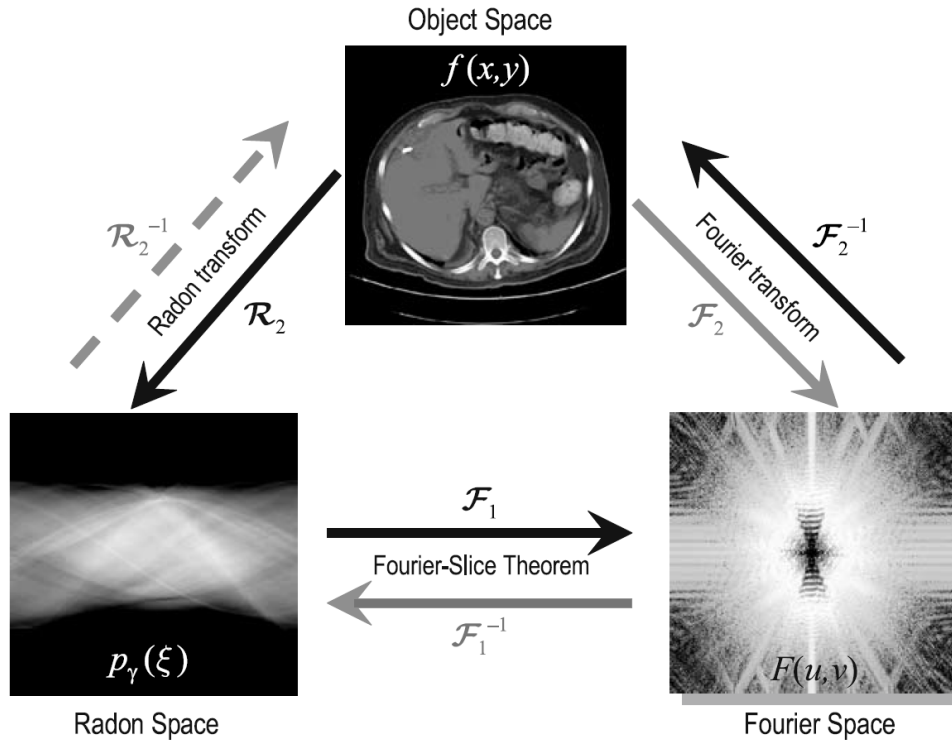


Figure 2.11: Calculation of the Object Space from the Radon Space using the Radon transformation to obtain a CT image. Using the Fourier-Slice theorem, the Object space can also be calculated by a one-dimensional Fourier transformation \mathcal{F}_1 and an inverse two-dimensional Fourier transformation \mathcal{F}_2^{-1} . Image was taken from [Buzug \(2011\)](#).

2.3.4 Image Reconstruction and Hounsfield Units

Image Reconstruction

In the reconstruction process, the inverse problem of determining the voxel-wise absorption coefficients must be solved. The absorption values are shown in a sinogram as a function of the angle ξ and the displacement γ which is called Radon Space $p_\gamma(\xi)$. The Radon Space is linked to the Object Space $f(x,y)$ via the inverse Radon transformation \mathcal{R}_2^{-1} . To determine this transformation mathematically effectively, the Radon Space can first be transferred into the Fourier Space with a one-dimensional Fourier transformation \mathcal{F}_1 . Afterwards, applying an inverse two-dimensional Fourier transformation \mathcal{F}_2^{-1} leads to the Object Space according to the Fourier slice theorem ([Figure 2.11](#)). However, using this approach, the simple unfiltered backprojection reconstructs positive attenuation values in image areas that have made no contribution to the attenuation at all. This leads to blurred areas in the reconstructed image. The incorrect values cannot be compensated by further backprojections. Therefore the backprojection is extended by a high pass filter, so that the filtered backprojection can reconstruct the image data correctly. The CT reconstruction is explained exemplary using the parallel beam geometry here. The mathematical methods of more modern geometries of CT scanners, for example cone beam CT, can be obtained from these using suitable coordinate transformations.

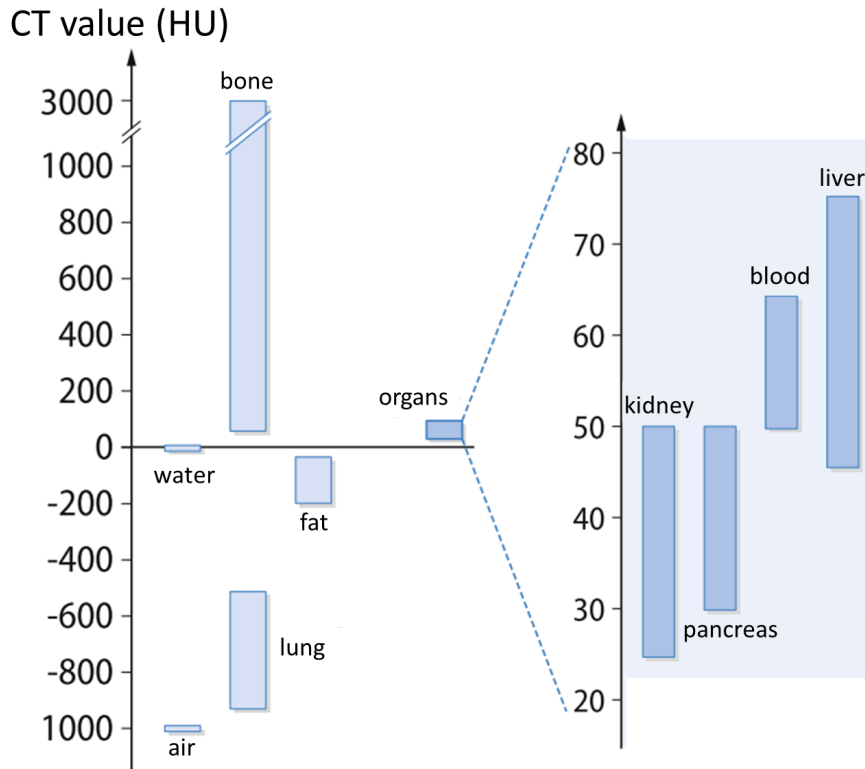


Figure 2.12: CT values in Hounsfield units for different body materials and organs. Per definition, air is assigned the CT value -1000 and water the value 0. Image adapted from [Alkadhi et al. \(2011\)](#).

Hounsfield Units

For a comparability of the images independent of different acquisition parameters such as tube voltage and beam filtering, the measured attenuation values μ are normalized. They are converted into CT values, their units are called Hounsfield units (HU). Per definition, air is assigned the CT value -1000 and water the value 0

$$\text{CT value} = \frac{\mu_{\text{voxel}} - \mu_{\text{water}}}{\mu_{\text{water}} - \mu_{\text{air}}} \cdot 1000. \quad (2.3.2)$$

CT values for different body materials and organs can be found in [Figure 2.10](#).

2.4 Perfusion Imaging

In this section, the definition of the term perfusion in general and its theoretical determination in human tissue is given. Furthermore, the concepts for measuring perfusion with MRI and CT are presented. Over time, two approaches have emerged. The first approach is based on the injection of a tracer into the investigated system. It includes dynamic susceptibility contrast (DSC) MRI and dynamic contrast-enhanced (DCE) MRI. DSC MRI is a T_2^* -weighted technique

only used in the brain for the clinical evaluation of perfusion in cerebral ischemia and brain tumors and will not be discussed further in this thesis. DCE MRI is the technique this thesis focuses on. It is based on the injection of a contrast changing material enabling T_1 -weighted bolus tracking. A second technique called arterial spin labeling (ASL) uses magnetically labeled water protons in the arterial blood as endogenous tracers. Perfusion measurements can be performed in CT as well. It is a dynamic contrast-enhanced approach (DCE CT) based on the injection of a tracer. Research into perfusion imaging has been carried out in many areas, both from a technical and clinical point of view. A more detailed insight in the methods relevant for this work will be explained in the following.

2.4.1 Tissue Perfusion

The term perfusion generally describes the process of supplying oxygen and nutrients to the capillary bed of a particular tissue. It refers to the delivery of arterial blood and in MRI and CT is measured in units of milliliters per 100 grams tissue per minute. It is important to distinguish between perfusion in the capillaries of the tissue and bulk blood flow occurring along the major arteries and veins. As perfusion is strongly correlated with the supply of oxygen and other nutrients to the tissues and removal of metabolic waste products, reduced perfusion often indicates impaired organ function or vascular diseases. Possible clinical applications include screening for malignant diseases, characterization of lesions, monitoring of lesion response to treatment and evaluation of residual pathologies (Hayes et al., 2002; Ross et al., 2002).

2.4.2 Tracer Kinetics

Although several techniques for measuring perfusion have been developed, they are all based on the tracking of a specific indicator or tracer in the form of a bolus. Modeling the tracer kinetics provides information about its distribution in the tissue and thus provides physiological information. It has to be noted that strictly spoken, there is a difference between the term indicator and tracer (Sourbron and Buckley, 2013). However, literature conventionally uses the term tracer in all cases (Lassen and Perl, 1979). The type of tracer is different for the methods developed so far.

Tracer Kinetic Modeling

The fundamental tracer kinetic model is described by the indicator dilution theory (Meier and Zierler, 1954) based on the assumption of a linear and stationary system. It is linear if there is a proportionality between the tissue response to tracer injection and the injected dose at any given time. A stationary system is independent of the injection time (Sourbron and Buckley, 2011).

Mass Conservation

Mass conservation states that no indicator is created or destroyed inside the tissue. Consequently, for a tissue with various inlets and outlets the difference

between total influx J_i and outflux J_o is the change of the tissue concentration $C(t)$ over time

$$\frac{dC}{dt}(t) = \sum_i J_i(t) - \sum_o J_o(t). \quad (2.4.1)$$

A link between influx and outflux can be established by the indicator transit time, defined as the time between entering and leaving the tissue. In an arbitrary branched tissue the indicator can use multiple paths causing a distribution of transit times. In a linear and stationary system, this leads to a probability distribution $H_i(t)$ acting as a propagator through the system (Lassen and Perl, 1979)

$$\sum_o J_o(t) = \sum_{\text{in}} H_i * J_i(t). \quad (2.4.2)$$

Here, the convolution $f * g$ is defined as

$$(f * g)(t) = \int_0^t f(u)g(t-u) du. \quad (2.4.3)$$

An integration of Equation 2.4.1 and Equation 2.4.2 yields the relationship between the tissue concentration and the concentrations at the inlets

$$C(t) = \sum_{\text{in}} R_i(t) * J_i(t) \quad (2.4.4)$$

with the definition of the residue function

$$R_i(t) = 1 - \int_0^t H_i(u) du \quad \text{or} \quad H_i = -\frac{dR_i}{dt}. \quad (2.4.5)$$

$R_i(t)$ is the proportion of dose injected at time $t = 0$ remaining in the tissue at time t . Consequently, $R(0) = 1$, and $R(t)$ continues to decrease depending on the tissue and tracer, but always remains positive. Henceforth, the expectation value of $H_i(t)$ is called transit time T_i of the inlet i .

$$T_i = \int_0^\infty t \cdot H_i(t) dt = \int_0^\infty R_i(t) dt. \quad (2.4.6)$$

Model Free Analysis

These general theoretical considerations are simplified to a single inlet model for typical MRI and CT experiments. Equation 2.4.4 then converts into

$$C(t) = I(t) * c_a(t) \quad \text{with} \quad I(t) = \text{PF} \cdot R(t). \quad (2.4.7)$$

The indicator is supplied by an arterial vessel feeding the tissue, whose measured concentration $c_a(t)$ in the blood plasma is also referred to as arterial input function (AIF). An unknown, tissue specific impulse response function $I(t)$ then connects the experimentally determinable time curves $C(t)$ and $c_a(t)$ by a convolution. PF describes the plasma flow, i.e. the carrier of the tracer to

the tissue. To estimate perfusion numbers, the simplest approach is a model-free analysis, where $I(t)$ is determined by numerical deconvolution of $C(t)$ with $c_a(t)$ (Østergaard et al., 1996a,c). This technique makes no assumptions about the tissue structure. After $I(t)$ has been calculated, the PF can be determined directly using $R(0) = 1$. Alternatively, it is feasible to derive the maximum value

$$\text{PF} = \max(I(t)) \quad (2.4.8)$$

leading to fewer numerical errors and dispersion of the contrast bolus in practice (Sourbron et al., 2004).

Compartment Models

Tracer kinetic models are used to incorporate existing information on structure, physiology and metabolic processes into the evaluation. The so-called compartment models (CM) are based on a tissue description consisting of one (single) or more (multi) compartments with one or several inlets or outlets. Accordingly, there is a multitude of possible models with corresponding assumptions and boundary conditions that can be applied depending on the organ and pathology (Ingrisch and Sourbron, 2013; Sourbron and Buckley, 2011). A specific analytic approach for the determination of the residual function $R(t)$ is chosen, allowing the determination of further tissue parameters such as the exchange rate between the compartments or their volume.

A compartment is described as a space in which the tracer concentration within the distribution volume v is homogeneous yet time-dependent. The concentration of the indicator $c(t)$ within this compartment is given by the number of indicator molecules divided by the distribution volume

$$c(t) = \frac{C(t)}{v}. \quad (2.4.9)$$

In addition, it is assumed that the outflow of all outlets must be proportional to the compartments' concentration

$$J_o(t) = F_o c(t) \quad (2.4.10)$$

with the factor of proportionality F_o , the clearance of the system (Lassen and Perl, 1979). An exchange between the compartments is assumed. The equation of mass conservation Equation 2.4.1 for a single compartment model then changes into

$$v \frac{dc}{dt}(t) = \sum_i F_i c_i(t) - \sum_o F_o c(t). \quad (2.4.11)$$

Solving the differential equation reveals a mono-exponential decrease of the residual function. The time constant is the mean transit time (MTT), completely independent of the inlet, hence it does not depend on the entry time of the tracer. The MTT is determined by the volume of distribution v and the clearance of the outlets

$$R(t) = e^{-t/\text{MTT}} \quad \text{with} \quad \text{MTT} = \frac{v}{\sum_o F_o}. \quad (2.4.12)$$

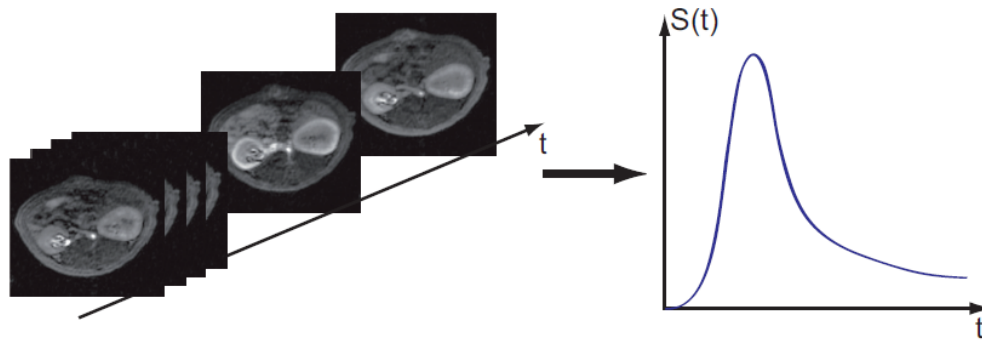


Figure 2.13: DCE signal over time. A series of images within a short time frame is acquired. For each voxel, the signal change $S(t)$ caused by the passing CA bolus can be derived. Figure adapted from [Zimmer \(2014\)](#).

Accordingly, for n interacting compartments, n differential equations are generated from [Equation 2.4.11](#).

2.4.3 Dynamic Contrast Enhanced Techniques

The idea that tissue perfusion could be measured by injection of an external tracer and subsequent measurement of the resulting signal changes was first proposed by [Runge et al. \(1984\)](#) and [Pettigrew et al. \(1986\)](#). In DCE MRI, the external tracer is injected into a peripheral vein as a bolus, which then moves through the body within the bloodstream. The distribution of the bolus is therefore related to the blood supply and the physiology of the investigated tissue. However, the concentration of tracer cannot be measured directly with MRI. Instead, the administered tracer leads to changes in the relaxation of the blood, which in turn leads to a signal change. Imaging with a fast sequence can produce a movie, a time-resolved image series of the same slice or volume during the passage of the injected CA. Thus, voxel wise signal curves $S(t)$ in the tissue of interest are generated ([Figure 2.13](#)). The concentration $c(t)$ of CA can then be determined from these curves. Finally, the kinetic tracer theory described in [subsection 2.4.2](#) is applied to find a suitable tissue model from which hemodynamic parameters can be calculated. DCE MRI is currently the recommended method for perfusion imaging in organs besides the brain ([Brix et al., 2004](#); [Dujardin et al., 2005](#); [Jerosch-Herold et al., 2004](#)).

The DCE technique is also employed in CT. The underlying process is the same, but the applied CA leads to a changed attenuation coefficient, which results in a change of the measured signal.

2.4.4 Arterial Spin Labeling

ASL was first proposed in 1992 by [Detre et al. \(1992\)](#), [Williams et al. \(1992\)](#) and [Kwong et al. \(1992\)](#). This MRI technique is non-invasive and no external tracer needs to be injected. Instead, tissue perfusion is measured by using water in the arterial blood itself as an endogenous and freely diffusible tracer.

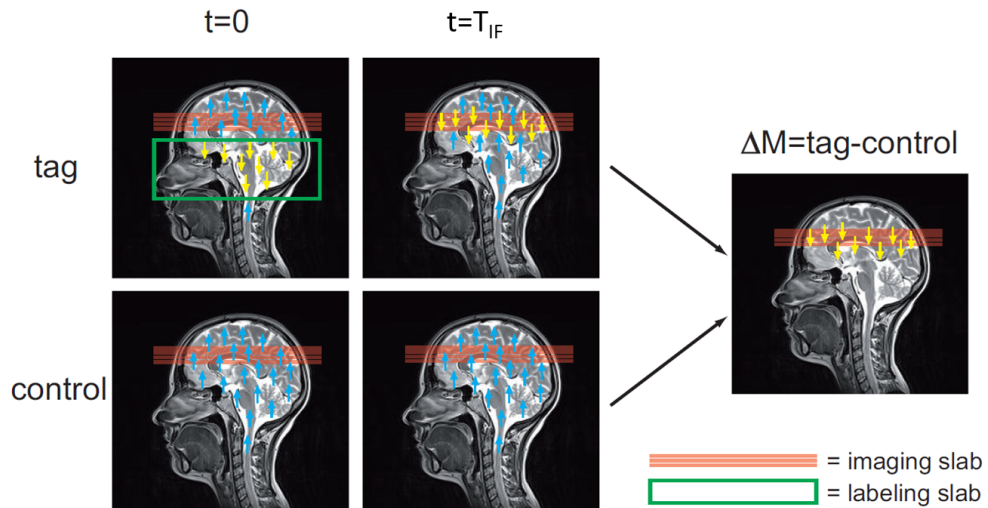


Figure 2.14: ASL creates a tag image where, at $t = 0$, the arterial blood is labeled by an RF-pulse in a slab proximal to the imaging region (green). After the inflow time T_{IF} , a second image is acquired when the tagged blood (yellow) reaches the imaging slab (red). Additionally, a control image is taken where the magnetization is not excited (blue). The ASL signal is achieved by subtraction of the control image from the tag image at $t = T_{IF}$ representing the magnetization created by the moving spins during T_{IF} . Image adapted from [Petersen et al. \(2006\)](#).

To employ arterial blood as a tracer, it has to be labeled in order to differentiate the tracer signal from the original blood water signal. This is done by inverting the magnetization of the incoming arterial blood proximal to the tissue volume of interest. Thus, it is important that these arteries actually supply the region to be measured afterwards. Subsequently, during the so-called inflow time (T_{IF}) or post-labeling delay, one waits until the labeled blood traveled from the labeling to the imaging site. Here the so called *tag* image is recorded. It has a reduced magnitude due to the delivered inverted magnetization, i.e. the labeled arterial blood water. A *control* image without any signal preparation is also acquired. It is assumed that the static components are equal both in the tag and in the control image. The difference between these two $\Delta M = \text{tag} - \text{control}$ is thus only the signal of the labeled blood which has flowed into the tissue during T_{IF} and is called perfusion-weighted image. Since this signal change is typically only 0.5 % - 1.5 % of the total signal, several tag and control pairs are typically recorded and averaged to increase the SNR of the acquisition. In the following, two sequences with different principles of the MR signal labeling are described.

Continuous ASL

[Detre et al. \(1992\)](#) and [Williams et al. \(1992\)](#) first established the so-called continuous arterial spin labeling (CASL). An RF inversion pulse is applied continuously in the labeling slice with a typical pulse duration of approximately 2 - 4 s. To do this, a magnetic field gradient is applied in the direction of the flowing arterial blood. This causes the resonance frequency of the magnetized

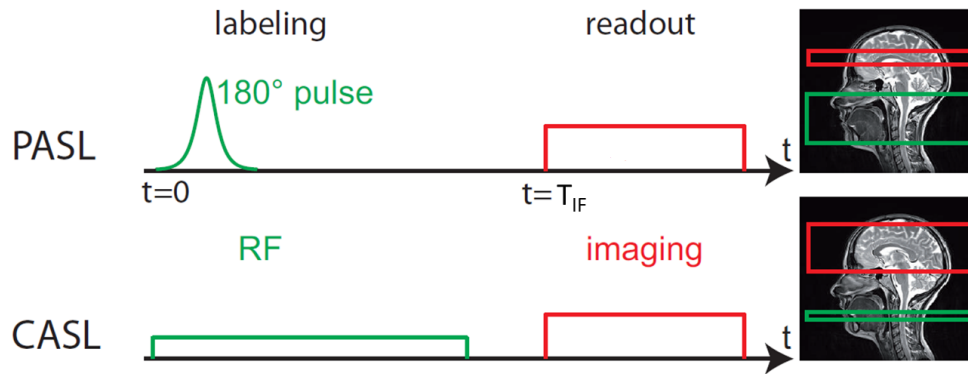


Figure 2.15: Pulsed ASL (PASL) uses a short inversion pulse and a larger labeling region compared to continuous ASL (CASL) which applies a continuous RF-pulse with a low amplitude in a small labeling region. Imaging starts after the inflow time (T_{IF}). Figure adapted from [Gregori \(2009\)](#).

hydrogen atoms to slowly change and eventually invert as they flow through the labeling slice. This inversion technique is also known as flow-driven adiabatic inversion ([Dixon et al., 1986](#)).

Pulsed ASL

[Edelman et al. \(1994\)](#) suggested to use a short 180° RF-pulse with a duration of 10 ms - 20 ms instead of a long pulse in a thick slab proximal to the imaging volume. The result, i.e. the inverted magnetization of the blood, is the same, but due to the optimization of the RF hardware for short pulses rather than continuous irradiation pulses, a reduced energy deposition in the tissue is possible. This technique is called pulsed ASL (PASL). Although a higher labeling efficiency can be reached, the arrival time of the magnetized blood in the imaging volume varies considerably more due to the thick slab. Thus the T_1 decay also varies and leads to a bias in perfusion measurement.

In current research, attempts are being made to combine both techniques in order to optimally exploit their advantages, an example of which is the pseudo continuous pCASL sequence ([Dai et al., 2008](#); [Wu et al., 2007](#)).

Perfusion measurements with ASL can be quantified. In [Buxton et al. \(1998\)](#) the general kinetic model (GKM) is introduced, which combines physical processes like longitudinal decay and bolus length with mathematical models.

Materials and Methods 3

The first section of this chapter describes the technical specifications of the imaging modalities MRI and CT relevant for this work. This is followed by a presentation of the measurement and evaluation methods of the individual experiments regarding the perfusion phantom study and the retrospective patient study of perfusion in rectal cancer patients. Sections of the latter have been published in (Gaa et al., 2017) and the description of the corresponding methods is presented here.

3.1 DCE MR and CT Imaging

The DCE imaging technique requires several procedures reaching from calibration to image acquisition and analysis. The specific methods that have been applied in this thesis to implement them will be further explained in the following (Figure 3.1).

3.1.1 MR Scanners and Coils

MR Scanners

The MRI measurements were carried out at the Department of Clinical Radiology of the University Hospital Mannheim. Clinical 3 T full-body scanners (MAGNETOM Tim Trio and MAGNETOM Skyra, Siemens Healthineers, Erlan-

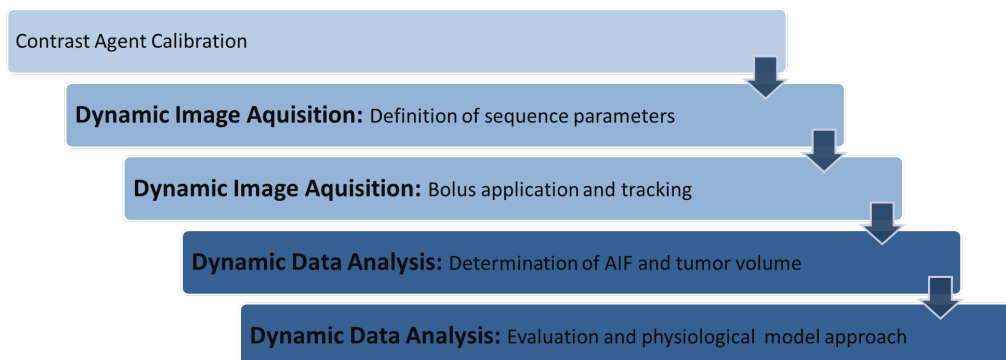


Figure 3.1: Schematic visualization of the operating steps for DCE imaging: CA calibration, image acquisition and data analysis.

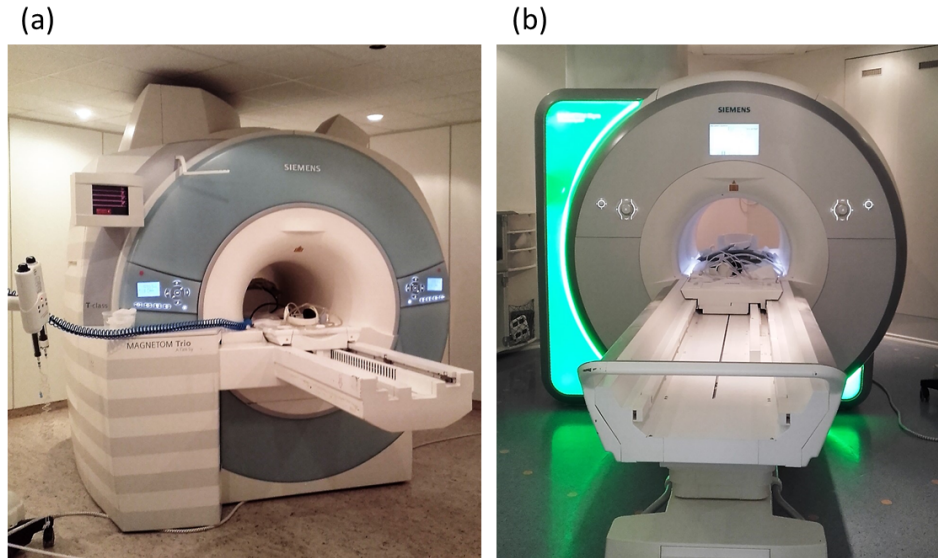


Figure 3.2: 3T MR scanners (a) MAGNETOM Tim Trio and (b) MAGNETOM Skyra (both Siemens Healthineers, Erlangen, Germany) used for patient and phantom measurements. In picture (a) the automatic CA pump is visible.

gen, Germany) were used (Figure 3.2). The static main magnetic field in both scanners is generated by superconducting coils cooled with liquid helium. In the bore of the scanner, the gradient system and transmitting coils are included. Also, the system is equipped with shim coils that ensure the homogeneity of the main magnetic field. This means that the B_0 -field is adjusted by active shimming before the scan.

The MAGNETOM Tim Trio system length is 2.13 m with a bore diameter of 0.60 m. A maximum gradient amplitude of $40 \frac{\text{mT}}{\text{m}}$ with a maximum gradient system slew rate of $200 \frac{\text{T}}{\text{m}\cdot\text{s}}$ (Siemens, 2004) is permitted. The maximum possible FOV amounts to $0.50 \text{ m} \cdot 0.50 \text{ m} \cdot 0.45 \text{ m}$.

The MAGNETOM Skyra system length is 1.73 m with a bore diameter of 0.70 m. A maximum gradient amplitude of $45 \frac{\text{mT}}{\text{m}}$ with a maximum gradient system slew rate of $200 \frac{\text{T}}{\text{m}\cdot\text{s}}$ (Siemens, 2012) is permitted. The maximum possible FOV amounts to $0.50 \text{ m} \cdot 0.50 \text{ m} \cdot 0.45 \text{ m}$.

MR Coils

The 32-element spinal matrix coil system installed in the patient table was used for signal reception. Besides, specific receive coils were employed. Patient measurements were performed with a flexible surface coil (Rx Body18) that could be placed directly on the patient's abdomen. Phantom measurements have been performed with a 15 channel phased array knee coil (TxRx 15 channel knee) to optimally enclose the phantom (Figure 3.3).

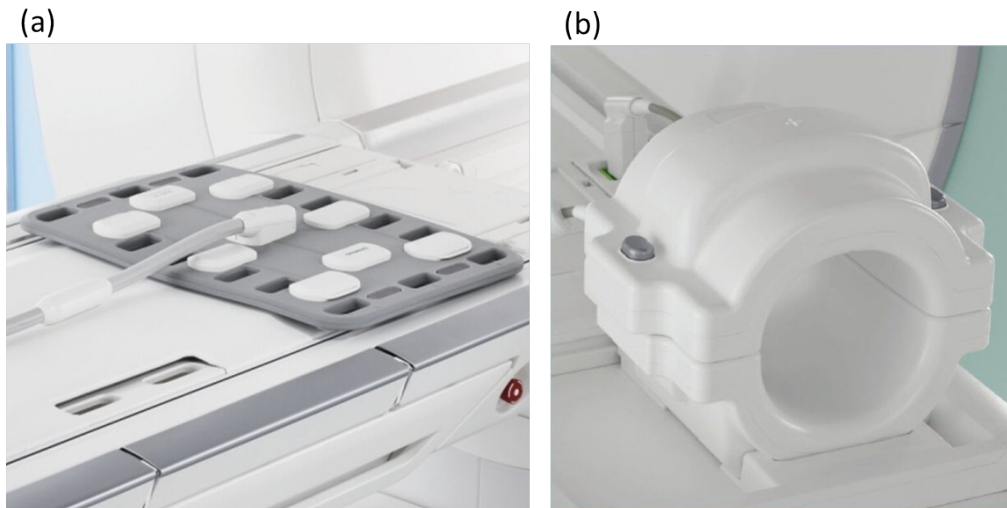


Figure 3.3: (a) Flexible surface coil (Rx Body 18) for patient measurements and (b) 15 channel phased array knee coil (TxRx 15 channel knee) for phantom measurements.

3.1.2 MR Sequences

TWIST Sequence for DCE MRI

In DCE imaging, a series of images are taken over a short time interval to represent the passage of the contrast bolus. This results in a trade-off between good spatial imaging of the tissue and a high temporal resolution, ensuring the best possible sampling of the contrast bolus signal. For an enhanced spatial resolution, the sampling density of the k-space points in conventional k-space imaging would be increased. This, in turn, is associated with an extended measurement time, in contradiction to a high temporal resolution.

The gradient echo sequence described in [subsection 2.2.3](#) remains the fundamental sequence to fulfill these requirements. It offers the possibility for very short TRs and TEs, low flip angles, and parallel image acquisition. In addition, one can benefit from the fact that information about image contrast can be found in the center of the k-space, while edges and details are encoded in the periphery as described in [subsection 2.2.2](#).

In DCE MRI, this was first used with a method known as keyhole imaging developed by [Van Vaals et al. \(1993\)](#) for measuring perfusion data of tumors and vascular lesions. In the rectangular k-space grid, the central phase-encoding lines were measured with a higher sampling rate than the outlying k-space points. This results in a series of highly time-resolved images with satisfactory spatial resolution.

Further modification led to the TWIST (time-resolved imaging with stochastic trajectories) ([Vogt et al., 2007](#)), ([Song et al., 2009](#)) sequence applied in this thesis. This 3D gradient echo sequence contains a phase encoding plane in k_y and k_z direction and frequency encoding in k_x direction. The sampling points in

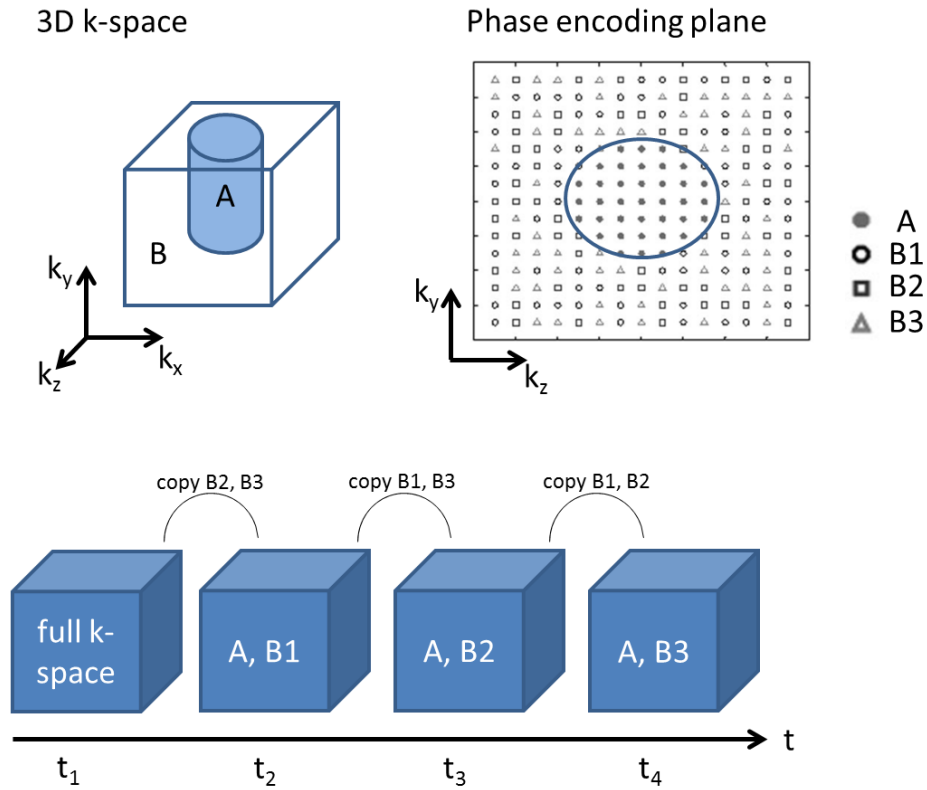


Figure 3.4: Illustration of the TWIST sequence: The 3D k-space is divided into two regions. The inner part A of the k-space is completely sampled for each image. In the outer region B only a fraction (B1, B2, B3) is measured. The missing part is completed by previous or subsequent measurements of the dynamic measurement series.

the phase encoding plane are sorted according to their radial distance r and an azimuth angle ρ from the center. Then, the k-space is divided into two regions: the inner region A, within a certain radial distance r_c , providing contrast information, and the outer region B, which contains high-frequency information. The entire k-space is only sampled in the first acquisition of the dynamic series. For each additional image all points located in region A are sampled but only a fraction of B (Figure 3.4). Sampling is semi-randomized alternating between the two regions starting at the outer edge of A. The missing information from the non-sampled k-space lines in B is obtained from the previously or subsequently acquired images. It is assumed that the contrast in the dynamic images changes as the CA flows through them, but not the information about edges and details in the periphery of the k-space.

Parallel Imaging

Parallel imaging or parallel acquisition technique (PAT) is another method to increase the acquisition speed. Multichannel or phased array receive coils are implemented to simultaneously acquire data. Initially, this leads to an increased SNR (Roemer et al., 1990). Besides, the individual receiving coil elements have

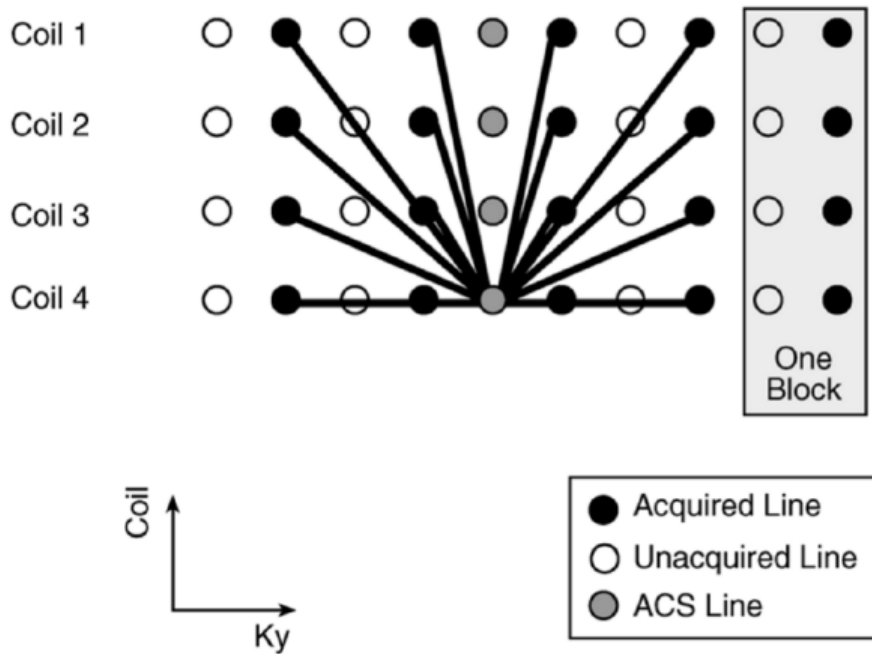


Figure 3.5: Principle of parallel imaging with GRAPPA reconstruction. By selecting an acceleration factor of $PAT = 2$, only every second line of the k-space is acquired. The autocalibration signal (ACS) supplies the weighting factors of each coil for the reconstruction of missing lines. Figure from [Griswold et al. \(2002\)](#).

different spatial dependent sensitivities. This allows reducing the number of phase encoding steps while the missing information is compensated by the additional data of the receiving coil elements. Undersampling of the k-space reduces measurement time, for example for a cartesian acquisition scan time is linearly proportional to the number of phase-encoding steps.

The algorithm applied in this thesis is called generalized autocalibrating partially parallel acquisitions (GRAPPA) ([Griswold et al., 2002](#)) and is visualized in [Figure 3.5](#). The acceleration factor can be selected and indicates which fraction of the k-space is sampled. It can typically be set between $PAT = 2$ and $PAT = 6$. The FOV and the resolution are preserved by the additional data of the phased array coils. Before reconstruction, an indirect sensitivity measurement is performed, which provides further spatial information, the so-called autocalibrating signal (ACS). It consists of multiple sampling lines in the k-space center to determine the weighting of the individual receiving coils. Finally, the reconstruction is performed for each coil element and assembled with a sum-of-squares method. The disadvantages of this approach are the reduction of the SNR and artifacts that can occur during image processing.

3.1.3 MR Contrast Agent

Mechanism

MR CA is used to increase contrast in conventional anatomical imaging. Furthermore its distribution in tissue provides information on physiological parameters during functional imaging. The MR CAs used in these phantom and patient studies were Dotarem (Guerbet, France) and Gadovist (Schering AG, Germany). They both contain the paramagnetic ion gadolinium (Gd) and otherwise differ only by their manufacturer. Since the Gd ion is toxic to the human organism, it is embedded in a chelate, diluted and applied intravenously. The seven unpaired electrons in the outer shell of the lanthanide lead to a faster relaxation of the surrounding protons causing shorter relaxation times, mainly influencing T_1 . This means that the MR signal does not originate directly from the CA but is indirectly represented by the amount of interaction through chemical bonds between water protons and the paramagnetic ions (Engelstad and Wolf, 1988).

The concentration of the Gd ion is then inversely proportional to the change of the relaxation time, predicted by the Solomon-Bloembergen equations (Gowland et al., 1992)

$$C(t) = \left(\frac{1}{T_1(t)} - \frac{1}{T_{10}} \right) / R_{Gd}. \quad (3.1.1)$$

T_{10} describes the pre-contrast T_1 time and is hereinafter also referred to as baseline. The proportional constant R_{Gd} is called the spin lattice relaxivity of Gd, dependent on the field strength and chemical structure of the CA and can be obtained from the CA manufacturer.

The kinetic behavior of a CA in vivo can be determined by connecting CA concentration changes with changes in the signal of the MR images. In principle, the relationship between the CA concentration and the relative increase in the signal intensity for each image sequence can be derived from the Bloch equations. First, it should be considered that a linear relationship cannot be assumed automatically. Therefore, additional calibration measurements are generally recommended.

Calibration

Consequently, a calibration measurement was carried out as a foundation for the CA measurements performed in this thesis. The relationship between the concentration of the Gd containing CA and the measured MRI signal was determined. A phantom consisting of several small tubes with volumes of 50 ml each was used. A dilution series of different Gd concentrations was prepared. The samples consisted of dilutions of (0.025, 0.05, 0.1, 0.2, 0.4, 0.8, 1.6, 3.1, 6.3, 12.5, 25, 50) mmol/l (Figure 3.6). They were placed one by one in the scanner's isocenter to avoid errors caused by B_0 -field inhomogeneities. Data were acquired with a clinical standard gradient echo sequence, parameters are given in Table 3.1.

Table 3.1: Imaging parameters of the MR CA calibration measurement.

Sequence	TE	TR	FA	matrix size	FOV	spatial resolution
GRE	10 ms	200 ms	25°	128 × 128	(320 × 320) mm ²	(2.5 × 2.5 × 2) mm ³

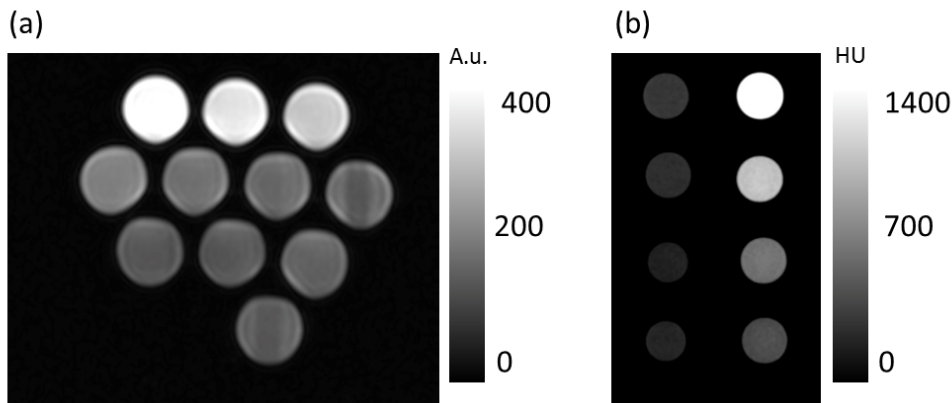


Figure 3.6: Calibration of the relationship between the concentration of the CA and the measured signal. (a) MR measurement of Gd containing tubes with different concentrations. Note that the tubes were measured subsequently to avoid errors caused by B_0 -field inhomogeneities and (b) CT measurement of iodine containing tubes with different concentrations.

3.1.4 CT Scanner and Sequence

CT Scanner

The CT measurements were as well carried out at the Department of Clinical Radiology of the University Hospital Mannheim. A dual-source CT system (Somatom Force, Siemens Healthineers, Erlangen, Germany) was used (Figure 3.7). At each of the two X-ray tubes, a voltage between 70 and 150 kV can be set. The detectors are supplied with an anti-scatter 3D collimator grid and can acquire 192 slices each. A rotation time up to 0.25 s can be reached with spatial resolutions of 0.25 mm. The gantry opening is 0.78 m. A tin filter shields patients from clinically irrelevant low-energy radiation which results in less dose.

DCE CT Sequence

Analogous to the DCE MRI measurement, DCE CT measures a series of images of the selected tissue section over a certain time to track the previously injected CA bolus. In the acquired image section, the supplying arteries for the determination of the AIF and the tissue under investigation need to be displayed. In contrast to MRI measurements, the focus does not lie on finding a compromise between high temporal and spatial resolution. The main challenge, in this case, is the enhanced dose application to the patient. To perform DCE measurements, many separate examinations are necessary. They burden the patient with CA and, for CT, with additional radiation dose, ac-



Figure 3.7: CT scanner Somatom Force (Siemens Healthineers, Erlangen, Germany) used for patient and phantom measurements.

cumulating through the dynamic measurement. Only the latest generation of CT scanners with dose reduction by the tin filter of up to 80 % (Leyendecker et al., 2019) makes such acquisition possible and ethically justifiable in the first place. The scanner has an implemented Volume Perfusion CT Body Sequence, a dynamic shuttle-mode perfusion protocol with automated motion correction for improved accurate anatomical object alignment. Depending on the patient's body weight, tube voltage can be set to the lowest reasonable value of 70, 80, 90 or 100 kVp (peak kilo Voltage). It is important to note that the detector, therefore, has to be optimized for low photon fluxes.

3.1.5 CT Contrast Agent

Mechanism

The CA Imeron (Bracco Imaging, Germany) used for the DCE CT measurements in the phantom and in the patients in this work is iodine based. In contrast to MRI, where the paramagnetic ion in the CA acts on the surrounding water, CT uses substances that directly attenuate the beam. This requires a significant difference in their atomic number (number of protons of the element, Z) to distinguish themselves from other surrounding materials. The difference to elements naturally occurring in the human body (e.g. hydrogen, oxygen, carbon, and nitrogen with $Z < 10$) is large for iodinated CA ($Z = 53$). This makes it easy to distinguish them from body tissues based on the spectral behavior of the materials. In addition, iodine in small quantities is not toxic to the human body and is easily soluble in water (Laubenberger and Laubenberger, 1999).

The kinetic behavior of the CA in the examined tissue can be determined by associating the concentration of the CA with the signal intensity. This correlation is much simpler in CT than in MRI. A higher attenuation value, as in the case of the high atomic number of the CA, is directly linearly related to the grey values - measured in HU - of the CT images.

Calibration

A series of measurements were performed to demonstrate the linear correlation described above between the concentration of the iodine containing CA and the measured CT signal (Figure 3.6). A phantom consisting of several tubes with volumes of 50 ml each was used. A dilution series of different iodine concentrations was prepared. The samples consisted of dilutions of (0.01, 0.02, 0.04, 0.08, 0.16, 0.32) mmol/ml. Data were acquired with a standard volume sequence with lowest tube voltage of 70 kV.

3.1.6 Application of Perfusion Models

Equation 2.4.7 provides the fundament of tracer kinetic calculations of perfusion parameters for the two approaches introduced in this work, the model-free fast deconvolution approach (FD) and compartment modeling (CM).

AIF

The convolution of the AIF with the residual function indicates that the determination of the AIF plays a central role here. Their exact determination is necessary to consider the effects of the bolus arrival on the tissue of interest, e.g. injection rate, cardiac output, arterial condition, the vascular route to the tissue, etc. These influences should be taken into account beforehand to ensure no impact on the calculation of specific tissue perfusion parameters.

After the contrast bolus has been administered intravenously, it must travel through large areas of the body before entering the tissue of interest. The typical representation of the measured signal curve at one position over time is often theoretically described by a gamma variation function. It starts with a relatively flat beginning, the so-called *baseline*, before the arrival of the CA in the tissue of interest. It is then followed by a sharp increase up to the maximum concentration and subsequently a slower decrease called the *first passage* of the CA.

However, transport through the body has several effects on its shape, in particular how and where the measurement of AIF is conducted has a significant impact. Depending on whether the AIF is measured in a small artery nearby the tissue of interest or large arteries distal to it, either partial volume artifacts in small arteries or bolus delay and bolus dispersion effects in large arteries may occur.

Dual Compartment Exchange Model

In contrast to the model free deconvolution analysis, dual compartment models assume that the tracer in the tissue can distribute in two separate compartments, the intravascular plasma space and the extracellular extravascular space. The dual compartment exchange model (2CX) is the most general 2CM that describes those two separate compartments with the plasma volume PV and the extracellular extravascular volume EV, respectively. Additional to a single

compartment model, influx and outflux from the interstitium is taken into account (Figure 3.8).

The concentration of the CA in the tissue is described as

$$C_t(t) = PV \cdot C_{PV}(t) + EV \cdot C_{EV}(t) \quad (3.1.2)$$

where $C_{PV}(t)$, the CA concentration in the intravascular plasma space, is defined as

$$\frac{dC_{PV}}{dt} = \frac{PSAP}{PV} (C_{EV}(t) - C_{PV}(t)) + \frac{PF}{PV} (C_a(t) - C_{PV}(t)). \quad (3.1.3)$$

$C_a(t)$ is the CA concentration in the arterial plasma. The permeability surface area product (PSAP) describes the in- and outflow rate of the exchange of the CA between the two compartments. The CA concentration $C_{EV}(t)$ in the extracellular extravascular space can be obtained by

$$\frac{dC_{EV}}{dt} = \frac{PSAP}{EV} (C_{PV}(t) - C_{EV}(t)). \quad (3.1.4)$$

Solving Equation 3.1.3 and Equation 3.1.4 yields the bi-exponential tissue response function $H_{2CX}(t)$ with function parameters PF, PV, PSAP, EV. Combined with Equation 2.4.7 and the specific impulse response function for the 2CX model, the four parameters PF, PV, PSAP, EV can be determined. For further details the work of Ingrisich and Sourbron (2013) can be consulted.

Dual Compartment Uptake Model

The dual compartment uptake model (2CU) is a simplification of the 2CX. If the MTT is long compared to measurement time, efflux is negligible from EV. Equation 3.1.4 subsequently simplifies to

$$\frac{dC_{EV}}{dt} = \frac{PSAP}{EV} (C_{PS}(t)) \quad (3.1.5)$$

and results in a monoexponential tissue response function $H_{2CU}(t)$. Solving Equation 2.4.7 with the new tissue response function yields to a three parameter model with parameters PF, PV, PSAP. Compared to the 2CX model the number of model parameters is reduced which means EV is not accessible (Figure 3.8).

Perfusion and Permeability Parameters

Permeability is the transport rate of the tracer per unit of the capillary surface. The parameters PF and PV are thus assigned perfusion parameters, whereas PSAP and EV are referred to as permeability parameters. A simultaneous measurement of perfusion and permeability parameters with the DCE technique requires the application of a suitable tracer kinetic model to distinguish the contribution of both spaces. Moreover, a CA exchange between the two spaces is assumed caused by leakage via the endothelial wall, considered equal in both directions.

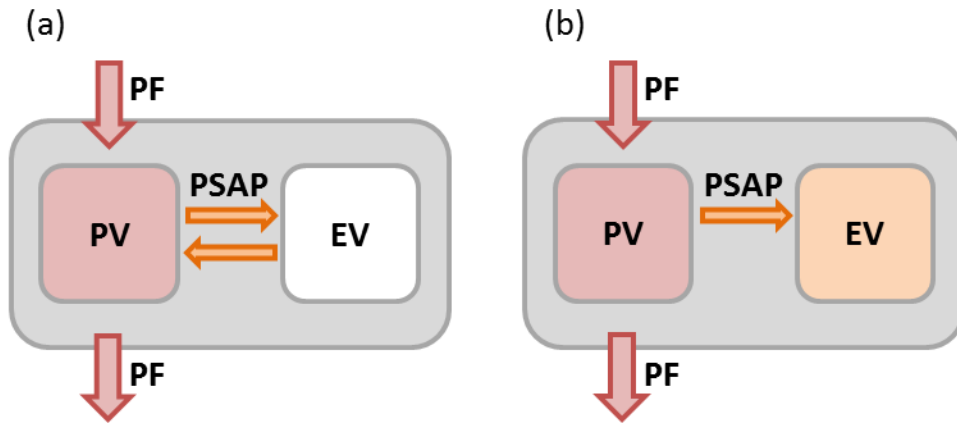


Figure 3.8: Schematic illustration of (a) the dual compartment exchange model (2CX) and (b) the dual compartment uptake model (2CU) with parameters plasma flow (PF), plasma volume (PV), extracellular extravascular volume (EV) and permeability surface area product (PSAP). The CA is transported via the PF and can cross the membrane between PV and EV. In the 2CU, no efflux from EV is assumed.

Other, sometimes more descriptive parameters can be derived from the parameters that originate directly from the model. The extraction fraction EF is the percentage of CA that extravasates and can be calculated by

$$EF = 1 - \exp\left(-\frac{PSAP}{PF}\right). \quad (3.1.6)$$

For reasons of completeness, K_{trans} should also be mentioned here, a parameter used in the Tofts model, measuring the flow into the interstitium (Tofts et al., 1999).

In literature, the parameters blood flow (BF) and blood volume (BV) are used instead of plasma flow and plasma volume, also taking the amount of red blood cells into account. A translation between both conventions can easily be performed by a scaling factor based on the hematocrit (HCT), the volume percentage of red blood cells in the blood. It follows that $PF = (1 - HCT) \cdot BF$. A $HCT = 0.45$ was assumed for the studies performed in this thesis. This corresponds to the human mean and was used, as an exact value was not determined in each patient.

Software and Data Analysis

Standardization of the technical tools is also necessary to advance the quantification of perfusion measurements. To ensure that these can also be used in everyday clinical practice, user-friendly software certified for diagnosis is required, additionally enabling the flexible integration of research innovations. For this reason, the commercial software Osirix (Version 5.6, Pixmeo Inc., Genève, Switzerland) and the open source equivalent software Horos (Version

3.0, horosproject.org, USA) was chosen for this work. The DICOM viewer meets the above mentioned requirements and is used in our Radiology department as well as by many others worldwide.

The in-house developed and certified perfusion plugin UMMPerfusion (Version 1.5.2) (Zöllner et al., 2016b) allows for executing several DCE MRI perfusion models simultaneously using the same ROIs during calculations. This is beneficial since the placement of the AIF and tumor tissue ROIs is crucial for a proper comparison of the models (Calamante, 2013). Furthermore, the selected signal curves are visualized immediately to directly detect and avoid selection errors. For compartment models, the plugin also enables an estimation of the Akaike information criterion (AIC) and chi square χ^2 of the fits assessing the goodness of fit as a parameter for model comparison (Luypaert et al., 2012). The calculation of hemodynamic parameters is feasible for an averaged ROI based fit as well as by pixel wise fitting of the corresponding model. For this purpose, the length of the baseline as well as the HCT and the used slices and time points can be selected. The boundary conditions for the respective fit can also be chosen manually.

Consequently, a comparison is possible with the same transparent and reproducible settings. Furthermore, changes or extensions of the plugin can be integrated reasonably uncomplicated.

Further statistics such as testing for normal distribution and t-test analysis was performed using MATLAB 2015 (Version 8.1.0.604, the Mathworks, Nattick, MA, USA).

3.2 DCE Perfusion Phantom Study

A controllable in vitro setup for system calibration, to optimize MRI quantification processes such as standardization of the acquisition procedure, as well as objective evaluation and comparison of pharmacokinetic models was developed. Therefore, a phantom was designed to generate reference measurements and ground truth data to assess the reproducibility of measurement protocols.

3.2.1 Phantom Design

As previously proposed by Heilmann et al. (2009) and Rajan et al. (2014), a hemodialysis filter was used as a basis for the perfusion phantom. The dialysis filter (Helixone FX 800, Fresenius Medical Care, Germany) was used to imitate tissue characteristics. It measures 25 cm in length with a diameter of 5 cm. Inside, it is built up with a bulk of parallel fibers close to the capillary size (diameter = 200 μm). The construction principle of the dialyzer enables the transfer of CA through a semipermeable membrane (pore diameter = 1.8 nm) from within the fibers to the surrounding space and thus provides two compartments. It exhibits a fixed permeability of the filter boundary, however the concentration gradient between the two chambers can be varied (Figure 3.9).

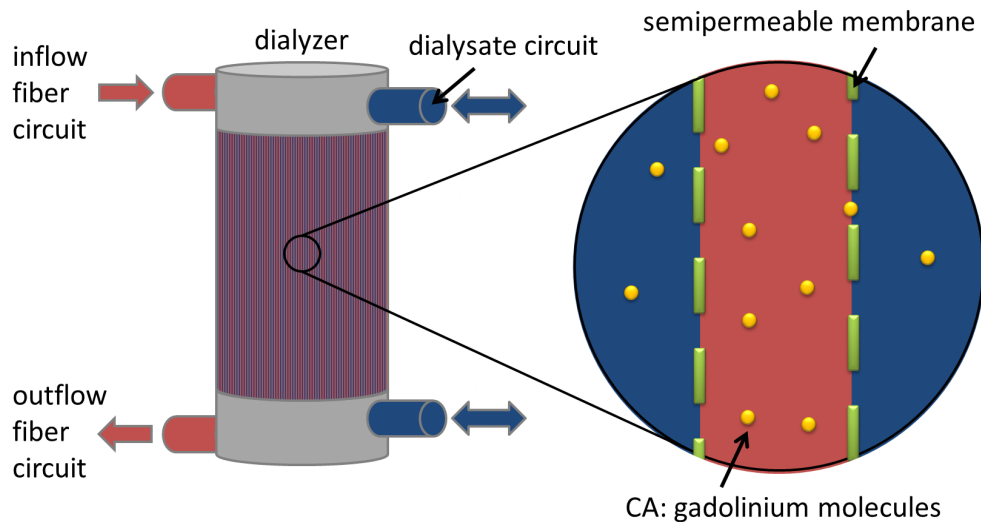


Figure 3.9: Construction scheme of the dialyzer. Two flow circuits are existent, the fiber circuit (red) and the dialysate circuit (blue). To simulate tissue characteristics with two compartments, a dialyzer with a semipermeable membrane (dashed green line) which can be passed by the CA molecules (yellow) was used.

Water was pumped from a bucket through an inflow silicone tube of 10 mm diameter (Festo Vertrieb GmbH & Co. KG, Germany) to the fiber compartment of the phantom. A peristaltic pump (Watson Marlow series 300, Watson-Marlow Ltd, United Kingdom) was used, which can be set to different pump rates. In a first step, the pump was calibrated to convert the arbitrary manufacturer specification into the actual flow rate, to find the appropriate velocity for the experiment and to ensure that the pumping capacity is constant. For this purpose, water was pumped from one reservoir into another at different set speeds while the time was stopped. The measured values were plotted against time and the velocities determined using a linear fit. The flow behavior was observed through the transparent tubes in the realistic measurement setup.

Each time before starting the actual measurement, the phantom was completely filled with water to make sure that no air is left inside the phantom. While pumping the water through the tube into the phantom, CA was injected automatically in the tube by a CA pump approximately 50 cm ahead entering the phantom when performing DCE measurements. Another outflow tube lead out of the phantom, transporting the water mixed with CA to a second bucket. The tube in front of the phantom inlet served as an artificial artery where the first pass of CA signal was measured and used to determine the AIF (Figure 3.10). For this purpose, the tube inlet was attached to the phantom in such a way that it was possible to measure the artificial artery and artificial tissue in one slice during the subsequent measurement. The second compartment, i.e. the compartment external to the dialysate fibers, can be connected by an additional circuit for particular experiments. An additional inflow and outflow tube are therefore connected to the respective connection points of the dialysis filter (Figure 3.11).

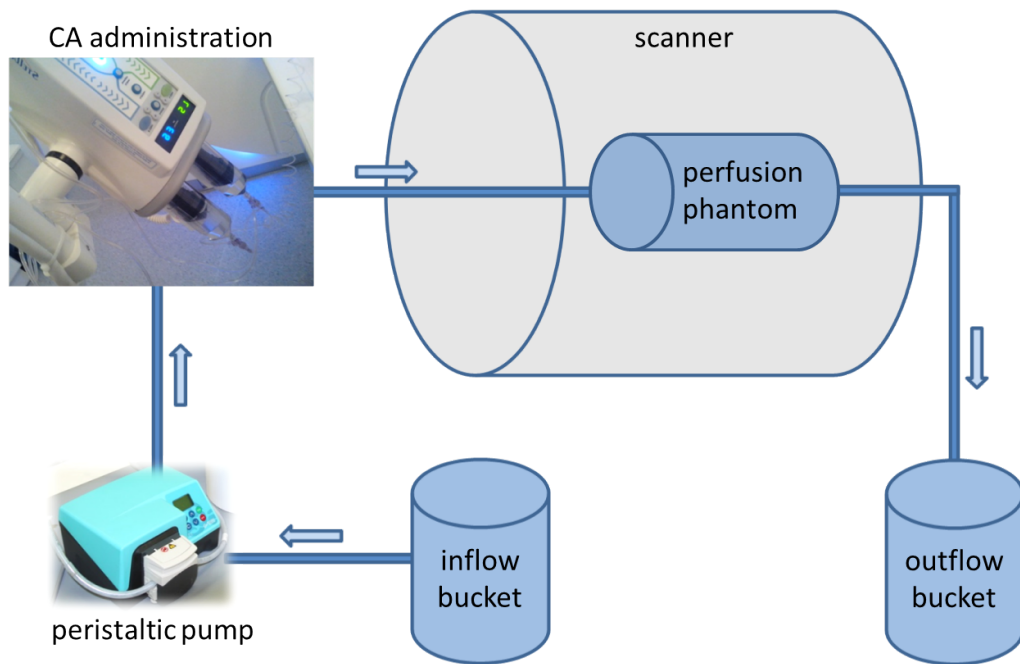


Figure 3.10: Experimental setup of the perfusion phantom in the scanner room. Water from the inflow bucket was pumped with a peristaltic pump into the phantom. CA could be injected automatically. Water mixed with CA was collected in an outflow bucket.

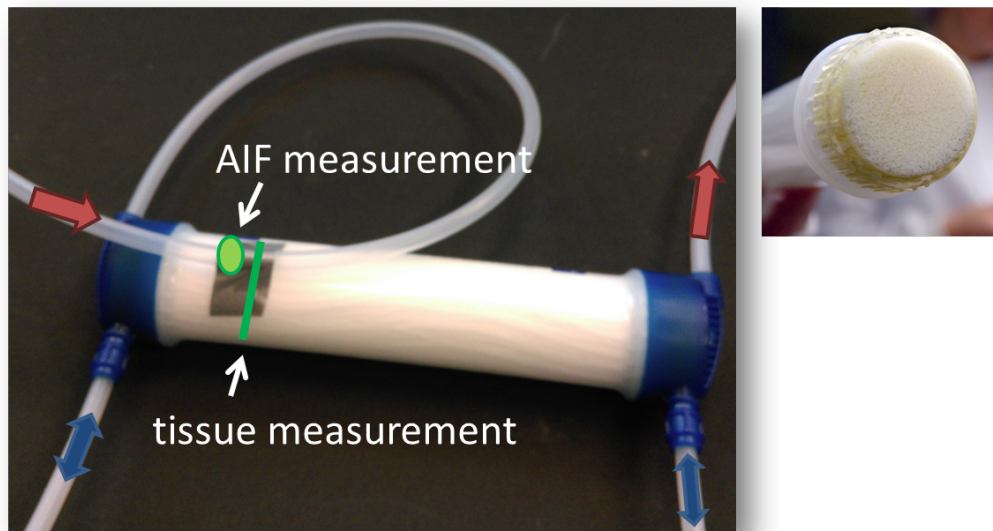


Figure 3.11: Utilization of the perfusion phantom. Two flow circuits can be addressed: The fiber circuit (red), with fibers depicted in the cross section of the dialyzer and the dialysate circuit (blue). The AIF was measured in the inflow tube shortly before entering the dialyzer together with the tissue function in the same slice (green).

Table 3.2: Imaging parameters of the quantitative DCE MRI phantom study.

Sequence	TE	TR	FA	matrix size	FOV	spatial resolution
TWIST	1.4 ms	3.8 ms	15°	128 × 128	(128 × 128) mm ²	(1 × 1 × 4) mm ³

3.2.2 Imaging Protocol

For a better comparability, all measurements were exclusively performed at the MAGNETOM Skyra scanner with the 15 channel phased array knee coil. To obtain high temporal and spatial resolution, the examination was performed with the 3D TWIST sequence, parameters are given in Table 3.2. Parallel imaging was used to achieve a high temporal resolution. Unless otherwise specified, a $PAT = 2$ was applied following the clinical protocol specification. Images were acquired in the transverse plane. Thus, the flow direction within the fibers intercepts the imaging plane. A continuous acquisition over a volume of 6 slices for 100 seconds with a nominal temporal resolution of 2 s per volume resulted in a total of 50 volumes. Right after the 5th volume had been acquired, 1 ml of a Gd based CA (Dotarem or Gadovist) was administered intravenously. It was followed by a 10 ml saline flush to ensure a coherent bolus during its passage. Both solutions were injected with a flow velocity of 1 ml/s.

For the evaluation of the measured DCE MRI data, the area of the AIF and the tissue volume was marked (Figure 3.12). The AIF was determined by placing a ROI in the tube in front of the phantom inlet. To avoid inflow effects and to minimize partial volume effects due to the small vessel diameter, a reasonable large tube was chosen and the ROI was measured in its center. The AIF and tissue volume was chosen on the same slice in the first third of the phantom length. OsiriX and its implemented perfusion plugin was used for the evaluation of perfusion parameters. All data were normalized by subtracting the mean intensity of five baseline volumes and a linear relationship of the CA concentration to the measured signal intensities was assumed.

3.2.3 Feasibility

It was examined whether the theoretical considerations could be implemented in practice. For this purpose three experimental setups were performed.

Setup 1: Washout The ability of Gd molecules to cross the semipermeable membrane was investigated. Thus, 5 ml of diluted CA (1:3) were injected into the fiber circuit of the phantom before the measurement. The input and output of the fiber circuit were closed and the phantom was connected to the tubes of the dialysate circuit. The dynamic DCE MRI measurement with the parameters described above and the pump for water transport were started simultaneously. It was observed whether the counter flow was capable of washing out the CA molecules migrated through the semipermeable membrane from the external dialysate circuit (Figure 3.13).

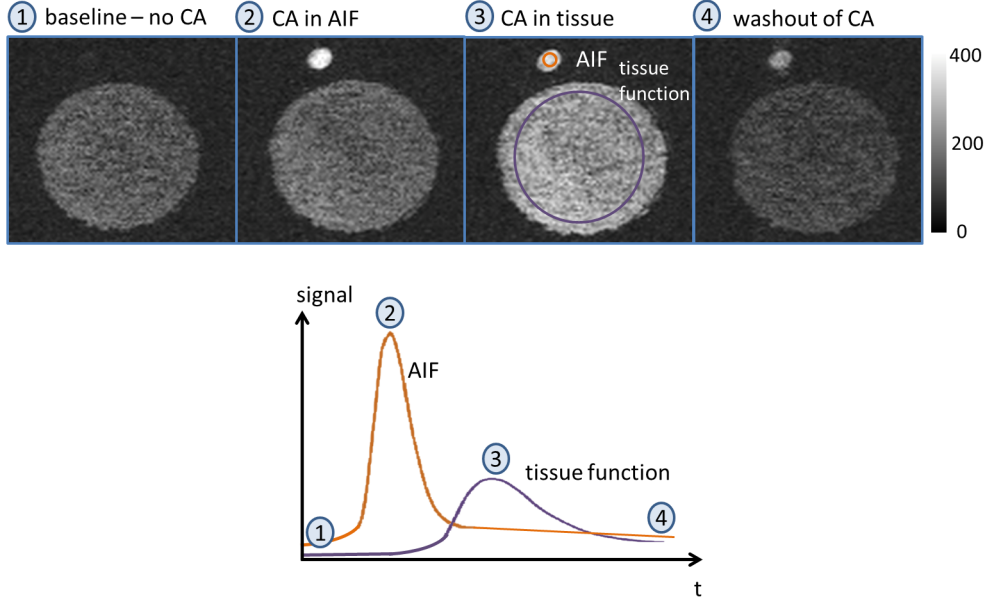


Figure 3.12: Evaluation of the acquisition data of the perfusion phantom. (1) Acquisition starts before CA administration to measure the baseline. (2) CA is injected and reaches the AIF (3) and shortly after the tissue. The ROI to determine AIF (orange) and tissue signal (purple) is placed in the same slice and remains constant for all measurements. Measurement continues until washout phase ends, e.g. the signal reaches baseline level again.

Signal over time of the acquired washout data was analyzed. For the quantification of the measured data, the clearance was determined analogously to (Rowland et al., 1973). Its value is expressed by the following differential equation which can be interpreted as the inverse of the removal rate of a substance from the body divided by its distribution volume

$$v \frac{dC}{dt} = -K \cdot C + \dot{m}. \quad (3.2.1)$$

Mass change \dot{m} is given in (mmol/min) or (mol/s), clearance K in (ml/min) or (m^3/s), concentration C in (mmol/l) and volume of distribution v in (l). Solving this equation results in

$$C = \frac{\dot{m}}{K} + \left(C_0 - \frac{\dot{m}}{K} \right) e^{\frac{K \cdot t}{v}} \quad (3.2.2)$$

with C_0 being the concentration in the beginning of the measurement. An exponential fit was performed on the measured data points to determine the corresponding parameters.

Setup 2: AIF and tissue measurement The aim was to verify whether the phantom is capable of producing realistic AIF curves and tissue curves. Turbulence in the tube or bending or sinking of the CA in the phantom caused by insufficient pressure or unsuitable phantom size and shape would change the signal curves. They would no longer show the behavior described in [subsection 2.4.3](#). The dialysate circuit was locked for this purpose. Water and

CA with the settings described above were pumped through the fiber circuit (Figure 3.13). Four different pumping velocities of $v = (12, 14, 16, 20)$ ml/s were chosen. The ROIs of AIF and tissue were selected once and kept in the same way for all velocities. A simplified gamma variate fit according to Chan and Nelson (2004) was performed

$$\Gamma(t) = \epsilon, \quad t \leq \tau \quad (3.2.3)$$

$$\Gamma(t) = \epsilon + (\Gamma_{\max} - \epsilon) e^{\alpha \left(1 - \frac{t - \tau}{t_{\max} - \tau}\right)} \left(\frac{t - \tau}{t_{\max} - \tau}\right)^{\alpha}, \quad t > \tau. \quad (3.2.4)$$

ϵ is the baseline of the signal, the curve is starting at time τ , the signal maximum is at Γ_{\max} , t_{\max} is the time the maximum is reached and α defines the shape of the function. Start of the CA signal curve, time of maximum as well as peak height was compared for the AIF and the tissue signal.

Setup 3: Full performance evaluation Both previous approaches were combined. The aim was to investigate the effects of an additional flow of water through the dialysate circuit on the signal generated by the flow through the fiber circuit. Two settings were investigated. The additional flow was incorporated in same- and counter direction to realize fluid exchange in the two compartments (Figure 3.13).

3.2.4 Reproducibility

The ability of the phantom to provide quantifiable and reproducible perfusion maps was investigated. With the standard settings described above and in experimental setup 2, the measurement was repeated five times during one measurement cycle to determine the inter measurement reproducibility. Based on the results of the feasibility tests, the pump speed was set to 16 ml/s for the following experiments. One week later, the same measurement was repeated to check if the results were reproducible over time. The phantom was positioned as identically as possible in the knee coil and in the scanner in general. Thus the same ROI for AIF and tissue as in the measurement one week before could be used. The 2CX was applied and pixel wise fits were performed. The perfusion parameters PF, PV and MTT as well as the permeability parameters EF and PSAP were determined and the fit accuracy was evaluated using AIC and χ^2 . Parameter maps were created and the mean values and standard deviations of the tissue ROIs were calculated.

Setup 3 was adjusted to compare both settings quantitatively. A pixel wise 2CX fit was applied to create perfusion, permeability and fit maps. The calculated mean and standard deviation was opposed to those obtained with setup 2.

3.2.5 Temporal Resolution and PAT

The influence of different sampling rates on the perfusion parameters and their fit quality was investigated. The different sampling resolutions T_s were achieved by varying the PAT factor. Imaging parameters were maintained from previous

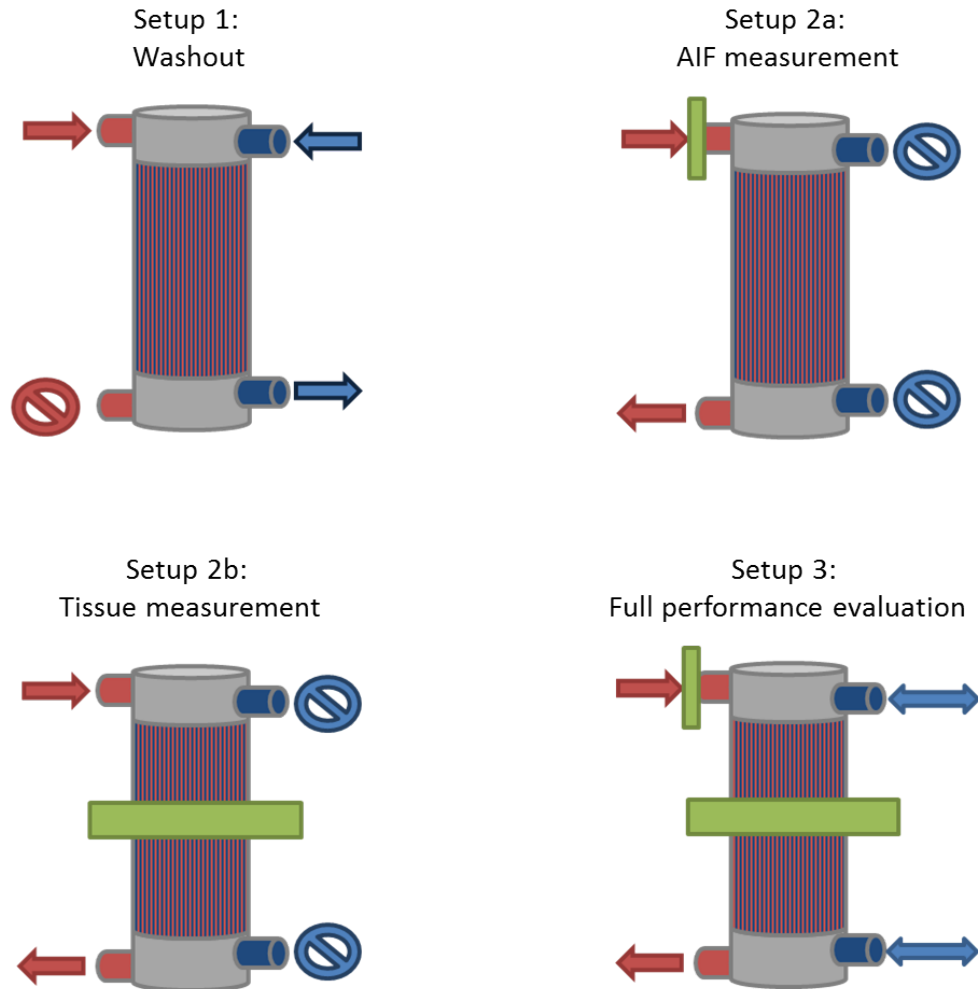


Figure 3.13: Experimental setups for the perfusion phantom study. The red arrows and dialyzer entrance indicate the flow circuit through the fibers, the blue ones the flow circuit through the dialysate circuit. Slabs in green show the measured slice of AIF and tissue.

Setup 1: Measurement of the washout curve to investigate the ability of gadolinium molecules to cross the semipermeable dialyzer membrane.

Setup 2a: Measurement of an artificial AIF.

Setup 2b: Measurement of an artificial tissue function.

Setup 3: Measurement of the artificial tissue function with an additional flow through the dialysate circuit in flow and counterflow direction.

experiments and can therefore be found in [Table 3.2](#). The total measurement time for each measurement was 1 minute, whereby the different temporal resolutions $T_s = (3.8, 2.7, 2.3, 2.1, 2.0, 1.9)$ s were achieved. These corresponded to parallel imaging factors $PAT = (1, 2, 3, 4, 5, 6)$. The inter- and intra-measurement precision of the PF depending on the sampling resolution was investigated.

1: Intra measurement precision To investigate the homogeneity within a single measurement, the intra measurement precision was determined by the standard deviation σ_{intra} of the PF in each ROI of the pixel wise fit such as the mean fit quality χ_{intra}^2 .

2: Inter measurement precision Measurements were repeated five times for each PAT setting to determine the inter measurement precision by the standard deviation of the mean values $PF_{\text{inter}} \pm \sigma_{\text{inter}}$ among each other.

Statistical analysis was performed for all above-mentioned quantities with an unpaired t-test ($P < 0.05$) in Matlab.

3.2.6 Application for ASL

The feasibility of the phantom for perfusion measurements using ASL and a comparison to the results obtained with DCE measurements was evaluated. For this purpose, ASL measurements were performed in the same measurement session and with the same experimental settings as the conventional DCE measurements. The selected experimental design offers the advantage that the complete experimental setup needs hardly any modifications. The access for the CA is no longer required and plugged off. An AIF no longer needs to be measured. Since the tube does not affect the image quality, the setup is not changed in order to ensure same setup alignment for comparability.

A PASL sequence was used with parameters given in [Table 3.3](#). It creates a perfusion-weighted image from the signal difference between control and label acquisition. This perfusion-weighted image data was used to calculate a PF map pixel by pixel applying the following formula ([Alsop et al., 2015](#))

$$PF = \frac{\lambda}{2\alpha \cdot T_{\text{IF}}} \cdot \frac{\Delta M(T_{\text{IF}})}{M_0} \cdot \exp\left(\frac{T_{\text{IF}}}{T_1}\right) \quad (3.2.5)$$

with the plasma flow PF in ml/100 g/min, the blood-tissue water partition coefficient $\lambda = 0.9$ ml/100 g, the inversion efficiency $\alpha = 0.98$, the prescan image M_0 and the control-label image $\Delta M(T_{\text{IF}})$. The longitudinal relaxation time of the tissue T_1 was set to 4000 ms for water and the inversion time T_{IF} was set to 2400 ms.

PF was determined by placing a ROI in the calculated map. Results regarding mean value and standard deviation were compared to those of the DCE measurements.

Table 3.3: Imaging parameters of the quantitative ASL MRI phantom study.

Sequence	TE	TR	FA	matrix size	FOV	spatial resolution
PASL	37.96 ms	7000 ms	180°	128 × 64	(288 × 144) mm ²	(2.25 × 2.25 × 5) mm ³

3.2.7 Application for DCE CT

The material properties of the phantom make CT measurements feasible. An important difference to consider here is the applied CA. The Gd containing MR CA was replaced by the iodine containing CA used in CT. Physiologically, this molecule also is able to penetrate the artificial endothelial wall. The size of the semipermeable membrane of the phantom capillaries permit a transfer in theory. To verify these assumptions, setup 1 and 2 of the feasibility and reproducibility measurements with the MR were repeated with the CT scanner.

Setup 1: Washout First, it was examined whether iodine molecules can cross the semipermeable membrane. Thus, 5 ml of diluted CA (1:3) of the CA were injected into the fiber circuit of the phantom before the measurement. The setup was identical with the one described in [Figure 3.13](#). The corresponding acquisition parameters are given in [Table 3.4](#). The measurement took 40 s with a measurement every second, resulting in a dose of about 100 mGy. Longer measurement times were not possible due to the restrictions of the scanner, thus this setting differs in comparison to the MR measurements. Signal evaluation of the acquired washout data was analyzed and compared quantitatively to the results of the MR measurement. Therefore the exponential fit was performed analogue to the MR measurement to obtain parameters such as clearance.

Setup 2: AIF and tissue measurement It was reviewed whether the phantom is capable of producing realistic AIF and tissue curves for CT measurements. Therefore the experimental setups as described in [Figure 3.13](#) were used in the CT scanner. Three different pumping velocities with $v = (16, 18, 20)$ ml/s were chosen. A gamma variate fit to investigate start of the CA signal curve, time of maximum as well as peak height for the AIF and the tissue signal was performed according to [Equation 3.2.4](#). This experiment was especially crucial as the iodine containing CA has a higher viscosity than the Gd containing one. A sticking or clogging should therefore be excluded. Quantitative perfusion maps of PF, PV and MTT using the FD method were produced. CM could not be applied since the evaluation is not yet possible with the Osirix plugin. Mean values and standard deviations were calculated and compared with the MR results.

Table 3.4: Imaging parameters of the quantitative DCE CT phantom study.

Sequence	tube voltage	tube current	matrix size	FOV	spatial resolution
standard abdomen	70 kV	150 mAs	512 × 512	(1024 × 1024) mm ²	(2 × 2 × 2) mm ³

3.3 DCE in Vivo Study in Rectal Cancer Patients

Perfusion measurements of patients with rectal carcinoma were evaluated using the DCE technique. They were acquired in clinical routine as qualitative pre-treatment scans. In this study they are quantitatively evaluated in the context of future improvements of the measurement workflow and to extend the scope of applications.

3.3.1 Patients

The prospective single-center study was approved by the Institutional Review Board (Medizinische Ethikkommission II, Medical Faculty Mannheim, Heidelberg University, Germany) and written, informed consent of all patients was obtained. All analyses were carried out in accordance with the ethics board approval. 26 patients with newly-diagnosed untreated rectal cancer were enrolled within a period of 2 years (December 2013 to December 2015) and underwent MRI of the pelvis including perfusion sequences covering their tumor. Eight patients had to be excluded from the study due to poor image quality. This resulted in final evaluation of 13 male and 5 female patients with a mean age of 64 ± 10 years. The tumor grade was staged T2 (4 patients), T3 (13 patients) or T4 (1 patient).

3.3.2 Data Acquisition

Acquisition Parameters

DCE MRI data was acquired with a 3T scanner either MAGNETOM Skyra or MAGNETOM Tim Trio depending on the availability of the device in clinical routine and without further specific indication. A standard spine coil and body coil were used. To obtain high temporal and spatial resolution, the examination was performed with a 3D TWIST sequence, according imaging parameters are given in [Table 3.5](#). Images were either acquired in axial plane or tilted in direction of the coronal plane to cover the tumor best as possible. A continuous acquisition over a volume of 20 slices for 5 minutes and 50 seconds with a nominal temporal resolution of 5 s per volume resulted in a total of 70 volumes. Right after the 10th volume had been acquired, 3 - 18 ml (0.1 to 0.15 ml per kg body weight) of Gd based CA Dotarem or Gadovist were administered intravenously and followed by a 40 ml saline flush. Both solutions were injected with a flow velocity of 1.5 ml/s.

Table 3.5: Imaging parameters of the quantitative DCE MRI in vivo study in rectal cancer patients

Sequence	TE	TR	FA	matrix size	FOV	spatial resolution
TWIST	1.44 ms	3.6 ms	15°	192 × 144	(260 × 158) mm ²	(1.4 × 1.1 × 3.5) mm ³

Signal Analysis

Both the healthy rectal wall and the tumor are supplied by several arteries. The aorta abdominalis, which originates from the center of the body, branches out symmetrically to the left and right side of the abdomen into several smaller vessels. The rectal wall is therefore supplied by many individual arteries with different points of attachment. During evaluation of measured DCE MRI data, the area for AIF determination and the tumor volume was initially marked in a anatomical T_2 -weighted image with high spatial resolution for a precise selection. The result was then transferred to the T_1 -weighted TWIST image (Figure 3.15). The AIF was determined by carefully placing a ROI in the arteria iliaca externa (Figure 3.14) to avoid inflow effects and to minimize partial volume effects due to the small vessel diameter. It was determined by a region growing algorithm with manually set thresholds. Analysis of DCE MRI data was performed for all patients where a ROI could be placed in the left as well as the right side iliac artery and produced an AIF. The tumor volume was chosen on the slice with the largest tumor intersection and the whole volume was outlined under supervision of a radiologist with three years of experience in abdominal imaging using OsiriX and the implemented perfusion plugin. All data were normalized by subtracting the mean intensity of five baseline volumes and a linear relationship of the CA concentration to the measured signal intensities was assumed.

3.3.3 Bilateral Blood Supply and AIF Selection

The discrepancy of quantitative perfusion parameters dependent on the chosen artery used as AIF was investigated.

The selection of the ROIs is shown for a representative patient in Figure 3.15. The signal over time of left and right AIF was compared for every patient qualitatively. Quantitative analysis of the DCE MRI image data was performed using the three above mentioned approaches: a voxel-by-voxel FD approach, a model based 2CU and a model based 2CX. PF, PV and MTT were calculated using left and right side AIF as well as the permeability parameters PSAP and EF. The fit quality of the parameters dependent on AIF selection was compared afterwards. As an alternative to selecting one AIF, a combination of both AIFs for a better representation of the actually arriving blood and CA bolus was investigated. Subsequently, the mean of the combined areas of both arteries was determined. For this purpose, the average of all pixel values in the two ROIs was calculated by $AIF_{new} = \text{mean}(AIF_{left} \cup AIF_{right})$. This new AIF was then used to recalculate the parameters previously listed.

First, the results of the individual patients were evaluated. Furthermore, the averaged effects of the entire study group were analyzed applying a box plot. For a statistical analysis a paired t-test was performed to determine if there was a significant difference between one-sided calculation of AIF and averaged AIF utilization. The significance level was set to $P < 0.05$.

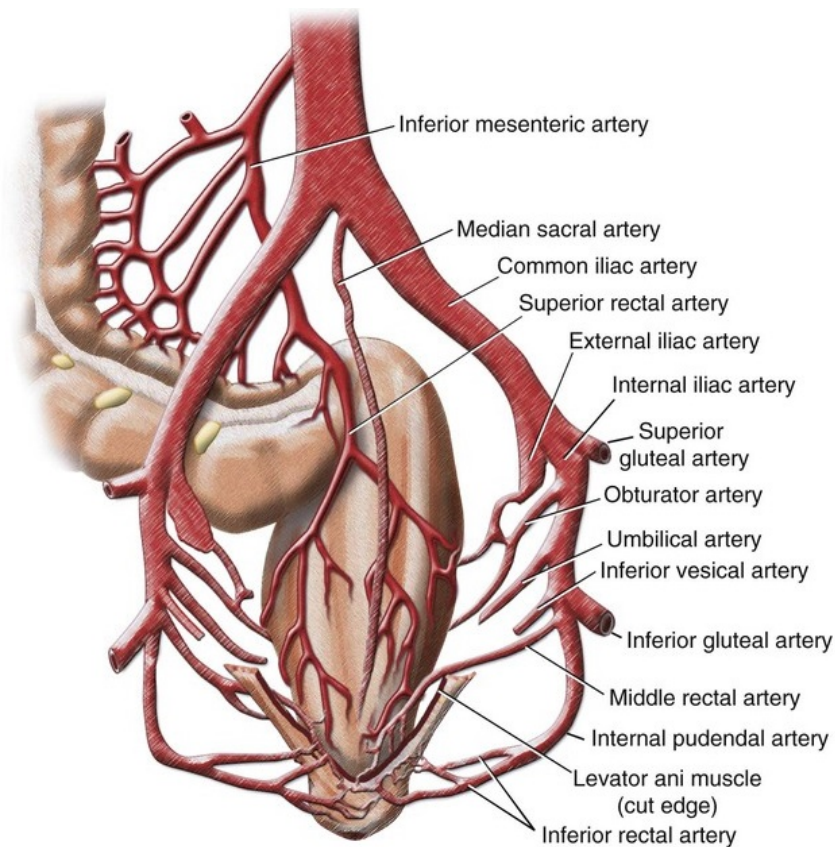


Figure 3.14: Anterior view of the anatomical structure of the rectum with the main feeding arteries. Blood supply is branched symmetrically to the left and right side of the abdomen into several smaller vessels (Sabiston et al., 2001).

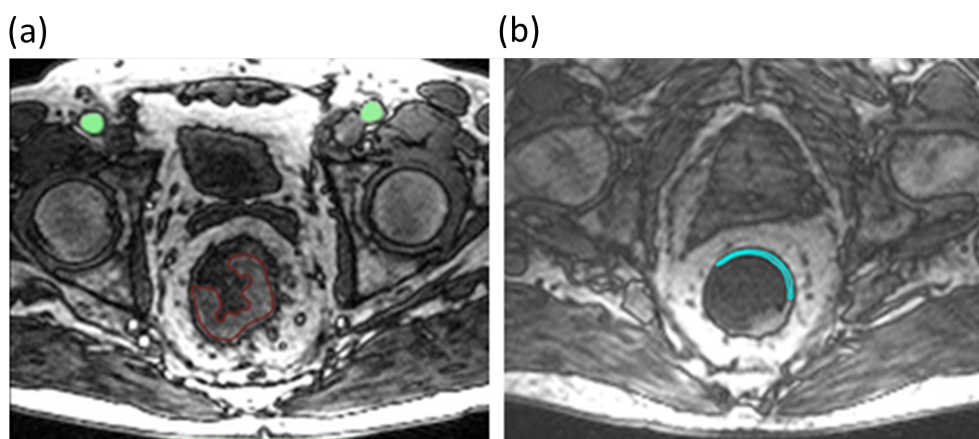


Figure 3.15: MR image of the abdomen of a representative patient with rectal tumor. (a) ROI for AIF and tumor were identified on the slices with their best representation. The AIF (green) was determined by a region growing algorithm with manually set thresholds. The tumor ROI (red) was manually outlined. ROI selection was performed in consensus with a radiologist. (b) Healthy rectum wall outlined as reference performed in consensus with a radiologist.

3.3.4 Compartment Models and Model Free Approach

Different pharmacokinetic models for quantitative DCE analysis were investigated. As a reference, the voxel-by-voxel FD approach mostly used in daily clinical practice for T_1 -weighted DCE MRI was used. The model based 2CU and a model based 2CX were compared to those results.

To account for both supplying arteries, the combined signal of the AIF ROIs was used to calculate an averaged AIF over all voxels based on the results of [subsection 3.3.3](#). All other settings and ROIs were maintained from the above study to calculate perfusion parameters PF, PV and MTT and permeability parameters PSAP and EF. The AIC and χ^2 were obtained to estimate the goodness of the fit.

To obtain a tissue comparison, a ROI was placed in healthy rectum tissue of 10 patients and mean perfusion parameters were obtained ([Figure 3.15](#)). The rectal wall is generally rather thin. In addition, acquired slices are those containing the tumor in which the healthy wall has receded even further. The number of evaluable pixels was very small in some patients and not representative. Therefore, this comparative measurement could not be carried out in the entire patient cohort. The evaluation was performed analogous to the evaluation of the tumor tissue described above.

A statistical analysis of the data was performed. Bland Altman plots were generated to analyze perfusion parameters for every single patient for all possible pairs of two different models, respectively. Lilliefors test was conducted to test for normal distribution within the three groups. Since not all data was normally distributed, nonparametric paired Wilcoxon sign rank test was employed for further analysis of the quantitative perfusion values within different models. The average values in each of the ROIs were compared for this test. A significance level of $P < 0.05$ was set. The severeness of the tumor of the patient cohort was divided into tumor stages. The mean values of the perfusion parameters were additionally determined separately according to this classification and compared with the total mean.

3.3.5 2D and 3D Evaluation

The influence of quantitative 3D volume DCE MRI in rectal cancer on perfusion parameters was investigated and compared to the data obtained by selecting a single 2D tumor slice.

Due to artifacts or insufficient coverage of the tumor on several slices, this investigation was conducted only on five patients (5 male, 64 ± 5 years) whose tumor was well recognizable on several slides. The settings and AIF ROIs were maintained from the above study.

The tumor tissue ROI was selected within the tumor volume by a performing physician according to the standard clinical procedure of analyzing DCE MRI data using only one slide. In the same way as in daily clinical practice, the choice

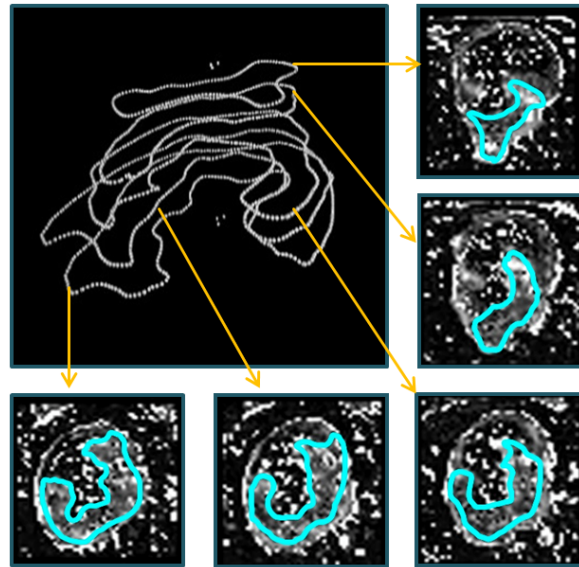


Figure 3.16: Three dimensional representation of the tumor volume consisting of five subsequent slices of signal data acquired with TWIST of a representative patient.

of one particular slice depended on the performing physician. Hereinafter, four additional ROIs were drawn on slices around the selected central tumor slice to delineate the entire tumor volume (Figure 3.16). Perfusion parameters (PF, PV, MTT) in the tumor were calculated pixel wise for each individual slice separately using the 2CU. The mean values of areas of the slices within the volume were calculated and the relative deviation of the smallest to the largest area as well as from the single slice chosen initially by the physician to the mean was calculated.

3.3.6 Comparison DCE CT

In order to obtain more tissue information, an additional perfusion CT scan was performed on the patients in this study. Volume perfusion CT was acquired on the Somatom Force CT system. The tube voltage varied between 80, 90 or 100 kVp and a tube current of 220, 150 or 100 mAs respectively, depending on the patient's body weight. The slice thickness was 1.5 mm. 50 ml of the intravenous CA Imeron with an iodine concentration of 400 mg iodine/ml were automatically applied with a following 50 ml saline flush. The scan was started 5 s after the start of CA injection. The temporal resolution was 1.5 s and a total of 19 scans were taken. After the measurement, an algorithm for noise reduction and an algorithm for motion correction (Siemens syngo.via CT Body Perfusion VA30, Siemens Healthineers, Erlangen, Germany) were automatically performed. It was attempted to find a comparable slice to the MR evaluation and to select AIF and tumor ROI similarly (Figure 3.17). Since the evaluation with CM for CT data is not yet possible with the Osirix plugin used here, the perfusion values could only be determined with the FD approach. PF, PV and MTT were estimated in tumor tissue and normal rectal wall and were compared with the determined MR values.



Figure 3.17: CT image of the abdomen of a representative patient with rectal tumor. (a) AIF and tumor were identified on the slices with their best representation. The AIF (orange) was determined by a region growing algorithm with manually set thresholds. The tumor ROI (purple) was manually outlined. ROI selection was performed in consensus with a radiologist.

Results 4

The results of this thesis are given in this chapter. Following the order of the last chapter, results of general calibration is given first. Afterwards the investigation of the designed perfusion phantom on feasibility and reproducibility in DCE MRI and application for other imaging techniques is given. The last part deals with the results of the DCE MRI in vivo study on rectal cancer patients of which parts have been published in ([Gaa et al., 2017](#)).

4.1 Contrast Agent Calibration

MR CA Calibration

For calibration, the signal intensities of the successively measured samples were plotted against their concentration ([Figure 4.1](#)). The diagram shows a steep increase, followed by a plateau region and a subsequent decrease of the signal with an increase of concentrations. A linear relationship between concentration and signal can thus not be assumed in principle. Zooming to smaller concentrations up to 2 mmol/l, an approximately linear course can be observed. This behavior corresponds to that described in the literature ([Shahbazi-Gahrouei et al., 2001](#)) for Gd containing CA in MR. Since the linear range covers the CA concentrations commonly used in clinical routine, no further correction methods were used and a linear characteristic was assumed in the following.

CT CA Calibration

The signal intensities of iodine containing CA probes was plotted against their concentration ([Figure 4.2](#)). The measured data points follow a linear slope. This is in accordance with [Hansen et al. \(2014\)](#), who additionally showed that higher tube voltages lead to a steeper slope, however, they should be avoided as they result in a higher patient dose. Due to the linear relationship for the measured clinically used CA concentrations further correction methods were not applied.

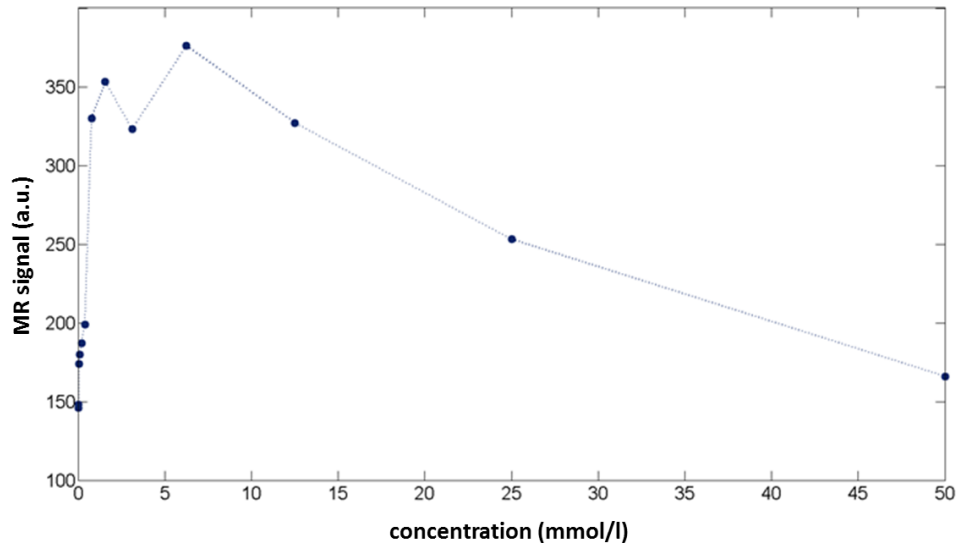


Figure 4.1: Calibration of the relationship between the concentration of the Gd containing CA Dotarem and the measured signal in MRI using a CA phantom.

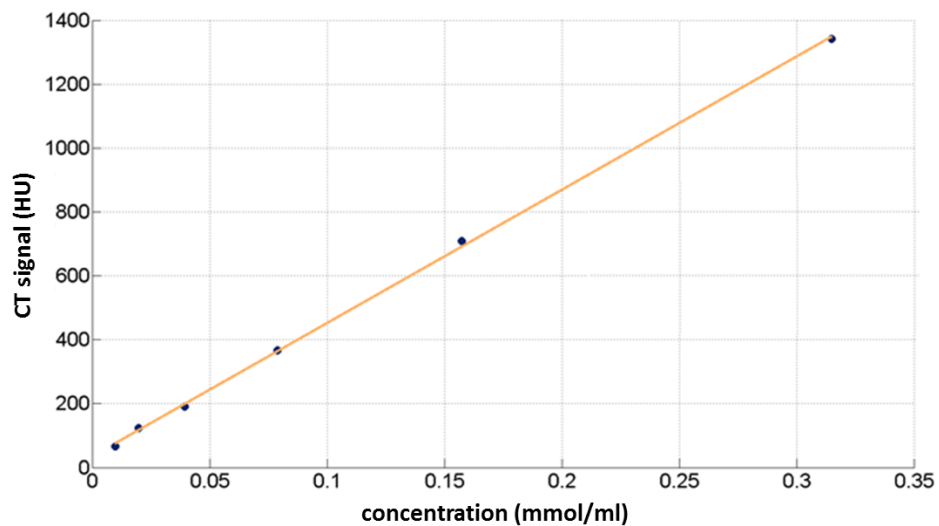


Figure 4.2: Calibration of the relationship between the concentration of the iodine containing CA Imeron and the measured signal in CT using a CA phantom.

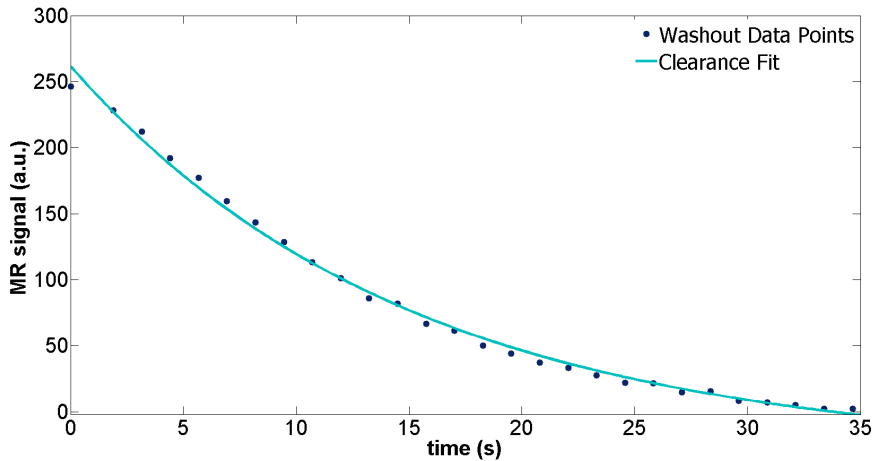


Figure 4.3: Experimental setup 1: Washout. A signal decrease is caused by CA transfer through the semipermeable membrane from fibers to dialysate space and subsequent washout. The data points follow a typical clearance function.

4.2 DCE Perfusion Phantom Study

4.2.1 Phantom design

The calibration of the peristaltic pump was performed, feasible velocities between 12 ml/s and 20 ml/s were found. These correspond to the order of magnitude of blood flow velocities in the human body in larger arteries. At lower speeds, the pressure of the pump is not sufficient to overcome the differences in height in the measuring setup and air bubbles are created in the tube. At higher speeds, the vibrations of the pump are transferred to the tube to such an extent that movement artifacts are introduced during AIF and tissue signal measurement (Figure 4.4).

4.2.2 Feasibility

Setup 1: Washout The CA stored in the fiber circuit in the phantom causes a high signal intensity in the measured T_1 -weighted MR signal at $t = 0$ s. The subsequent washout by the water flow through the dialysate circuit is expressed in a decreasing signal (Figure 4.3). The measured signal data points follow a typical clearance function. The performed fit revealed a clearance of $K = 207$ ml/min according to the formula described in Equation 3.2.2.

Setup 2: AIF and tissue measurement Evaluation of the measured signal could demonstrate that the phantom generates artificial AIFs and tissue functions with characteristic first pass - the steep increase in the signal - and typical washout slopes for all tested flow velocities (Figure 4.4). Results of the gamma variate fit are given in Table 4.1. The start time τ of the AIF signal curve is consistent for all four velocities. The height of the maximum Γ_{\max} increases with higher velocities and the time of the maximum t_{\max} is reached slightly earlier for higher velocities. In the tissue, the start time τ is delayed for

Table 4.1: Results of the gamma variate fit used for AIF and tissue data points for different flow velocities. The start time τ , the height of the maximum Γ_{\max} and the time of the maximum t_{\max} are given.

flow velocity	12 ml/s	14 ml/s	16 ml/s	20 ml/s
AIF				
τ (s)	17	17	17	18
Γ_{\max}	634	783	915	1090
t_{\max} (s)	21	21	20	20
tissue				
τ (s)	25	24	22	21
Γ_{\max}	66	62	60	59
t_{\max} (s)	33	32	29	26

lower velocities. The height of the maximum Γ_{\max} increases slightly with lower velocities and the time of the maximum t_{\max} is reached earlier for higher velocities. The tissue signal intensities are reduced and the curve width is broadened compared to the AIF signal.

Setup 3: Full performance evaluation Identical effects on the tissue function for additional flow in the dialysate circuit both in same direction and counter direction to the flow in the fibers were revealed. The additional flow leads to a reduced overall signal, it decreased from 55 a.u. to 28 a.u. for both flow directions. A reduced slope in the wash in phase and a faster decay was measured and is depicted in [Figure 4.5](#).

4.2.3 Reproducibility

In [Figure 4.7](#), the pixel wise calculated parameter maps and in [Table 4.2](#) the corresponding mean values with standard deviation in the tissue ROI of the five subsequent reproducibility measurements for the perfusion parameters PF, MTT and PV are given. Additional information about the extravasation of the CA into the dialysate circuit could be obtained by fitting the 2CX. Mean values with standard deviation of PSAP and EF have been calculated. The fit quality was determined with AIC and χ^2 . A representative fit using the 2CX is depicted in [Figure 4.6](#). The five measurements were averaged, the percentage standard deviation of the mean are 8 % for PF, 6 % for PV, 13 % for MTT. The deviation of the PSAP was highest with 18 % and the standard deviation of EF was 12 %. Values are given in [Table 4.3](#).

Here, also the results of all parameters for the second measurement after one week are depicted and can be compared to the mean and standard deviation of the five measurements the week before. PF stays constant compared to the mean of the five measurements at $t = 0$. All other values show a decrease of $\Delta PV = 22$ %, $\Delta MTT = 10$ %, $\Delta PSAP = 5$ % and EF $\Delta EF = 10$ %. The AIC is slightly decreased by less than 5 %, χ^2 is within the results of the earlier

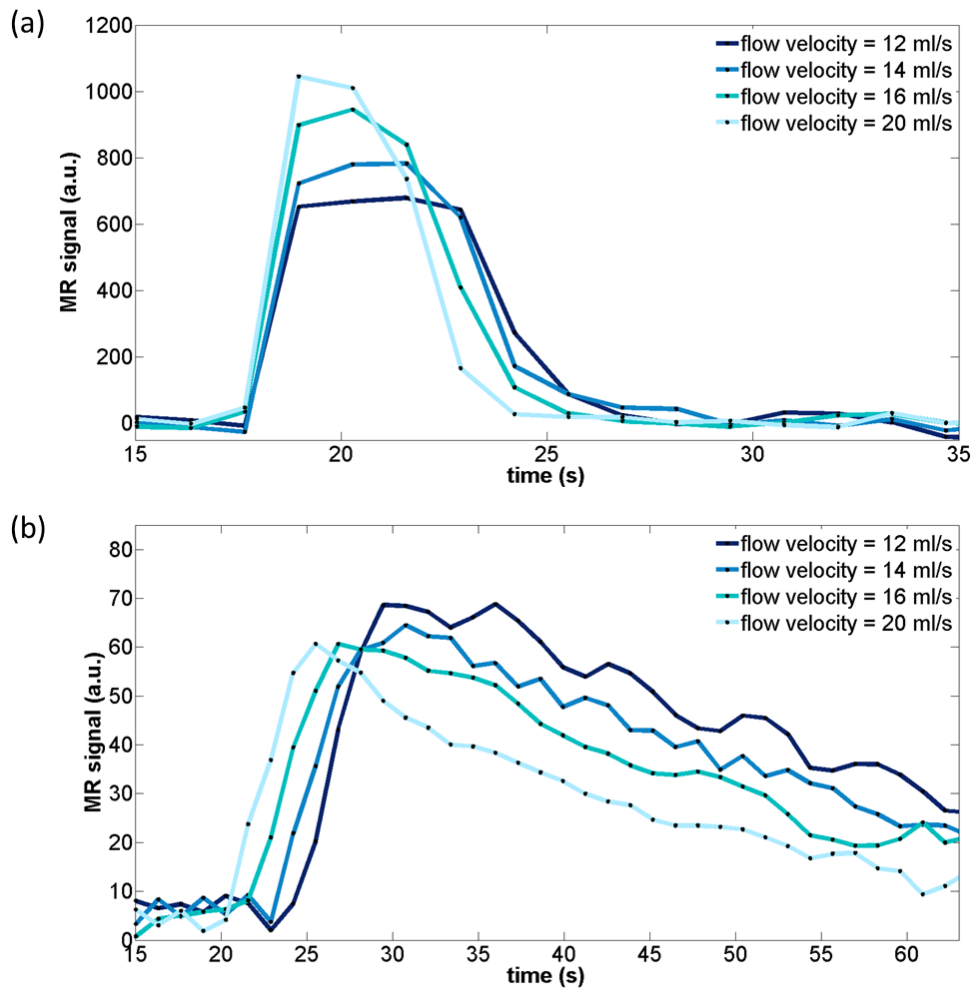


Figure 4.4: (a) Plot of the MR signal in the phantom's artificial artery over time for four different flow velocities resulting in AIFs and (b) signal in the phantom's artificial tissue region over time for four different flow velocities resulting in typical tissue functions. A delay and broader distribution can be observed for lower velocities.

measurement. All measured values lie within the standard deviation.

When the experiment was switched to setup 3, the calculated perfusion values with additional flow in same/counter direction showed a decrease of (36/43) % for PF and (52/26) % for PV. MTT remains constant. PSAP decreases by (67/76) % and EF by (17/26) %. The AIC decreases by (57/50)%, χ^2 is higher for flow in same direction and reduced for flow in counter direction by (16/33) % (Table 4.3).

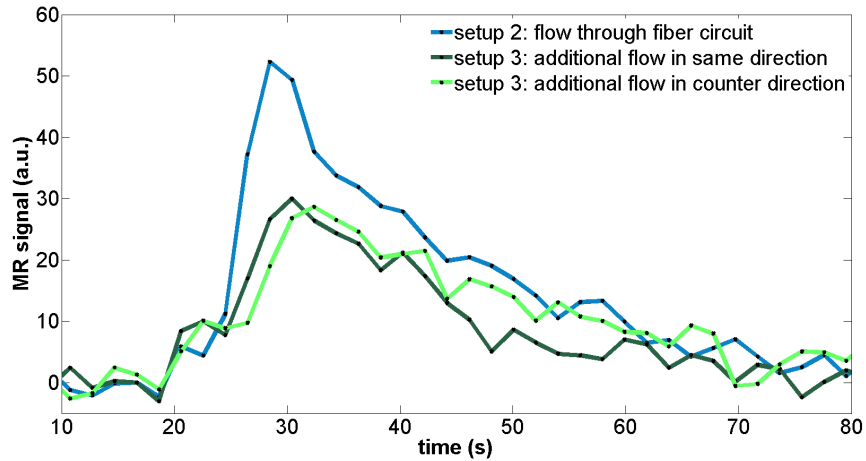


Figure 4.5: Plot of experimental setup 2: The tissue signal in blue caused by flow through the fiber circuit and plot of experimental setup 3: Changed tissue signal due to additional flow in the dialysate circuit in same and counter direction of the fiber circuit. The additional flow leads to a reduced overall signal and a faster decay.

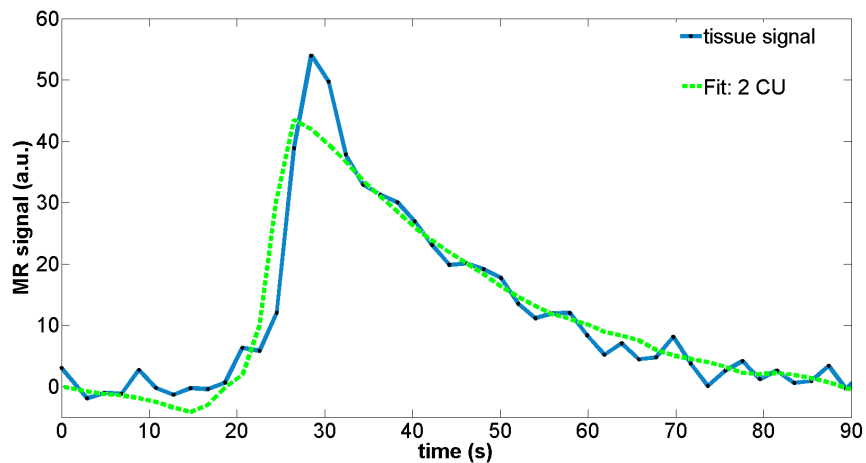


Figure 4.6: Phantom tissue signal produced with setup 2 and fit curve obtained with the 2CX.

Table 4.2: Mean \pm standard deviation of pixel wise calculated results for PF, PV, MTT, PSAP, EF, AIC and χ^2 using the 2CX. The results were obtained in a single measurement session. The five subsequent measurements were performed without modification in the setup.

	1	2	3	4	5
PF (ml/100 ml/min)	104 \pm 34	91 \pm 29	89 \pm 27	87 \pm 26	85 \pm 19
PV (ml/100 ml)	73 \pm 30	61 \pm 22	68 \pm 28	68 \pm 28	72 \pm 29
MTT (s)	28 \pm 12	27 \pm 8	28 \pm 10	34 \pm 13	30 \pm 9
PSAP (ml/100 ml/min)	51 \pm 35	34 \pm 30	32 \pm 24	36 \pm 30	42 \pm 26
EF (%)	29 \pm 12	21 \pm 16	25 \pm 17	25 \pm 18	28 \pm 18
AIC	302 \pm 16	307 \pm 15	310 \pm 15	312 \pm 16	315 \pm 15
χ^2	6 \pm 2	4 \pm 2	6 \pm 1	6 \pm 2	7 \pm 2

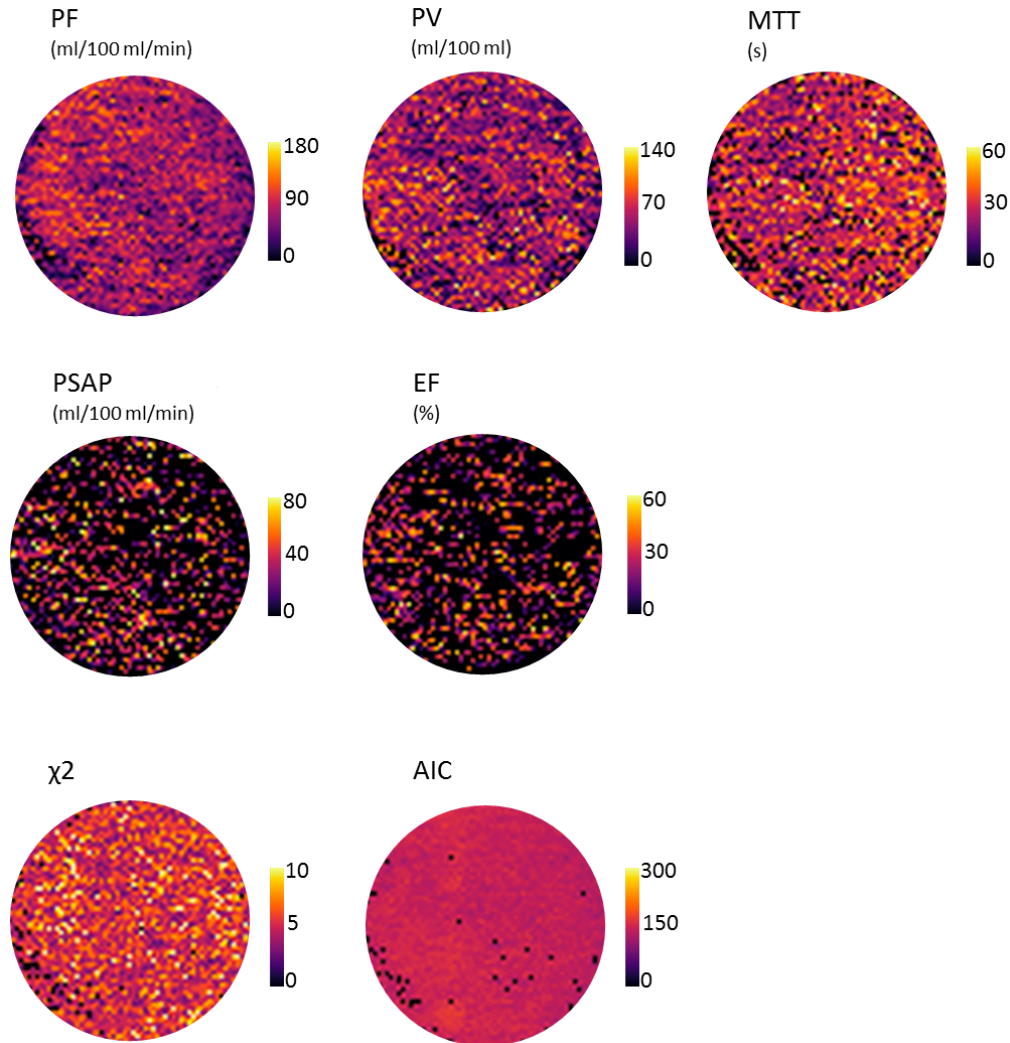


Figure 4.7: Pixel wise fitted maps in the artificial tissue by applying the 2CX. Perfusion parameters PF, PV, MTT in the first row, permeability parameters PSAP and EF in the second row and χ^2 and AIC to determine the goodness of fit in the third row.

Table 4.3: Mean \pm standard deviation of pixel wise calculated results for PF, PV, MTT, PSAP, EF, AIC and χ^2 using the 2CX. The left side shows the mean of the five subsequent measurements \pm standard deviation of the mean in the first week at $t = 0$. The right side shows mean \pm standard deviation one measurement after 1 week.

	$t = 0$	$t = 1$ week
PF (ml/100 ml/min)	91 ± 7	91 ± 26
PV (ml/100 ml)	68 ± 4	53 ± 23
MTT (s)	29 ± 4	26 ± 11
PSAP (ml/100 ml/min)	39 ± 7	37 ± 26
EF (%)	26 ± 3	23 ± 19
AIC	309 ± 4	299 ± 16
χ^2	6 ± 1	6 ± 2

Table 4.4: Mean \pm standard deviation of pixel wise calculated results using the 2CX for PF, PV, MTT, PSAP, EF, AIC and χ^2 achieved with additional flow in the dialysate circuit in same and in counter direction.

	additional flow in same direction	additional flow in counter direction
PF (ml/100 ml/min)	58 \pm 22	51 \pm 20
PV (ml/100 ml)	25 \pm 16	39 \pm 23
MTT (s)	25 \pm 13	26 \pm 19
PSAP (ml/100 ml/min)	12 \pm 9	9 \pm 8
EF (%)	19 \pm 17	17 \pm 12
AIC	127 \pm 10	149 \pm 13
χ^2	7 \pm 3	4 \pm 2

Table 4.5: Mean values \pm standard deviations for σ_{intra} , χ^2_{intra} and PF_{inter} dependent on PAT and sampling rate.

PAT / T_s (s)	1 / 3.8	2 / 2.7	3 / 2.3	4 / 2.1	5 / 2.0	6 / 1.9
σ_{intra} (ml/100 ml/min)	25.8 \pm 0.7	26.4 \pm 1.2	26.8 \pm 1.3	24.2 \pm 4.7	20.4 \pm 1.5	19.8 \pm 1.6
χ^2_{intra}	6.4 \pm 0.2	5.7 \pm 0.1	5.1 \pm 0.1	5.1 \pm 0.2	5.4 \pm 0.1	5.4 \pm 0.1
$\text{PF}_{\text{inter}} \pm \sigma_{\text{inter}}$ (ml/100 ml/min)	77.0 \pm 2.7	78.2 \pm 4.1	75.0 \pm 4.9	83.4 \pm 8.2	84.0 \pm 4.4	80.2 \pm 4.3

4.2.4 Temporal Resolution and PAT

The AIF and pixel wise calculated maps for PF for different temporal resolutions by variation of the PAT factor are shown in [Figure 4.8](#). Corresponding mean values and standard deviation are given in [Table 4.5](#).

Moreover, a quantitative analysis was carried out.

(1) Intra measurement variability: For each individual measurement, σ_{intra} of the PF within the phantom and the fit quality χ^2_{intra} are depicted in the boxplot in [Figure 4.9](#) to determine the robustness and performance of the fit. The statistical evaluation showed that σ_{intra} of the PF is significantly smaller for PAT = 5 and PAT = 6 compared to the other measurements. For χ^2_{intra} the values for PAT = 1 are significantly higher.

(2) Inter measurement variability: The median and interquartile range of the mean values of PF_{inter} within the measurement series are shown in the boxplot in [Figure 4.9](#). The unpaired t-test reveals a significant lower value for PAT = 1 and PAT = 3 measurements compared to PAT = 5, an elevated median is noticeable here in the boxplot.

4.2.5 Application for ASL

The control and label images generated with the ASL sequence in an intermediate step provide homogeneous results of the phantom flushed with water. They are depicted in [Figure 4.10](#) together with the perfusion-weighted image calcu-

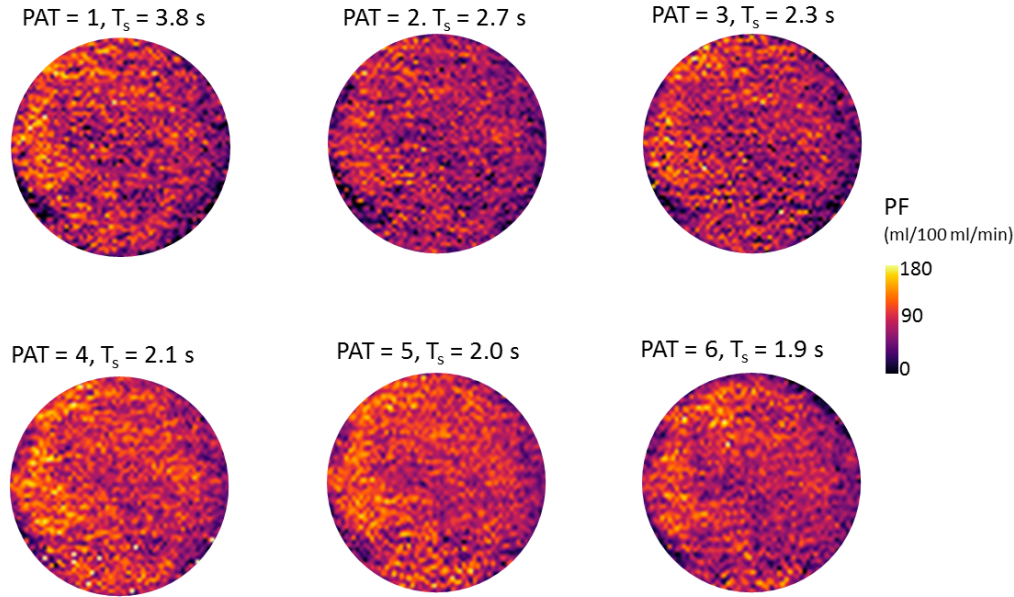


Figure 4.8: Pixel wise calculated PF maps for different temporal resolutions T_s achieved by parallel imaging (PAT). Sampling rate of the last measurement is twice as high compared to the first one.

lated from these scans. PF was determined pixel wise in a ROI in the artificial dialyzer tissue. The mean values of this measurement with $PF = (98 \pm 36)$ ml/100 ml/min agree well with the subsequently performed DCE measurement $PF = (91 \pm 26)$ ml/100 ml/min. The standard deviation is increased by 44 % for the ASL measurement compared to the DCE measurement.

4.2.6 Application for DCE CT

The measured CT signal obtained with experimental setup 1 shows a high HU signal caused by the CA locked in the fiber circuit in the phantom at $t = 0$ s. The subsequent washout by the water flow through the dialysate circuit is expressed in a decreasing signal in [Figure 4.11](#). The measured signal data points follow a typical clearance function as described in [Equation 3.2.2](#), the performed fit revealed a clearance of $K = 203$ ml/min. This is in good agreement with the result of the MRI measurement of $K = 207$ ml/min.

Evaluation of the signal of experimental setup 2 shows that the phantom generates AIFs and tissue functions with characteristic first pass - the steep increase in the signal - and typical washout slopes for all tested flow velocities ([Figure 4.12](#)). Results of the gamma variate fit are given in [Table 4.6](#). The start time τ of the AIF signal curve is delayed for lower velocities, the height of the maximum Γ_{\max} increases with higher velocities. The time of the maximum t_{\max} is reached earlier for higher velocities. The start time τ of the tissue signal curve is delayed for lower velocities and the height of the maximum Γ_{\max} is decreased for the highest velocity due to a higher baseline signal. The time of the maximum t_{\max} is reached earlier for higher velocities. The intensities of the tissue signal are reduced and the curve width is broadened compared to

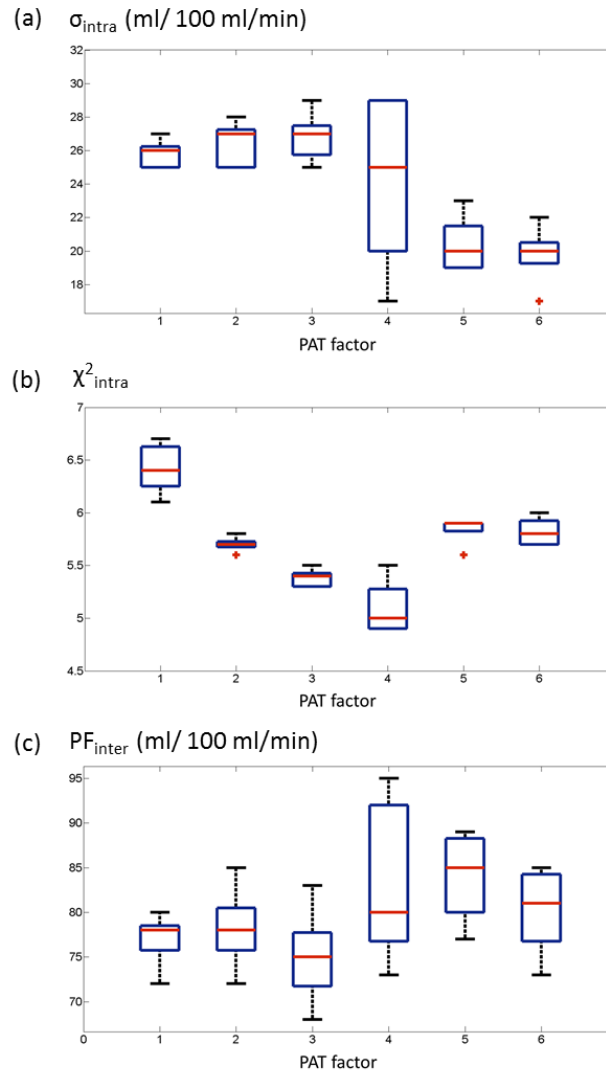


Figure 4.9: Intra measurement variability: (a) Boxplot for σ_{intra} and (b) χ^2_{intra} . Inter measurement variability: (c) Boxplot of PF_{inter} . Each plot shows PAT = (1, 2, 3, 4, 5, 6) with corresponding $T_s = (3.8, 2.7, 2.3, 2.1, 2.0, 1.9)$ s. The median is depicted by a red line, first and third quartile are shown in blue, whiskers at 1.5 times the interquartile distance in black.

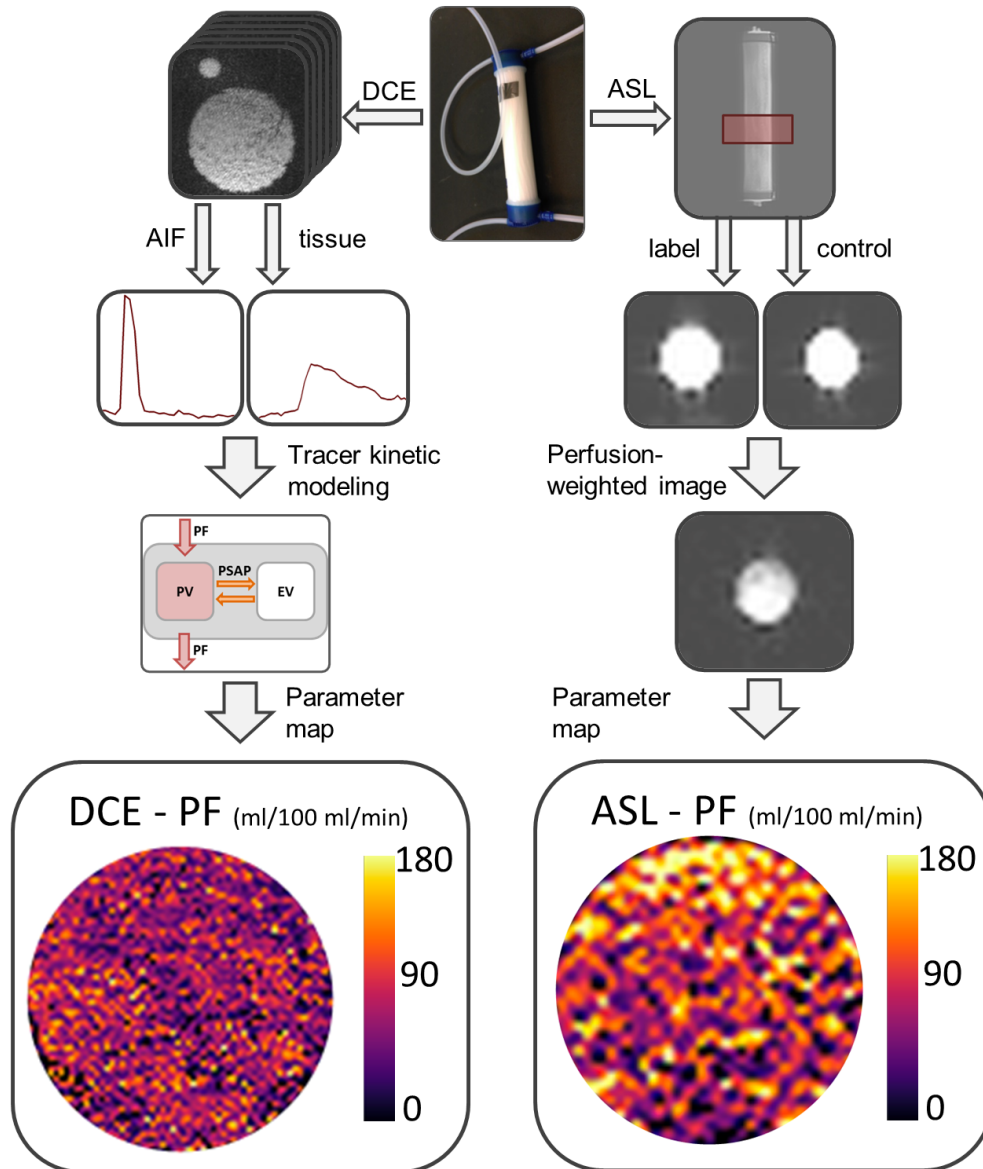


Figure 4.10: Phantom measurement using DCE MRI and ASL. DCE operating steps on the left side: AIF and tissue function are used for tracer kinetic modeling. ASL operating steps on the right side: Control and label image in the artificial tissue of the phantom are measured and perfusion weighted image is subsequently calculated by the scanner software. PF map was calculated pixel wise.

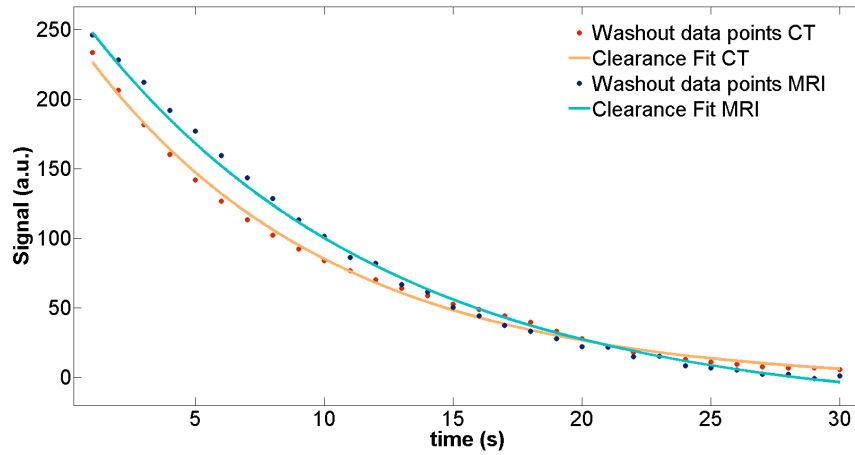


Figure 4.11: Plot of the signal decrease caused by CA transfer through a semipermeable membrane from fibers to dialysate space and subsequent washout. The data points follow a typical clearance function.

Table 4.6: Results of the gamma variate fit used for AIF and tissue data points for different flow velocities in DCE CT. The start time τ , the height of the maximum Γ_{\max} and the time of the maximum t_{\max} are given.

flow velocity	16 ml/s	18 ml/s	20 ml/s
AIF			
τ (s)	25	23	19
Γ_{\max}	282	337	339
t_{\max} (s)	27	25	21
tissue			
τ (s)	32	29	27
Γ_{\max}	46	46	43
t_{\max} (s)	36	31	29

the AIF measurements. A comparison of the curve progression of the MR and CT measurement shows differences in the start time of the AIF signal curves, MR ones are independent of the flow velocity whereas they start later for lower velocities in CT. However, the remaining characteristics of the AIF curves are the same in both modalities. The tissue curves show a delayed behavior at lower speeds in both modalities. The widening of the bolus is more prominent in the MR measurements than in the CT measurements.

PF = (94 ± 53) ml/100 ml/min was calculated applying the FD approach to the CT data, the map is given in [Figure 4.13](#). PV = (21 ± 16) ml/100 ml and MTT = (22 ± 14) s was furthermore determined.

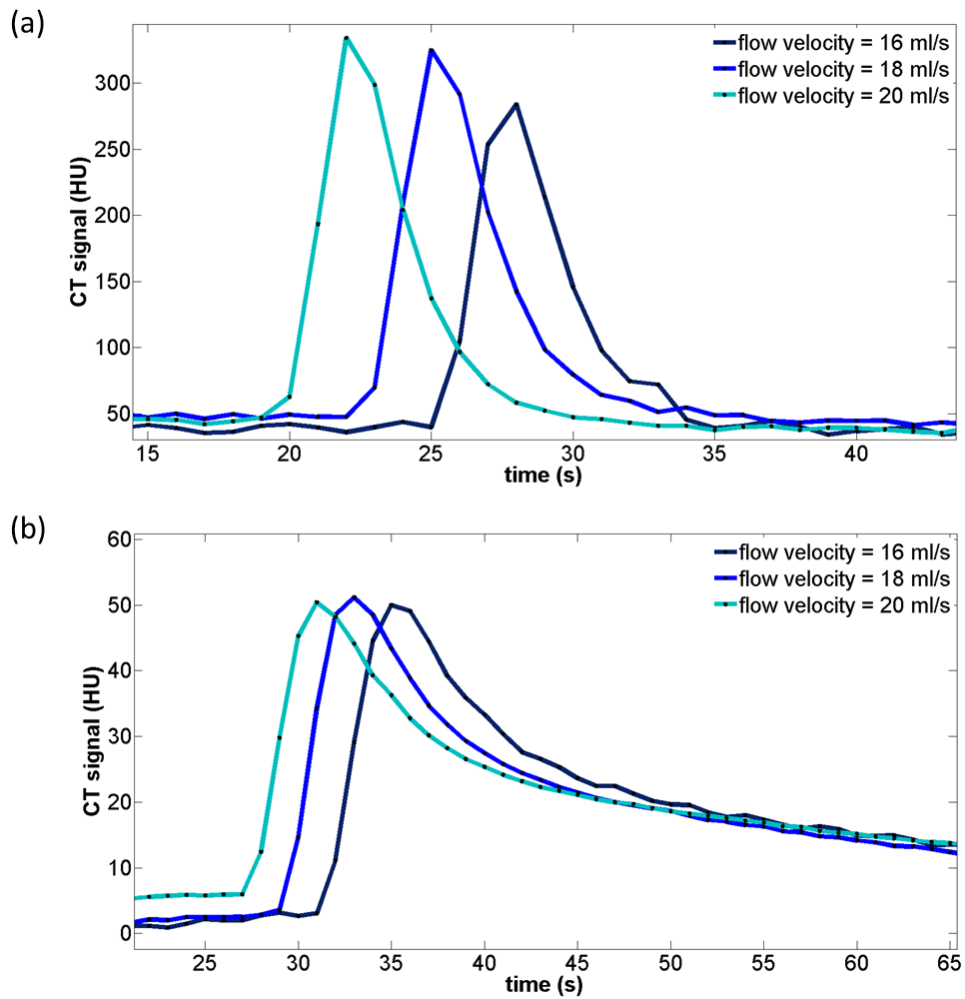


Figure 4.12: (a) Plot of the CT signal in the phantoms artificial artery over time for three different flow velocities resulting in AIFs and (b) signal in the phantoms artificial tissue region over time for three different flow velocities resulting in typical tissue functions. A delay and broader distribution can be observed for lower velocities.

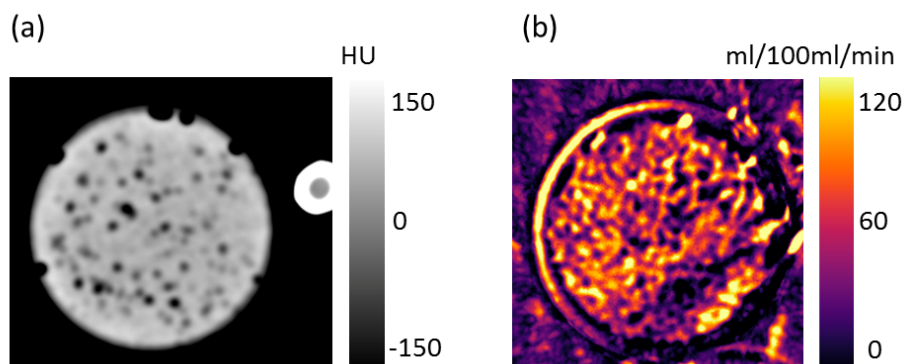


Figure 4.13: Perfusion phantom application in the CT. (a) Native measurement of phantom and artificial AIF and (b) pixel wise calculated map of PF.

4.3 DCE in vivo Study in Rectal Cancer Patients

The results of a retrospective rectal cancer study of 18 patients is presented in the following. DCE imaging of the tumor tissue with quantitative evaluation comparing CMs to FD was published in (Gaa et al., 2017). Influence of AIF application and tumor selection as well as comparison to CT results is additionally presented.

4.3.1 Bilateral Blood Supply and AIF Selection

The delineated tumor and the rectangular shaped box for pixel wise calculation of parameter maps are depicted in Figure 4.14, together with the ROIs for the AIF placed in the left and right iliac artery. Beside, their corresponding signal curves of one representative patient are shown.

The total blood supply of the arteries to the tumor and thus the signal over time differs for left and right AIF especially at the bolus peak. Perfusion parameters PF, PV, MTT and permeability parameters PSAP and EF determined with the individual AIF are given in Table 4.7 together with the fit quality calculated using AIC and χ^2 . The table shows the results separately for the use of the three evaluation methods FD, 2CU and 2CX. Summarized results for all patients are depicted in the boxplots in Figure 4.16 and Figure 4.17. Parameter maps of a representative patient are shown in Figure 4.15.

The mean values of each single parameter compared for left and right AIF all lie within the 1σ confidence interval. The maximum deviation is 22 % for the PF in the 2CX and also in general PF is the parameter with the largest deviations. Mean and median show a good agreement, although there are larger deviations in PSAP and χ^2 . It is prominent that outliers exist for almost all parameters and models.

Statistical analysis with a paired t-test revealed significant deviations for the PF for the use of left and right AIF when the compartment models are used (2CU: $P = 0.04$, 2CX: $P = 0.04$). Furthermore, the EF shows a statistically significant deviation with the 2CU ($P = 0.03$). All other parameters show no significant deviations for the two different AIFs.

The individual patient results using left and right AIF subtracted from each other are visualized in the boxplot in Figure 4.18. There are considerable deviations, especially in the PF with up to 30 ml/100 ml/min. PF obtained fitting the CM deviates significantly from zero, meaning values of the right AIF are significantly higher in the individual patient than for the left AIF. The mean and median of all parameters show no significant deviation except for PF using the 2CM. Here, the median is around zero, however the mean is systematically negative.

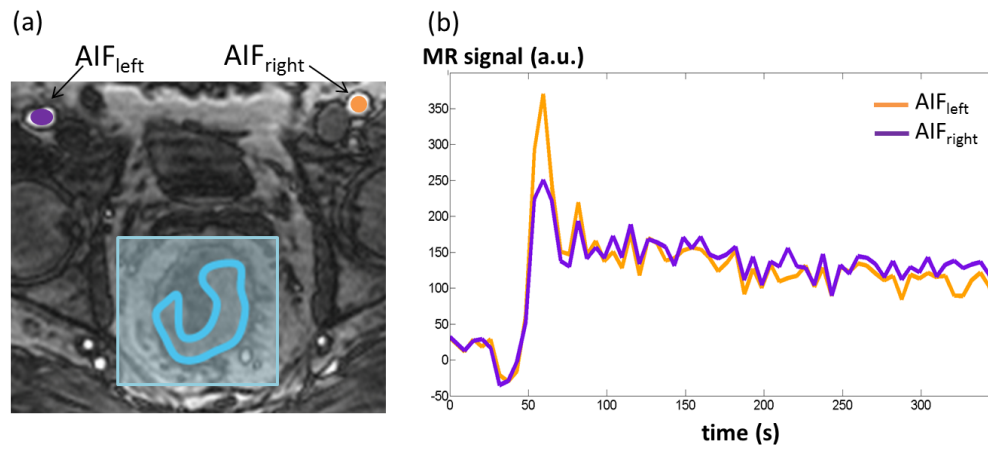


Figure 4.14: (a) Native MR image with ROIs for left (purple) and right (orange) AIF positioned in the external iliac artery. The tumor of the representative patient is delineated in blue surrounded by the rectangular shaped box used for the subsequent parameter maps. (b) Averaged signal in the AIFs. Differences especially at the bolus peak are clearly visible.

Table 4.7: Mean \pm standard deviation of perfusion parameters for left and right AIF applying FD, 2CX and 2CU.

	FD		2CX		2CU	
	AIF _{left}	AIF _{right}	AIF _{left}	AIF _{right}	AIF _{left}	AIF _{right}
PF (ml/100 ml/min)	37 \pm 21	36 \pm 19	61 \pm 38	79 \pm 61	50 \pm 33	64 \pm 44
PV (ml/100 ml)	32 \pm 18	31 \pm 15	16 \pm 9	18 \pm 12	21 \pm 11	22 \pm 13
MTT (s)	58 \pm 15	58 \pm 17	17 \pm 9	15 \pm 11	28 \pm 15	25 \pm 15
PSAP (ml/100 ml/min)	-	-	8 \pm 7	9 \pm 8	2 \pm 2	2 \pm 2
EF (%)	-	-	11 \pm 7	9 \pm 6	5 \pm 4	4 \pm 3
AIC	-	-	165 \pm 82	174 \pm 85	180 \pm 75	184 \pm 80
χ^2	-	-	9 \pm 11	11 \pm 14	8 \pm 9	10 \pm 12

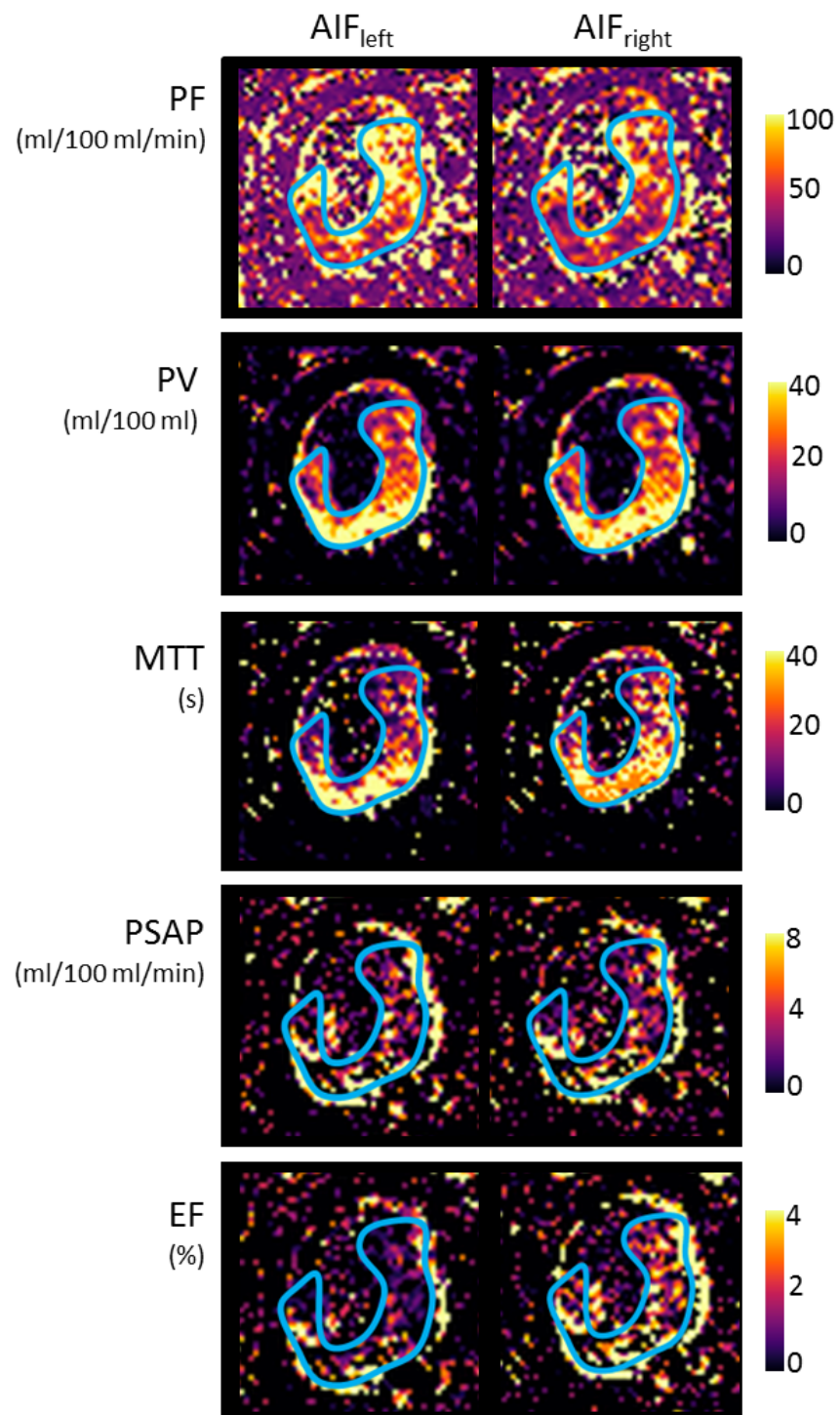


Figure 4.15: Parameter maps of PF, PV, MTT, PSAP and EF generated with the 2CU in one representative patient using left and right AIF. The tumor is delineated in blue.

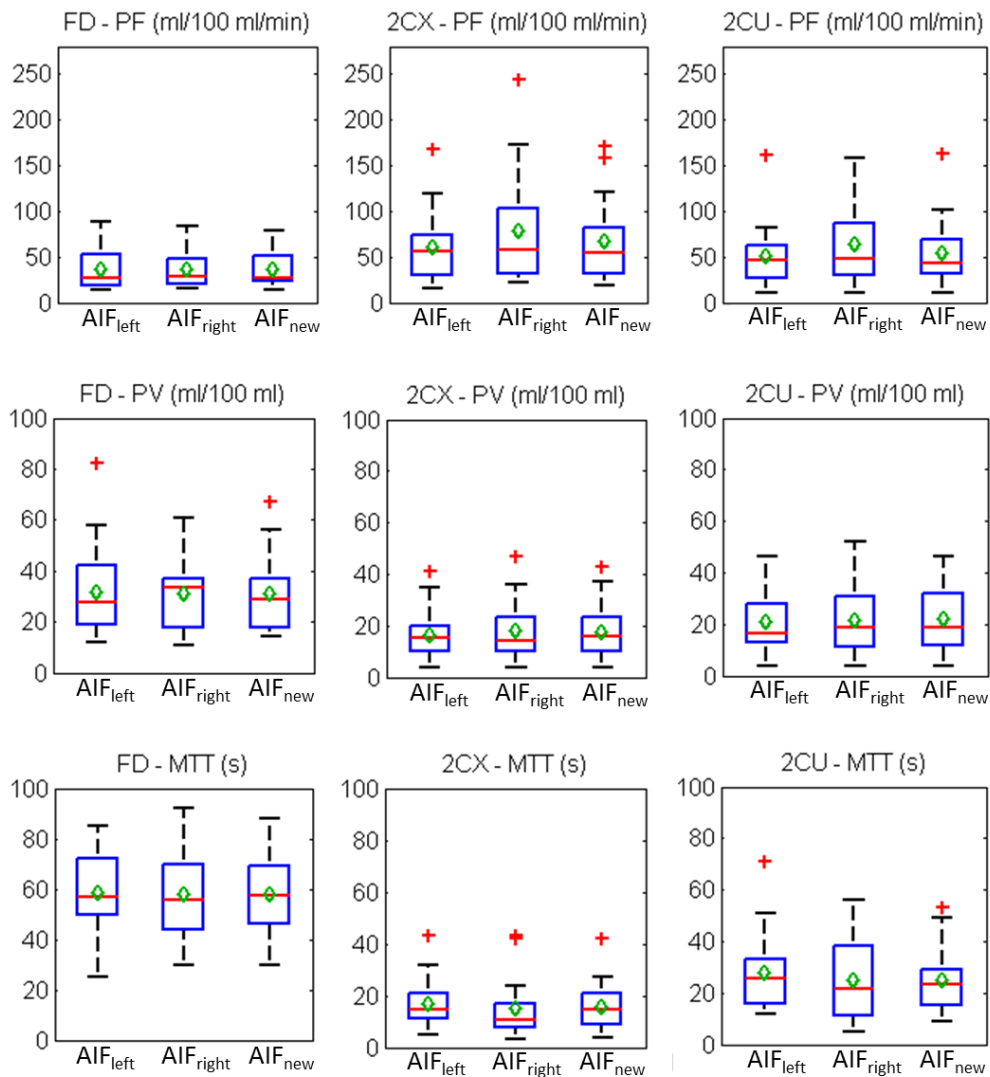


Figure 4.16: Boxplots visualizing PF, PV and MTT for FD, 2CU and 2CX. The values are calculated for the left, right and new combined AIF. The median is depicted by a red line and the mean values by a green dot. First and third quartile are shown in blue, whiskers at 1.5 times the interquartile distance in black.

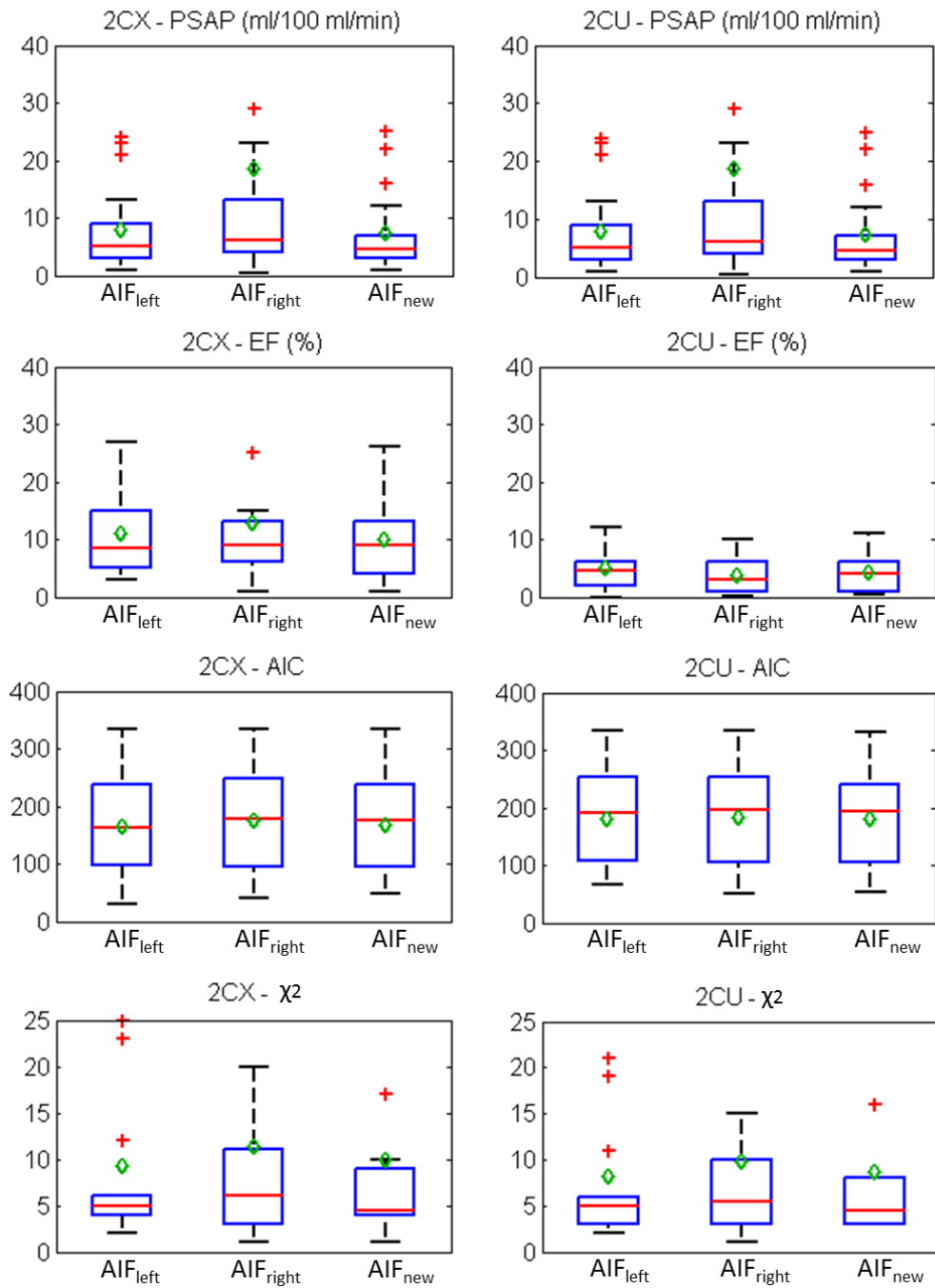


Figure 4.17: Boxplots visualizing PSAP, EF, AIC and χ^2 for 2CU and 2CX. The values are calculated for the left, right and new combined AIF. The median is depicted by a red line and the mean values by a green dot. First and third quartile are shown in blue, whiskers at 1.5 times the interquartile distance in black.

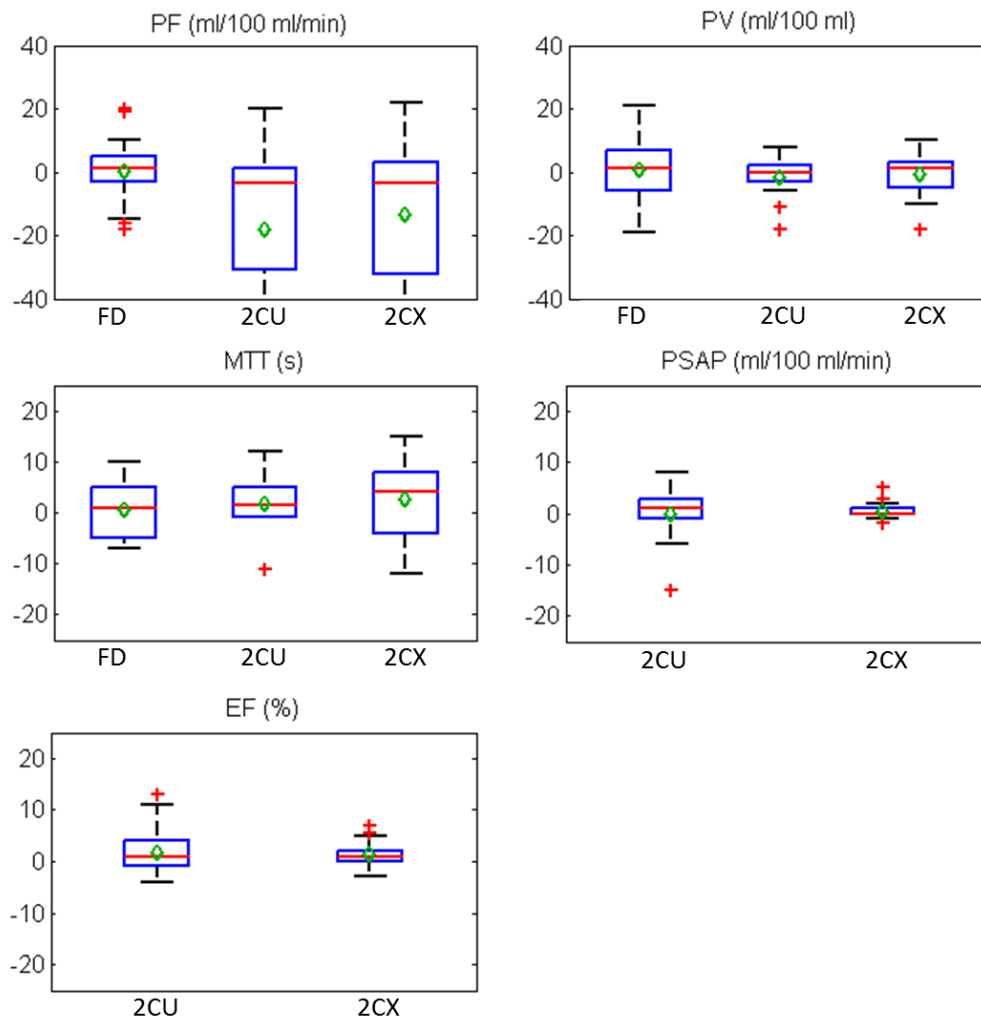


Figure 4.18: Boxplots visualizing the differences of PF_{l-r} , PV_{l-r} , MTT_{l-r} , $PSAP_{l-r}$ and EF_{l-r} for all patients for left and right AIF using the FD, 2CX and 2CU. The median is depicted by a red line and the mean values by a green dot. First and third quartile are shown in blue, whiskers at 1.5 times the interquartile distance in black.

4.3.2 Compartment Models and Model Free Approach

Figure 4.19 depicts the tissue signal and fit curves for the 2CU and 2CX model and the tumor signal of one representative patient. Maps of PF, PV and MTT for one representative patient are shown for the 2CU and 2CX model and the FD approach in Figure 4.20.

Mean values and standard deviations for estimated perfusion parameters PF, PV, MTT, the permeability parameters PSAP, EF and fit quality determined with AIC and χ^2 averaged over all 18 patients are given in Table 4.8.

Both the 2CU and the 2CX show similar results for the mean values and all lie within the 1σ confidence interval. However, slight differences in the fit lead to higher values for PF (19 %) for the 2CX whereas the mean values for the

2CU are higher for PV (18 %) and MTT (36 %). The FD results show large deviations to those calculated with the 2CM with the MTT being three times as high for the FD compared to the 2CX. Compared to the compartment models (2CX/2CU), an underestimation of the PF (47 %/35 %) and an overestimation of MTT (72 %/57 %) and PV (41 %/29 %) can be observed for the FD approach.

This is also visualized in the Bland-Altman plots in [Figure 4.21](#). In all plots, almost all data points are distributed within the band of agreement placed at ± 1.96 standard deviations. A maximum of two outliers outside the band of agreement can be observed. Differences between two measures and corresponding standard deviations calculated of the FD approach and one of the 2CM are higher than the comparison of the CMs among each other.

The results separated by different cancer stages T2, T3 and T4 also given in [Table 4.8](#) all lie within the 1σ confidence interval for the FD approach when compared to the initial results. Deviations for the FD range between (0 - 33) %, highest deviations can be found for T4 cancer stage. A higher dependency on the tumor stage can be found for the CMs, here deviations range between (10 - 68) % for the 2CX and (12 - 66) % for the 2CU. For both models, values for MTT lie outside the 1σ confidence interval. Also, deviations are most prominent for T4, but also T2 cancer stage. The trend for all parameters and models is the same, for example for T3 all approaches show a higher PF.

Mean perfusion parameters PF, PV, MTT for healthy rectum tissue were all smaller compared to the tumor tissue for FD and 2CU. For 2CX, PF and PV are smaller, MTT is constant. The trends of higher PF and smaller PV and MTT for the CMs compared to the FD already described for tumor tissue remains consistent also for the healthy tissue.

Permeability parameters show large deviations; the results for both parameters are about 2.5 times higher for the 2CX compared to the 2CU. The large standard deviation leads to values lying within the 1σ confidence interval. Parameters of the fit quality were calculated for both compartment models. These differed by 5 % regarding AIC and 10 % regarding χ^2 .

For comparison, the results were also included in the boxplots from [subsection 4.3.1](#) in [Figure 4.16](#) and [Figure 4.17](#). AIF_{new} shows the result of the new, combined AIF. The combination of both sides leads to a mitigation of extreme outliers which are no longer as strongly weighted by the new approach.

Statistical analysis with the non parametric paired Wilcoxon sign rank test showed significant differences for the comparison of all models. The P-values were smaller than 0.01 for all compared models and perfusion parameters. Parameters for fit quality also showed significant differences, however with higher P values of 0.02 (AIC) and 0.04 (χ^2) ([Table 4.9](#)).

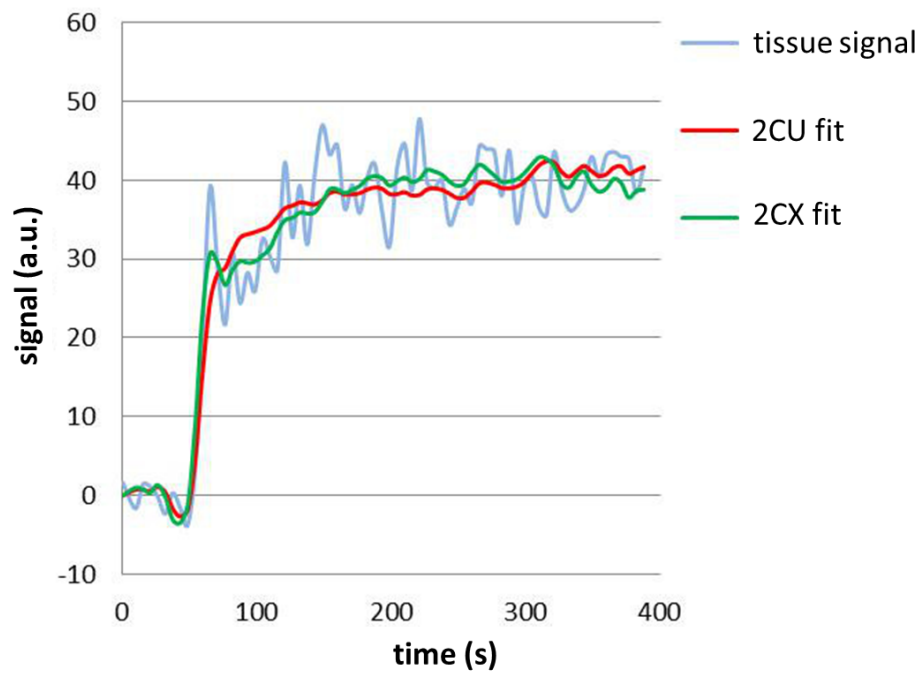


Figure 4.19: Signal in the tumor tissue over time in blue and fit curve calculated with 2CU (red) and 2CX (green).

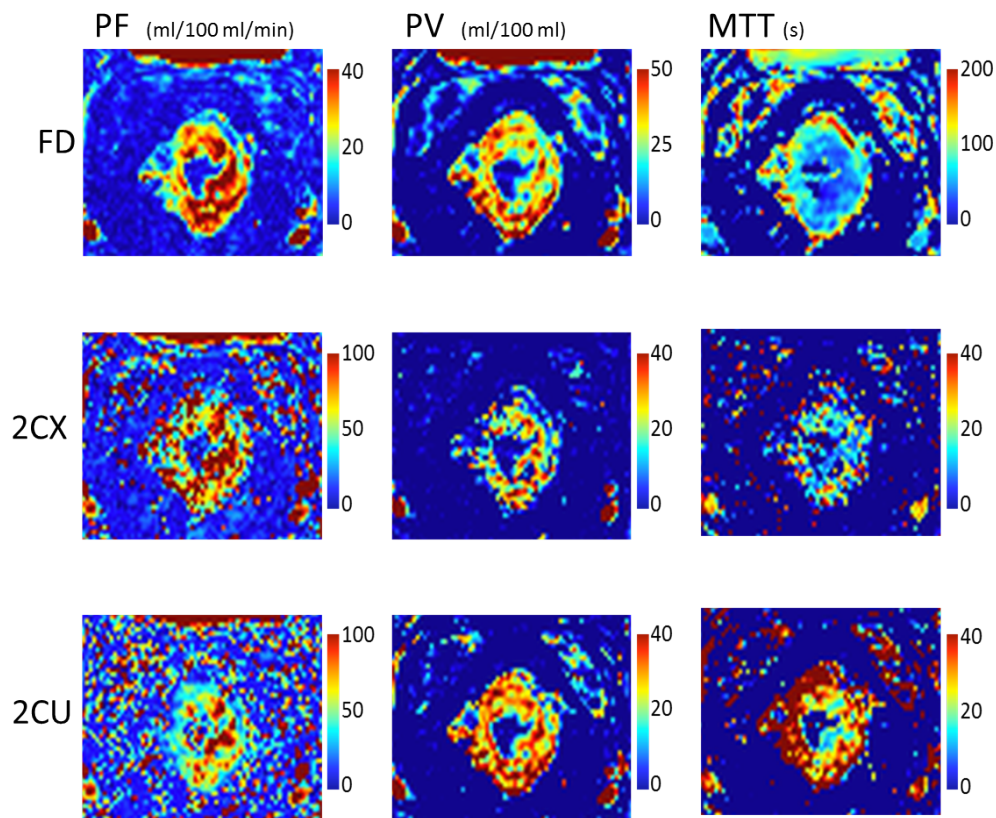


Figure 4.20: Pixel wise calculated maps for PF, PV and MTT of the tumor region of one representative patient for the 2CU and 2CX compared to the FD approach.

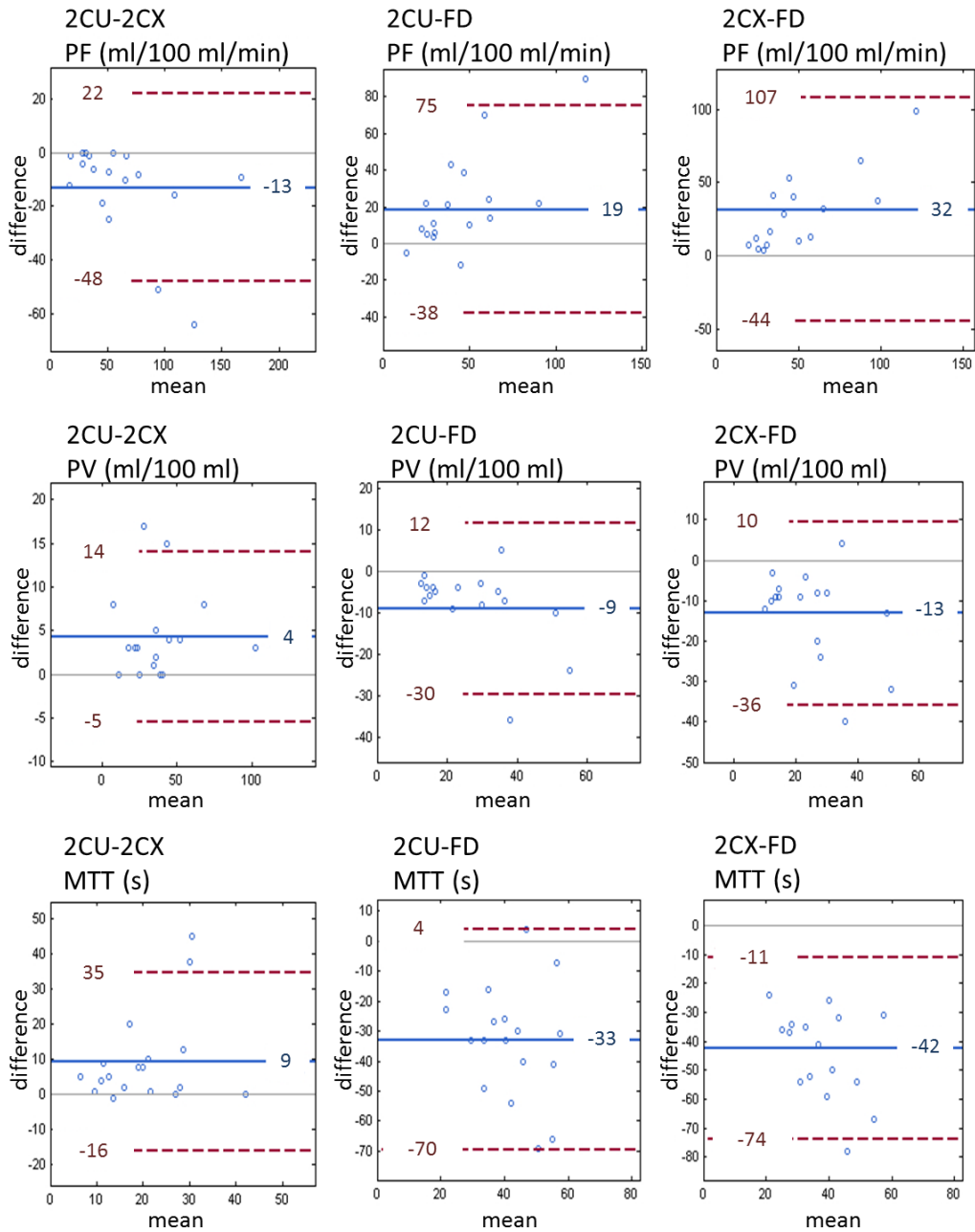


Figure 4.21: Bland-Altman plots of the perfusion parameters PF, PV and MTT from top row to bottom row comparing the applied approaches FD, 2CU, 2CX among each other from left to right. The mean value of the difference between two measures over the mean of two measures is depicted in blue. The band of agreement (placed at ± 1.96 standard deviations) is depicted in red.

Table 4.8: Overview of perfusion, permeability and quality of fit parameters stated in mean \pm standard deviation for the 2CX, 2CU and FD. Values for healthy rectum wall are given in *italic*. Separate values for the different cancer stages are listed. Note that permeability parameters can not be calculated with the FD approach. Quality of fit parameters are not depicted for the FD approach as values are calculated directly with this approach and no fit is required.

Parameter	2CX	2CU	FD
Mean of tumor tissue (<i>and healthy tissue</i>)			
PF (ml/100 ml/min)	68 \pm 44 <i>37 \pm 19</i>	55 \pm 36 <i>34 \pm 16</i>	36 \pm 19 <i>27 \pm 11</i>
PV (ml/100 ml)	18 \pm 11 <i>11 \pm 4</i>	22 \pm 12 <i>11 \pm 5</i>	31 \pm 15 <i>19 \pm 7</i>
MTT (s)	16 \pm 9 <i>16 \pm 5</i>	25 \pm 13 <i>20 \pm 6</i>	58 \pm 16 <i>46 \pm 16</i>
PSAP (ml/100 ml/min)	7 \pm 7	2 \pm 2	-
EF (%)	10 \pm 7	4 \pm 3	-
AIC	169 \pm 81	179 \pm 77	-
χ^2	10 \pm 12	9 \pm 10	-
T2 (3 patients)			
PF (ml/100 ml/min)	41 \pm 16	33 \pm 5	34 \pm 12
PV (ml/100 ml)	25 \pm 9	31 \pm 7	33 \pm 6
MTT (s)	25 \pm 13	38 \pm 11	67 \pm 18
T3 (13 patients)			
PF (ml/100 ml/min)	76 \pm 47	61 \pm 38	37 \pm 21
PV (ml/100 ml)	16 \pm 11	20 \pm 12	31 \pm 17
MTT (s)	13 \pm 6	22 \pm 11	55 \pm 15
T4 (1 patient)			
PF (ml/100 ml/min)	34	33	27
PV (ml/100 ml)	17	17	26
MTT (s)	27	29	59

Table 4.9: Statistical determination of pairwise test between the applied evaluation approaches FD, 2CU and 2CX. P-values obtained with Wilcoxon sign rank test are given for perfusion parameters PF, PV and MTT and for AIC and χ^2 . $P < 0.05$ was considered as significantly different.

	FD - 2CX	FD - 2CU	2CX - 2CU
P (PF)	0.0012	0.0079	6.13 E-05
P (PV)	3.51 E-04	7.27 E-04	2.44 E-04
P (MTT)	1.96 E-04	2.32 E-04	6.34 E-04
P (AIC)	-	-	0.02
P (χ^2)	-	-	0.04

4.3.3 2D and 3D Evaluation

The mean tumor size \pm standard deviation of the single slices for the subgroup of five patients was (5 ± 2) cm², the mean overall tumor volume \pm standard deviation was (7 ± 2) cm³ with a slice thickness of 3.6 mm. Visualization of perfusion parameters PF, PV and MTT for all slices and all patients are presented in [Figure 4.22](#). The figure includes values of the single slice delineated by the performing physician and mean values with standard deviation for the combined surrounding slices. The corresponding values are given in [Table 4.10](#) and parameter maps of the PF in five slices in a representative patient can be seen in [Figure 4.23](#).

Data analysis showed that mean values of the single slice deviate up to 12 % for PF, 14 % for PV, and 7 % for MTT. Values for two of the slices chosen by the performing physician and in total values of 13 slices are lying outside the 1σ confidence interval of the perfusion parameters acquired over the whole volume. Maximum deviations between two single slices in a tumor volume range up to 28 % for PF and PV and 36 % for MTT.

4.3.4 Comparison DCE CT

The results of the volume perfusion CT are given in [Table 4.11](#). They show mean values and standard deviations for PF, PV and MTT determined with the FD approach. Compared to the calculated MR values in [Table 4.8](#), the PF shows good agreement with a deviation of 19 % lying within the 1σ confidence interval. PV and MTT however show more than 10 times higher values in the MRI results compared to the CT results. Values of the healthy tissue show the same trends, the PF and PV decreases whereas the MTT stays constant, however, also here the MRI results are multiple times higher compared to the CT results.

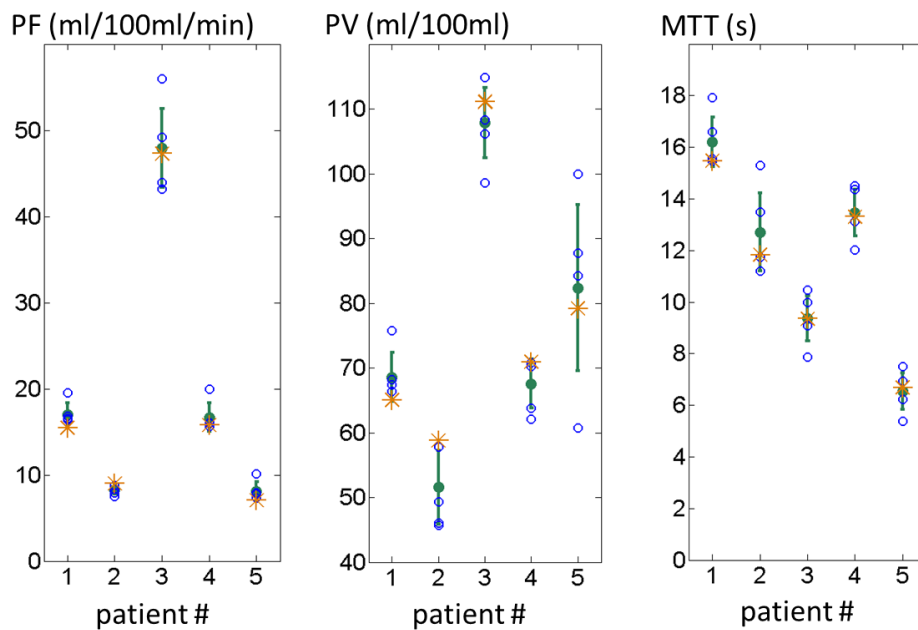


Figure 4.22: Graph of the perfusion parameters PF, PV and MTT calculated for individual 2D slices and 3D volume of rectum tumor tissue. The value of the chosen slice of the performing physician is marked in yellow, the additional ones in blue. The mean value \pm standard deviation of all five slices is given in green.

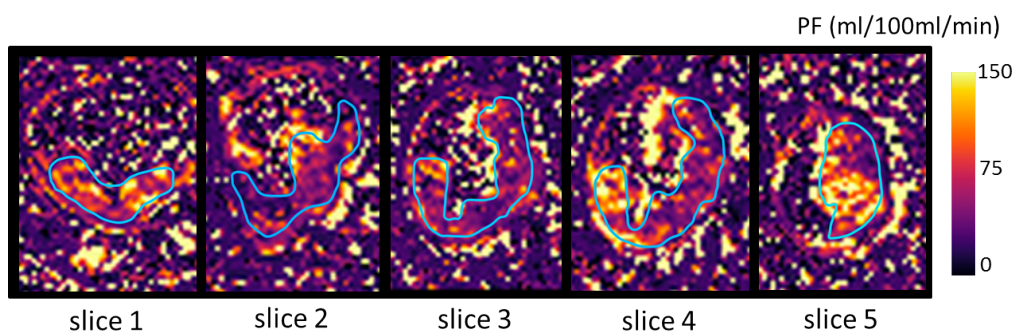


Figure 4.23: PF parameter maps of five subsequent slices of rectum tumor tissue in a representative patient. PF values are heterogeneous within one slice and when compared between the five individual slices.

Table 4.10: Mean values of pixel wise calculated parameter maps for PF, PV and MTT for each single slice and calculated mean value \pm standard deviation for the entire tumor volume. The value for the slice chosen by the performing physician is given in **bold**.

	patient #	slice 1	slice 2	slice 3	slice 4	slice 5	mean \pm std
PF (ml/100 ml/min)	1	76	67	65	68	66	69 \pm 4
	2	46	49	59	58	46	52 \pm 6
	3	115	108	99	106	111	108 \pm 5
	4	62	71	64	70	71	68 \pm 4
	5	88	61	100	84	79	82 \pm 13
PV (ml/100 ml)	1	17	20	15	16	17	17 \pm 1
	2	8	8	9	9	7	8 \pm 1
	3	56	49	44	43	47	48 \pm 5
	4	16	16	16	16	20	17 \pm 5
	5	7	8	10	8	7	8 \pm 1
MTT (s)	1	15	18	15	17	16	16 \pm 1
	2	15	13	12	11	12	13 \pm 2
	3	10	9	8	10	9	9 \pm 1
	4	13	13	12	15	14	13 \pm 1
	5	5	7	7	6	7	7 \pm 1

Table 4.11: Mean values \pm standard deviation of the perfusion parameters PF, PV and MTT for the FD approach calculated on DCE CT data and compared to the DCE MRI data from [Table 4.8](#). The healthy rectum wall tissue results are given in *italic* for comparison.

	FD (CT)	FD (MR)
Mean of tumor tissue (<i>and healthy tissue</i>)		
PF (ml/100 ml/min)	43 \pm 12	36 \pm 19
	<i>15 \pm 6</i>	<i>27 \pm 11</i>
PV (ml/100 ml)	3 \pm 1	31 \pm 15
	<i>1 \pm 1</i>	<i>19 \pm 7</i>
MTT (s)	5 \pm 2	58 \pm 16
	<i>5 \pm 1</i>	<i>40 \pm 16</i>

Discussion 5

Two approaches were applied to determine feasibility, improvements and limitations in quantitative DCE perfusion MRI. A perfusion phantom setup suitable for DCE measurements was developed and a retrospective rectum cancer patient data set was analyzed. This chapter discusses the findings of these two parts of the thesis, some of which were published in ([Gaa et al., 2017](#)).

5.1 DCE Perfusion Phantom Study

Feasibility

First, the question was addressed whether the phantom meets the requirements of a model that reflects the physiology in humans with flow through the capillaries, the surrounding extravascular space and the exchange between these two compartments.

In experimental setup 1, the ability of Gd molecules to cross the semipermeable membrane of the phantom was investigated. It revealed that CA molecules can cross the fiber wall from dialysate space to fiber space. The migration of the molecules between the two regions and flushing out the CA followed a typical washout curve with exponential decay. The CA molecules can move freely between the two compartments without attaching to the membrane or remaining in the dialysate space. Thus, the semipermeable membrane of the fibers enables the simulation of two-compartment kinetics and can thus imitate capillaries and interstitium in the human body.

The aim of experimental setup 2 was to verify whether the phantom is capable of producing realistic AIF and tissue curves for different default flow velocities. The obtained parameters of the performed gamma variate fit correspond to the set flow velocity. The signal in the artificial AIF in the tube in front of the phantom starts at the same time for all velocities. Since the AIF is measured shortly after the injection point of the CA, no offset was anticipated due to the different velocities. For higher velocities the signal maximum increased and the curve width decreased which can be explained by the increased speed of the bolus and the resulting faster passage through the measurement slice. In the artificial tissue within the phantom, the signal has already dropped overall, as the CA bolus has widened due to the branching of the wide tube into the

small fiber capillary. This is also evident in the delayed onset of the tissue curves, starting much later at a slower flow velocity. The slightly increased maximum signal at lowest flow velocity compared to the higher velocities does not correspond to this theory. With a slower widened bolus one would have expected a lower signal. A possible explanation could be discontinuous flow in the phantom. This is more likely at lower speeds, as the individual pump impulses of the peristaltic pump characteristic have a greater influence here. The effect can clearly be seen in form of spikes in the signal. In the following experiments such low velocities were no longer used. Nevertheless, a low pump velocity would have been desirable, as this would have been more in line with the velocities in human arteries. The lowest artifact free velocity of 16 ml/s was chosen in the following as the signal in AIF and all other tissue curves showed no apparent turbulence, distortion or congestion while passing through the experimental setup.

In experimental setup 3, both previous approaches were combined. Additionally to the flow in the fiber circuit of the dialyzer, water was pumped through the outer dialysate circuit. The effects of this additional flow on the signal was investigated, both with the additional flow incorporated in same- and counter direction. The simultaneous flow through both compartments led to a reduction of the signal intensity in the artificial tissue by 49%. This expected result can be explained by the realized fluid and CA exchange between the two compartments. The CA extravasated in the dialysate space is washed out by the additional flow instead of accumulating there when no additional flow is applied. The flow direction has no influence on the measured signal.

Overall, the findings of the feasibility experiments show that the perfusion phantom can serve as a tissue mimicking device to measure perfusion in MRI.

Reproducibility

Next, the ability of the phantom to provide quantifiable and reproducible perfusion maps was investigated. The measurement was repeated five times during one measurement cycle and one week later, the same experiment was repeated to check if the results were reproducible over time.

The averaged five subsequent measurements showed standard deviations of the mean of 8 % for PF, 6 % for PV, 13 % for MTT. The deviations of the PSAP was highest with 18 % and the standard deviation of EF was 12 %. The maps for fit quality show some extreme outlier voxels which may be caused by single clogged pores in the membrane. They might be responsible for deviations and could especially influence permeability. Measurement errors occurring only in a single measurement could also be caused by air bubbles or turbulence of flow.

After one week, the PF showed no changes compared to the mean value obtained the week before. All other parameters show a decrease between 5 and 22 %, yet all lie within their standard deviation. It can therefore be assumed that no major impairment of the dialyzer material occurred within this week. However, it should be noted that poor rinsing of the CA can lead to permanent

deposits and clogging. Since the filter is commercially available, it should be replaced in such a case.

If an additional flow in the dialyzer circuit is applied, a decrease in PF, PV, PSAP and EF is observed. This can be explained, as the CA molecules in the dialyzer compartment are drained now instead of accumulating there. The MTT remains the same as this parameter depends highly on the phantoms characteristics and flow velocity of the bolus and shows a lower dependency on an additional flow. The fit quality calculated with χ^2 depends on the chosen model and the number of fitted parameters which remained the same. Thus, no change was expected, which could be confirmed in the experiment.

Even with the standardized phantom used in this thesis, a lot of adjustment parameters for an optimal fit still exist. For example, start or boundary settings, the sampling rate as well as the pharmacokinetic model representing the underlying physiology have to be found. The advantage is, however, that a phantom can eliminate many other aspects that would otherwise occur in humans. Every issue can be examined in an isolated experiment. For example, in this setup, an additional flow could be adjusted which lowered the AIC. This might be an indication, that with additional flow, the 2CX fits the data better. Influence of the sampling rate without further interference of artifacts caused by human physiology was investigated in the following. Artifacts in the phantom itself for example voxels that are recognizable as outliers are few. They may be caused by air inclusions or other stationary turbulence or agglutination of the capillaries. Such pixels could be excluded from the calculation of the average value in the future.

Temporal Resolution and PAT

The influence of different sampling rates on the perfusion parameters and their fit quality was investigated. The different sampling resolutions T_s were achieved by varying the PAT factor. In literature, the impact on the calculated parameters is a controversial question so far. Previous studies see a predominant quality enhancing effect with faster sampling rates, especially when pharmacokinetic models are to be applied (Aerts et al., 2011). A change in the parameter values themselves was also noted. Ginsburg et al. (2016) describe a larger influence on K_{trans} compared to the PV. However, Othman et al. (2016) could not find any influence of the sampling rate on perfusion parameters at all. In addition, Li et al. (2012) proposed SNR loss caused from parallel imaging. As a consequence, the application of PAT factors is used with caution in concern of quality loss in clinical practice.

Experiments with the perfusion phantom in this thesis found a significant influence of the PAT factors and T_s on the PF and inter and intra measurement variability. Significantly smaller intra measurement variability σ_{intra} was detected for the PF using high acceleration factors $PAT = 5$ and $PAT = 6$ and for χ_{intra}^2 the values for $PAT = 1$ are significantly higher. The higher sampling resolution in this cases will possibly compensate for the SNR loss proposed by Li et al. (2012) caused by parallel imaging. The significant differences for certain PAT

factors on PF shown in this work are in accordance with [Aerts et al. \(2011\)](#) and [Ginsburg et al. \(2016\)](#). This can be understood as the determination of PF depends mainly on the initial slope of the tissue curve. In order to adequately measure this rapid signal change, a high sampling rate is required. Other parameters such as PV are only determined in the further, slower changing progress of the curve. To determine those properly it is rather important to keep the measurement running until baseline is reached again. This issue should also be considered in the context of the measurement of AIF which plays a central role, especially in the application of pharmacokinetic models. A high temporal resolution is required to cover the rapid signal change sufficiently. The spatial resolution, on the other hand, is of less importance for the AIF measurement. To ensure this high spatial resolution in tumor tissue, however, is of utmost importance for diagnosis or therapy monitoring. Since the tissue curve progression does not show any more extreme changes, especially after the first slope, the sampling rate could be reduced and the spatial resolution increased instead. In the CT routine, studies have already been performed with higher sampling rates in the phase of AIF measurement and first pass in the tissue and lower sampling rates when the remaining tissue signal is acquired. This was initially done in order to reduce the dose ([Sudarski et al., 2018](#)). In MRI, however, it could be a possibility to combine optimal AIF sampling and high tissue spatial resolution.

Finally, it has to be noted that all sampling resolutions used in this experiment are high compared to other studies and clinical practice. The currently minimal recommended range is $T_s < 8 - 15$ s ([Aerts et al., 2011](#)). An even greater effect of the quantification quality can thus be expected with these long T_s . Based on the results of this work, it can therefore only be recommended to increase the sampling rate for DCE perfusion measurements, especially in the first section of the acquisition. Especially when using pharmacokinetic models, this could lead to a more reliable quantification of perfusion parameters.

Application for ASL

The feasibility of the phantom for perfusion measurements using ASL and a comparison to the results obtained with DCE measurements was evaluated. DCE models use numerous fixed parameters such as the HCT, relaxivity of the CA and flip angle. They are affected by errors in their estimation which in turn have a large influence especially on PF results ([Tofts et al., 2012](#)). But [Parkes and Tofts \(2002\)](#) showed that also ASL is strongly dependent on the chosen values for its model parameters as well. [Cutajar et al. \(2014\)](#) even asks if both approaches can be compared at all having such different underlying kinetic models and different intrinsic ways to measure perfusion. While ASL covers short temporal windows, DCE acquisition lasts for several minutes. A very simple phantom setup as proposed in this work could help to investigate the comparability of those two methods more closely.

It could be shown that the phantom is suitable for ASL measurements, producing homogeneous PF maps. The results of the ASL measurement of (98 ± 36) ml/100 ml/min are in good agreement with the DCE results of (91 ± 26) ml/100 ml/min. Although, it needs mentioning that higher blood flow and a

relatively low SNR will make the transition from phantom to patient approach likely to be more complicated. This is one of the reasons why ASL has not yet found broad clinical application. Now, for the development of a standardized workflow, the two independent measurement methods can be compared. This offers great potential in perfusion measurement and strengthens the importance of both DCE and ASL. Balancing patients' needs such as CA incompatibility and diagnostic needs such as high resolution could thus easier be achieved.

Application for DCE CT

Due to radiation exposure during a CT scan, phantoms are important to develop, investigate, and evaluate new perfusion imaging techniques. The feasibility of the phantom for DCE CT measurements could be shown. Washout of iodine based CA is similar to the one obtained by Gd in the MRI measurement, its higher viscosity did not influence this process. This could be demonstrated by a good agreement in the clearance fit parameter of $K_{CT} = 203$ ml/min and $K_{MRI} = 207$ ml/min. AIF and tissue functions could be obtained and gamma variate fits revealed comparable results to those achieved in the MRI measurement. The delayed start in the AIF may be caused by a larger distance of CA injection point and position of AIF measurement caused by a slightly changed experimental setup in the scanner room. Another explanation could be the higher viscosity of the CT CA leading to a changed fluid dynamic of the bolus. $PF = (94 \pm 53)$ ml/100 ml/min obtained with the FD approach is in good agreement with the MRI results ($PF = (91 \pm 26)$ ml/100 ml/min). The higher standard deviation might be due to image artifacts caused by the tube with a high concentration of CA next to the phantom which should be changed in the phantom setup in future measurements. MTT as well shows a good agreement whereas PV is reduced. The application of the alternative quantification approach could be the reason for this and remains further research.

Limitations - DCE Perfusion Phantom Study

One limitation of the phantom is the orientation of the fibers in a preference direction. Physiologically, capillaries are branched in arbitrary directions. This has an effect on the measured total signal in a slice which cannot be reflected by the dialyzer phantom. [Gaass et al. \(2017\)](#) developed a phantom providing a solution for this, however, it is not reproducible in its production and compartments can not be modeled. The development of ever more precise and refined 3D printing methods may be a conceivable solution to combine both the reproducible and branched capillary approaches in the future.

The use of water as a transport medium for the CA ensured optimal repeatability and control of the experimental conditions. However, it is expected that the flow dynamics in the in vivo capillaries will be more complex than in our experiments as a result of the pulsating flow in the arterial vessels and the non-Newtonian behavior of the blood. In other studies, flow dynamics have already been simulated with a water glycerol mixture, which is closer to the composition of blood ([Foltz et al., 2019](#)). Yet, this is more cost-intensive and the behavior within capillary-sized fibers in phantoms would have to be examined first.

5.2 DCE in Vivo Study in Rectal Cancer Patients

Bilateral Blood Supply and AIF selection

It is essential to determine a reliable AIF for the quantification of perfusion as completely different physiological processes can lead to the same tissue signal. Calamante (2013) describes an example of a narrow bolus, which reaches the tissue very quickly but leaves it slowly and with a long MTT due to a hypoperfusion of the tissue. The study compares this with a slow and wide bolus that leaves the tissue quickly and with a shortened MTT due to hyperperfusion. Both scenarios would provide similar tissue curves and thus perfusion parameters although the tissue condition has completely different physiological pathologies. This finding is in contrast to the clinical practice. Mostly, qualitative or semi-quantitative evaluation of the tissue curve is done. If sometimes quantification with a pharmacokinetic model is performed, an AIF in one slice and on one side of the body is arbitrarily selected only. To examine this topic in more detail, the effects on the perfusion parameters were investigated in rectal cancer patients. Either the left or right supplying artery was used as AIF and the influence when using a model free FD approach and two dual CM were compared.

Differences in the signal obtained with left and right AIF were observed. Significant deviations for some of the resulting perfusion parameters were found for the 2CX and 2CU, but not for the FD approach. A closer look at the individual patients revealed heterogeneous results among them. Some of the patients show little or no dependence on the selected side of the AIF, others show large inconsistencies with deviations in the PF of up to 30 ml/100ml/min. These findings are in agreement with studies of the influence of the AIF selection of quantification in DCE MRI in other organs (Cutajar et al., 2010).

An explanation could be of a physiological nature. After the bolus is injected into a peripheral vein, it passes through the heart and lungs before being distributed in the tissue. Along the entire way, the bolus may be altered in different ways on either side of the body. If bolus delays occur, the temporal offset between AIF and tissue function no longer displays the reality. Furthermore, the bolus can be broadened by diffusion, an effect called dispersion. Since the studied patients are severely ill or elderly people, abnormal changes in the arteries due to stenosis or occlusions are not uncommon and can alter the bolus even further (Michaely et al., 2006). Several correction methods have been proposed for these problems (Calamante et al., 2000). However, most of them are elaborate to implement and time consuming to use. This makes them less applicable in clinical practice. A more feasible solution is to choose the artery as close as possible to the tissue. However, these arteries are already divided into several branches and are small in diameter. Partial volume effects can therefore occur in the selected ROI. These can lead to considerable changes in the AIF in both peak width and height (Calamante, 2005).

As a first compromise that is easily implemented in clinical practice, both the left and the right artery were examined as close as possible to the tumor. The two results were averaged and the resulting AIF applied to obtain quantitative perfusion results. In this way larger deviations due to the above mentioned conditions could be attenuated.

Compartment Models and Model Free Approach

Several studies showed that the determination of perfusion parameters can serve as an additional tool for diagnosing and staging pathological changes of organs and subsequently finding an appropriate therapy method ([Attenberger et al., 2014](#); [Ceelen et al., 2006](#)). A variety of models for the calculation of these parameters is available but there is no consensus which model represents the parameters best. Thus, it is important to use the most accurate model for determination of robust functional parameters to help establish their additional value for diagnostic imaging. In this study, we investigated three different tracer kinetic approaches, the model-free FD approach, the 2CU and the 2CX model, and their impact on the quantitative perfusion parameters for rectal cancer. The use of pharmacokinetic modeling on DCE MRI data from rectal cancer patients is in contrast to previous studies that mainly dealt with the FD approach ([Attenberger et al., 2014](#)) or the Tofts model ([Tong et al., 2015](#)).

Mean values of the calculated quantitative perfusion parameters (PF, PV, MTT) show that they depend on the specific evaluation approach and are influenced by the tracer kinetic model. Perfusion values in patients differ more between the deconvolution and compartment models than among the compartment models which could be visualized in the Bland Altman plots. These results are in accordance with findings by [Sourbron and Buckley \(2011\)](#), where an underestimation of MTT and PV is described for the model-free analysis. This underestimation can occur due to long interstitial transit times of extravascular tracers. It is associated with an underestimation of the area under the impulse response function caused by too short acquisition times. They also reported a possible underestimation of PV for the extended Tofts model, whereas this effect does not occur for the compartment models ([Sourbron and Buckley, 2013](#)). This could be an argument for the use of the 2CM as opposed to the Tofts model. As the 2CU is a simplification of the 2CX for specific physiological cases, both models should yield similar results in these cases, whereas outliers would occur only if one of the model includes effects that the other model does not consider and thus fits the patient's perfusion data better. This is supported by the fact that, on the one hand, more outliers are detected for the comparison of the dual compartment models. On the other hand, standard deviation is smaller in contrast to the comparison with the FD approach. Permeability parameters are significant higher for the 2CU compared to the 2CX. These are the parameters that describe the exchange characteristic between the two compartments, which is expected to be different in the 2CU than in the 2CX. The results may therefore indicate that one of the models better describes the true physical condition. However, due to the small patient number and the lack of a gold standard measurement, further conclusions are difficult to draw. The

significant differences of the AIC and χ^2 values as a measure of the goodness of fit may be described by a few single outliers, as mean values show similar results. Most patients were grouped in T3 cancer stage. Thus, too few patients in cancer stages T2 and T4 were available to draw any conclusion on whether the stage correlates with the mean perfusion parameters. Yet, this hypothesis shall be investigated in future clinical studies.

A comparison with previously published papers investigating DCE MRI of rectal cancer is challenging as a majority of studies used only the Tofts model for evaluation, which does not enable the quantification of the perfusion parameters examined here (Ceelen et al., 2006; Tong et al., 2015). The 2CM considered here have not been employed for the calculation of perfusion parameters in rectum cancer MR images before. However, studies using CT perfusion data show blood flow values between 60 and 110 ml/100ml/min which corresponds to a PF of 33 and 60.5 ml/100ml/min, respectively, and is thus in a good agreement with the values we obtained in our study (Goh et al., 2008; Sahani et al., 2005). Calculated perfusion values for healthy rectum tissue showed higher PF and PV for all models which is also in good agreement with Sahani et al. (2005). However, due to the small size of the healthy rectum wall, only data of 10 patients was evaluated and the amount of pixels used was quite small. This could be an explanation why we measured longer (FD/2CU) or constant (2CX) MTT whereas in Sahani et al. (2005) it is reported to be shorter. Since the goodness of fit and perfusion parameters show reasonable results, it can be assumed that the dual compartment models used are generally suitable for the quantification of perfusion in rectal cancer. The choice of the optimal model depends on several aspects, for instance, if only the perfusion has to be determined or if further information such as permeability and interstitial volume are to be studied. In Donaldson et al. (2010) guidelines on selecting a tracer kinetic model are given. These guidelines state out that in some cases the 2CX and 2CU model provide advantages compared to the commonly used models. First of all, additional parameters can be useful for clinicians to describe the tumor and help to decide which therapy to use. Especially for antivascular drugs and a pre- and post-treatment observation, the FD approach cannot give any information as it does not describe two compartments and the parameter K_{trans} of the Tofts model is not as specific as PF and PSAP in the 2CX model. Furthermore, the Tofts model assumes that the time taken for the CA to pass through the plasma compartment (plasma MTT) is negligible. However, calculated MTTs show, that this cannot be assumed and signalize that the 2CX or 2CU model could describe the data better. Imaging quality is sufficient to use a more complex model than model free FD approach, which is probably more robust for images with poor data quality but does not describe the physiology properly (Luybaert et al., 2011; Sourbron and Buckley, 2011).

We found significant differences between all three approaches. This indicates that there is not only one appropriate model for the complete patient cohort, but some models seem to fit better to some specific patients. An investigation on whether a specific tumor condition or stage is decisive for the choice of the model sounds promising. However, the investigated patient cohort is limited with 18 patients. A larger number of experimental studies to show repro-

ducibility and validity of the parameter values would be necessary for a general statement on clinical usefulness and whether one model should be prioritized over the other. Whether general statements can be made for one type of tumor or if the best possible model can also differ from patient to patient remains questionable. The work of [Romain et al. \(2017\)](#), which proposes a framework for model estimation based on physiology, imaging quality and further parameters, seems promising. Nonetheless, the potential of other, physiologically also appropriate models compared to the widely used ones and the strong dependency of quantitative perfusion parameters on the chosen model could be shown here.

2D and 3D Evaluation

This study demonstrates that perfusion parameters obtained only in a single slice selected by physicians in clinical routine may differ greatly from the mean values derived in a whole tumor volume. The difference between minimum and maximum values within a volume is even more severe with up to 28% for PF and PV and 36% for MTT. The study was limited to only five of the 18 patients because the image quality of the remaining ones was not sufficient for a volume evaluation. Therefore the meaningfulness of the results can be transferred to all patients only to a limited extent. However, the findings are in accordance with other studies of [Davenport et al. \(2013\)](#); [Goh et al. \(2008\)](#); [Mendichovszky et al. \(2009\)](#) that have not investigated different slices, but determined the influence of the size of AIF and tissue ROI. [Goh et al. \(2008\)](#) compared tissue ROIs in rectal CT images with respect to their size. The study concluded that there is a huge influence on the perfusion values. It was pointed out, that especially on the edges, the homogeneity of the tumor perfusion is not given anymore. [Davenport et al. \(2013\)](#) observed in a study of simulated data that inter reader reproducibility was highest, when the largest possible ROI in one tissue slice is chosen. [Mendichovszky et al. \(2009\)](#) observed the ROI size of AIFs in kidney DCE MRI highly influences the perfusion parameters. Taken all these findings and the results obtained in this thesis together, the selection of ROIs in both AIF and tissue plays a major role in perfusion quantification. There are two main influences: First, the acquired signal contains partial volume or inflow artifacts. Due to poor selection of the AIF, the artifact can distort the signal in the ROI leading to incorrect results. Second, the signal in the respective ROI is different for anatomical or physiological reasons. The latter one advises that due to the heterogeneous morphology of most tumors, the evaluation of perfusion parameters of the entire tumor for analysis seems mandatory to determine different degrees of tumor vascularity, necrosis or hemorrhage. Although there are also other proposed correction methods, such as the omission of the tumor margin, the practical implementation of this procedure is somewhat arbitrary and therefore strongly dependent on the person evaluating the data. Additionally, the problem with recommended methods of selecting the presumed correct ROI is that there is no gold standard to compare the results to. Choosing the entire tumor volume in the first place increases the clearness in the definition of the volume of interest whereas individual slice selection suffers from intra observer variance. In summary, a recommendation to determine 3D perfusion parameters can be made, especially if volume data is already available and can

thus contribute to a more targeted therapy.

Comparison DCE CT

The DCE CT perfusion measurement is also feasible as a comparative modality or alternative in case of contraindication of an MRI measurement. It is therefore relevant whether comparable results can be achieved in a quantification. [Kierkels et al. \(2010\)](#) performed DCE MRI and CT perfusion parameters of rectal tumors with the Tofts model. They found similar results for K_{trans} , however could not find any correlation between v_e and v_p comparing both modalities. Although the scanner is of an older generation and the model used was a different one, the results seem to be in agreement with this study. PF values lie within the 1σ confidence interval, however PV and MTT differ significantly. A reasons may be the different viscosity of the CA, the effect could be overcome with a calibration of both. Additionally, total acquisition time in this study was only 30 s due to dose restriction. PF, which is mainly determined by the first part of the tissue curve, is therefore more accurate than PV and MTT, determined from the latter part of the tissue curve for which the measurement did not last long enough ([Cuenod and Balvay, 2013](#)).

Limitations - DCE In Vivo Study in Rectal Cancer Patients

Signal evaluation A general concern regarding DCE MRI is a lack of standardization concerning image acquisition routines and evaluation of obtained data. The combination of different factors such as insufficient coverage of the entire tumor volume, varying type and amount of CA, arbitrary slice selection regarding AIF or tumor or the application of different model functions and methods for analysis complicates the comparison among different studies ([Khalifa et al., 2014](#)). In this study, the choice of AIF and tumor slice followed the orientations used in previous studies and was strictly adhered to for all analyzed patients, guaranteeing best possible reproducibility ([Fusco et al., 2011](#)). Further improvement could be achieved by whole tumor analysis, accomplished by using the applied 3D sequences for tumor volume rendering, which would account for heterogeneous tumor tissue.

Gold standard A limitation of the study is that no gold standard method for measuring the perfusion parameters, e.g. scintigraphy or positron emission tomography was employed and compared to the models. However, the quantification methods were compared to each other rather than producing absolute values. As outlined before, the obtained values are found to be in the same range compared to other studies.

Motion artifacts No correction of motion artifacts was performed. Peristaltic movement in the abdominal region can lead to wave-like deviations in the obtained data and might have an influence on the results. However, as all methods were applied to the same DCE MRI data sets, any occurring motion artifacts would have affected the results equally and were not considered a major cause of error. Image registration approaches aiming to reduce motion artifacts in DCE MRI exams of rectal cancer should be considered in prospective studies.

Scanner The study used two different scanners to obtain the patient data. However, the exact magnetic field strength given for both scanners Magnetom Skyra and Magnetom Trio is $B_0 = 2.89$ T. Furthermore, a study investigated diffusion values at these two scanners previously, and came to the conclusion that nearly identical values could be obtained (Rao et al., 2012). Together with the fact that all other parameters are comparable and when calculating perfusion parameters, the baseline signal is subtracted, we assumed that the influence of the scanner difference is negligible.

General Limitations

CA Concentration No conversion of signal intensities to CA concentration was performed, but a linear relationship was assumed. As the conversion from signal intensities to CA concentration is performed before the application of the pharmacokinetic models, this can be regarded as a systematic error. It should have a similar effect on all methods and consequently it would not change the comparison presented in this work. For a more precise conversion of the measured signal into the concentration, the variable flip angle (VFA) method is used to initially quantify the measured T_1 value. From this, the concentration can be calculated via a linear relationship between T_1 and the concentration (Dickie et al., 2016). In some studies, an improved accuracy and precision has been shown by VFA application (Dickie et al., 2016; Dietrich et al., 2015) and therefore seems to be recommendable. However, these results are based on synthetic data and phantom measurements. In the above-mentioned work, corrections in homogeneity were first carried out on the B_1 -field for the precise quantification of T_1 values. Together with the VFA measurement itself, this results in a considerably longer measurement time, which is not easily acceptable for the patient. In addition, the acquired perfusion image has to be registered with the measured correction image afterwards. The method has also been applied in the human brain (Cheng and Wright, 2006), but in contrast to DCE measurements in the abdomen, fewer motion artifacts are produced and the measurement time is shorter in general. Correction measurements and application are therefore more justifiable in terms of time and are more realistic to perform. Nevertheless, the influence of conversion of signal intensities to CA concentration curves appears to be a contributing factor and needs to be examined in future research.

Software Studies have found that the reproducibility and accuracy of pharmacokinetic parameter measurements depend on the software package used. The studies of Beuzit et al. (2016) and Kudo et al. (2010) investigated different software for CT and MR and used the same source data for evaluation. Significant errors of up to 80% were found in the calculated pharmacokinetic DCE parameters, resulting in poor comparability. Different curve fitting algorithms, the definition of the AIF, namely patient- or population-based (Rata et al., 2016) for MRI and the tracer delay sensitivity in CT was given as main reasons. It would explain the difference between the rectal CT and MRI data compared in this thesis. Also deviations between values of this study and literature for the MR rectal perfusion parameters may have attributed to this.

Ethics and new studies The findings from both the phantom and retrospective rectal cancer study have not yet been applied to humans in a new study or in clinical practice. Compared to other procedures in MRI, which can be tested immediately on volunteers, a volunteer or even patient study is ethically not easily feasible due to the necessary administration of CA. Diseases of the kidney or an allergy to one of the CA components even completely exclude such an examination or it may only be carried out in an absolute emergency. The critical use of CA has been further strengthened by studies in recent years, which have observed that CA can be accumulated permanently in the brain and cause damage (Montagne et al., 2016; Taheri et al., 2016). Alternative techniques are DCE CT as described in this thesis or MRI perfusion measurements with ASL. However, there are pitfalls here as well. The time-resolved CT performed with modern devices has a lower dose than previously and is therefore feasible in general. But the accumulated dose is not negligible, especially in follow-up examinations. In addition, CA must be administered here as well, which in turn can lead to allergic reactions. The ASL measurement does not require any irradiation or CA at all, but due to the low signal a reliable quantification is not yet possible, especially in the abdomen. In summary, this encourages even more the development of valid human-like perfusion phantoms. With these, novel and improved methods can be developed and evaluated most effectively, making a transfer into clinical routine ethically justifiable. A phantom as presented here, applicable for simultaneous use with all three methods (DCE MRI, DCE CT and ASL) allowing comparisons among each other can set the standard for the selection of the most suitable method for each individual patient case while always achieving the same reliable, quantifiable results.

Clinical Transfer and Future Directions

A first step for data acquisition would certainly be to establish a consistent acquisition protocol. Such a standardized procedure has already been suggested in (Shukla-Dave et al., 2019). For the future, a more frequent adaptation of this protocol on the basis of advancing research results would be desirable. This would also make a comparison of retrospective data with one another much easier with regard to further development of the evaluation methods. However, in all performed experiments the main uncertainty factor is the manual and individual selection of evaluation methods. Study results thus are always dependent on the physicians, on their qualification and the consideration that a comprehensive selection means a large investment of time, which is unrealistic in clinical routine. However, for the measurement reproducibility and inter and intra site quality consistency and thus a robust quantification is inevitable. Ideally, a fully evaluated 4D data set of the possible AIF arteries and the tissue to be examined should be available. At best, a suitable model is automatically selected on this basis and under consideration of the physiological parameters. Based on the development in recent years, the use of neural networks for this issue is an obvious choice. Accordingly, further studies (Tönnies et al., 2020) have been started based on this work.

Conclusion 6

The quantification of tissue perfusion MRI is of great medical value for tumor diagnosis, treatment planning and therapy control yielding information about blood supply to organs and tumors non invasively. However, quantitative dynamic perfusion measurements are not yet fully established in the clinical routine. Reproducibility and comparison of quantitative parameters is difficult due to non-standardized examinations and data analysis.

The objective of this work was to evaluate the feasibility and to find improvements and limitations of Dynamic Contrast Enhanced (DCE) MRI in combination with pharmacokinetic modeling for perfusion quantification. To achieve this, two approaches were pursued.

In the first part, a multimodal perfusion phantom mimicking tissue at the capillary level was developed to investigate the reproducibility of perfusion parameters. In contrast to other phantoms, the phantom possesses two compartments that simulate intra- and extravascular space and thus better reflects human physiology. This enabled the application of a dual compartment model which allows the modeling of perfusion and permeability. Reproducible values both within repetitions of a series of measurements and in the repetition after one week were obtained. DCE MRI phantom results could be compared to those measured with Arterial Spin Labeling and DCE computer tomography, consistent results were achieved. The standardized setup enabled an investigation of an increased sampling rate on quantitative parameters. It could be shown that the signal deficit due to the used parallel imaging technique can be compensated by the higher sampling rate of AIF and tissue function. Significant influence on the fit quality and perfusion parameters and a reduction of intra measurement deviation could be shown in this case.

In the second part, the clinical evaluation of an in vivo perfusion study of rectal carcinomas was investigated and further developed. The bilateral selection of the arterial input function and the use of dual compartment models (Exchange and Uptake model) as well as tissue ROI selection in a heterogeneous tumor showed a significant influence on the quantification of perfusion parameters. The determination of permeability parameters enabled by pharmacokinetic modeling can provide additional information about the extravasation compared to model free approaches.

Summarized, the significant influence of pharmacokinetic modeling, AIF and tissue ROI selection and sampling rate on perfusion and permeability parameters could be demonstrated by a phantom and in vivo study. To ensure reliable quantification of DCE perfusion measurements in clinical routine, it will be essential in the future to initially extract and analyze all the small individual steps required in this context. Moreover, it will be necessary to identify the most suitable methods according to the state of the art and finally to combine them in a standardized form to a consistent measurement and analysis procedure. The combination of phantom and in vivo studies is an effective solution to jointly develop new strategies for the quantification of DCE MRI in the future. A prime example could be the implementation of neural networks. Data provided from simulations, phantoms and patient studies can be incorporated into neural networks. The gained knowledge could be of considerable benefit to this research topic.

List of Figures

2.1	Zeeman energy splitting in a hydrogen atom	10
2.2	Relaxation trajectory of the magnetization vector after excitation .	14
2.3	Relation of the bandwidth $\Delta\omega$ of the RF excitation pulse, the gradient strength G_z and the resulting slice thickness Δz	16
2.4	Spatial encoding	17
2.5	Decomposition of signal in the time domain to signal in the frequency domain using a Fourier Transformation	19
2.6	Spin echo sequence	20
2.7	Gradient echo sequence	21
2.8	T_1 -, T_2 - and PD-weighted image contrast dependent on TE and TR	22
2.9	X-ray tube and X-ray spectra	24
2.10	Attenuation of X-rays in water by Rayleigh scattering, Compton scattering and photoelectric effect	25
2.11	Relation of Object Space and Radon Space using Radon transformation and Fourier-Slice theorem	26
2.12	CT values in HU for different body materials and organs	27
2.13	DCE signal over time	31
2.14	ASL acquisition technique	32
2.15	Pulsed ASL and continuous ASL sequence	33
3.1	DCE operating steps	35
3.2	3T MR scanners	36
3.3	MR coils for patient and phantom measurement	37
3.4	TWIST sequence	38
3.5	Parallel imaging with GRAPPA	39
3.6	CA Calibration - CT and MRI measurement	41
3.7	CT scanner	42
3.8	2CX and 2CU model	45
3.9	Construction scheme of the dialyzer	47
3.10	Experimental phantom setup	48
3.11	Utilization of the perfusion phantom	48
3.12	Signal evaluation of perfusion phantom data	50
3.13	Experimental setups for the perfusion phantom study.	52
3.14	Anatomical structure of the rectum with arteries	57
3.15	MR image of the abdomen with AIF and rectal tumor ROI	57
3.16	3D representation of rectal tumor	59
3.17	CT image of the abdomen with AIF and rectal tumor ROI	60

4.1	MR CA Calibration	62
4.2	CT CA Calibration	62
4.3	Phantom feasibility: Washout	63
4.4	Phantom feasibility: AIF and tissue function	65
4.5	Phantom feasibility: Additional flow in dialysate circuit	66
4.6	Tissue signal and 2CX fit	66
4.7	Parameter maps in artificial tissue	67
4.8	PF maps for different PAT / T_s	69
4.9	Boxplot different PAT / T_s	70
4.10	Phantom measurement using DCE MRI and ASL	71
4.11	Phantom feasibility: Washout CT	72
4.12	Phantom feasibility: AIF and tissue function CT	73
4.13	Perfusion phantom application in the CT	73
4.14	Evaluation ROIs and signal of left and right AIF	75
4.15	Parameter maps for left and right AIF	76
4.16	Boxplots of perfusion parameters using left and right AIF and FD, 2CU and 2CX	77
4.17	Boxplots of permeability and fit parameters using left and right AIF and 2CU and 2CX	78
4.18	Boxplots of differences of PF_{l-r} , PV_{l-r} , MTT_{l-r} , $PSAP_{l-r}$ and EF_{l-r} using the FD, 2CX and 2CU	79
4.19	Tumor tissue signal over time and fit with 2CU and 2CX	81
4.20	PF, PV and MTT in tumor for 2CU, 2CX and FD	81
4.21	Bland-Altman plot comparing FD, 2CU, 2CX for PF, PV and MTT	82
4.22	2D and 3D tumor perfusion parameters	85
4.23	3D PF parameter maps in rectum tumor tissue	85

List of Tables

2.1	Tissue relaxation times T_1 and T_2 of 1H at magnetic field strength $B_0 = 3T$	13
3.1	Imaging parameters of the MR CA calibration measurement.	41
3.2	Imaging parameters of the quantitative DCE MRI phantom study.	49
3.3	Imaging parameters of the quantitative ASL MRI phantom study.	54
3.4	Imaging parameters of the quantitative DCE CT phantom study.	54
3.5	Imaging parameters of the quantitative DCE MRI in vivo study in rectal cancer patients	55
4.1	Gamma variate fit for AIF and tissue	64
4.2	Phantom reproducibility: Parameters for five subsequent measurements	66
4.3	Perfusion parameters at $t = 0$ and $t = 1$ week	67
4.4	Perfusion parameters with additional flow in dialysate circuit	68
4.5	PF and fit quality for different PAT / T_s	68
4.6	Gamma variate fit for AIF and tissue for DCE CT	72
4.7	Perfusion parameters for left and right AIF applying FD, 2CX and 2CU	75
4.8	Perfusion, permeability and quality of fit parameters for tumor tissue, healthy rectum wall and different cancer stages for FD, 2CU and 2CX	83
4.9	Pairwise statistical test between FD, 2CU and 2CX	84
4.10	2D and 3D tumor perfusion parameters.	86
4.11	Perfusion parameters using the FD approach for DCE CT	86

Acronyms

CM Compartment Model

2CM Dual Compartment Model

2CU Dual Compartment Uptake Model

2CX Dual Compartment Exchange Model

AIF Arterial Input Function

ASL Arterial Spin Labeling

BF Blood Flow

BV Blood Volume

CA Contrast Agent

CASL Continuous Arterial Spin Labeling

CT Computer Tomography

DCE Dynamic Contrast Enhanced

DSC Dynamic Susceptibility Contrast

EES Extracellular Extravascular Space

EF Extraction Fraction

EV Extracellular Extravascular Volume

FID Free Induction Decay

FD Fast Deconvolution

FOV Field Of View

Gd Gadolinium

GRAPPA Generalized Autocalibrating Partially Parallel Acquisition

HCT Hematocrit

HU Hounsfield Units

MRI Magnetic Resonance Imaging

MTT Mean Transit Time

NMR Nuclear Magnetic Resonance

PASL Pulsed Arterial Spin Labeling

PAT Parallel Acquisition Technique

PET Positron Emission Tomography

PF Plasma Flow

PSAP Permeability Surface Area Product

PV Plasma Volume

ROI Region of Interest

RF Radio Frequency

SNR Signal to Noise Ratio

TWIST Time-Resolved Imaging with Stochastic Trajectories

VFA Variable Flip Angle

References

- Abragam, A. (1961). *The principles of nuclear magnetism*. Number 32. Oxford university press.
- Aerts, H. J., Jaspers, K., and Backes, W. H. (2011). The precision of pharmacokinetic parameters in dynamic contrast-enhanced magnetic resonance imaging: the effect of sampling frequency and duration. *Physics in Medicine & Biology*, 56(17):5665.
- Alkadhi, H., Leschka, S., Stolzmann, P., and Scheffel, H. (2011). *Wie funktioniert CT?*, volume 4. Springer.
- Alsop, D. C., Detre, J. A., Golay, X., Günther, M., Hendrikse, J., Hernandez-Garcia, L., Lu, H., MacIntosh, B. J., Parkes, L. M., Smits, M., et al. (2015). Recommended implementation of arterial spin-labeled perfusion mri for clinical applications: a consensus of the ismrn perfusion study group and the european consortium for asl in dementia. *Magnetic resonance in medicine*, 73(1):102–116.
- Attenberger, U., Pilz, L., Morelli, J., Hausmann, D., Doyon, F., Hofheinz, R., Kienle, P., Post, S., Michaely, H., Schoenberg, S., et al. (2014). Multi-parametric mri of rectal cancer—do quantitative functional mr measurements correlate with radiologic and pathologic tumor stages? *European journal of radiology*, 83(7):1036–1043.
- Beuzit, L., Eliat, P.-A., Brun, V., Ferré, J.-C., Gandon, Y., Bannier, E., and Saint-Jalmes, H. (2016). Dynamic contrast-enhanced mri: Study of inter-software accuracy and reproducibility using simulated and clinical data. *Journal of magnetic resonance imaging*, 43(6):1288–1300.
- Bloch, F., Hansen, W., and Packard, M. (1946). Physical review. *Phys Rev*, 70:460–473.
- Bloembergen, N., Purcell, E. M., and Pound, R. V. (1948). Relaxation effects in nuclear magnetic resonance absorption. *Physical review*, 73(7):679.
- Brix, G., Kiessling, F., Lucht, R., Darai, S., Wasser, K., Delorme, S., and Griebel, J. (2004). Microcirculation and microvasculature in breast tumors: pharmacokinetic analysis of dynamic mr image series. *Magnetic Resonance in Medicine: An Official Journal of the International Society for Magnetic Resonance in Medicine*, 52(2):420–429.

- Brix, G., Semmler, W., Port, R., Schad, L. R., Layer, G., and Lorenz, W. J. (1991). Pharmacokinetic parameters in cns gd-dtpa enhanced mr imaging. *Journal of computer assisted tomography*, 15(4):621–628.
- Buxton, R. B., Frank, L. R., Wong, E. C., Siewert, B., Warach, S., and Edelman, R. R. (1998). A general kinetic model for quantitative perfusion imaging with arterial spin labeling. *Magnetic resonance in medicine*, 40(3):383–396.
- Buzug, T. M. (2011). Computed tomography. In *Springer Handbook of Medical Technology*, pages 311–342. Springer.
- Calamante, F. (2005). Bolus dispersion issues related to the quantification of perfusion mri data. *Journal of Magnetic Resonance Imaging: An Official Journal of the International Society for Magnetic Resonance in Medicine*, 22(6):718–722.
- Calamante, F. (2013). Arterial input function in perfusion mri: a comprehensive review. *Progress in nuclear magnetic resonance spectroscopy*, 74:1–32.
- Calamante, F., Gadian, D. G., and Connelly, A. (2000). Delay and dispersion effects in dynamic susceptibility contrast mri: simulations using singular value decomposition. *Magnetic Resonance in Medicine: An Official Journal of the International Society for Magnetic Resonance in Medicine*, 44(3):466–473.
- Ceelen, W., Smeets, P., Backes, W., Van Damme, N., Boterberg, T., Demetter, P., Bouckenoghe, I., De Visschere, M., Peeters, M., and Pattyn, P. (2006). Noninvasive monitoring of radiotherapy-induced microvascular changes using dynamic contrast enhanced magnetic resonance imaging (dce-mri) in a colorectal tumor model. *International Journal of Radiation Oncology* Biology* Physics*, 64(4):1188–1196.
- Chan, A. A. and Nelson, S. J. (2004). Simplified gamma-variate fitting of perfusion curves. In *2004 2nd IEEE International Symposium on Biomedical Imaging: Nano to Macro (IEEE Cat No. 04EX821)*, pages 1067–1070. IEEE.
- Cheng, H.-L. M. and Wright, G. A. (2006). Rapid high-resolution t1 mapping by variable flip angles: accurate and precise measurements in the presence of radiofrequency field inhomogeneity. *Magnetic Resonance in Medicine: An Official Journal of the International Society for Magnetic Resonance in Medicine*, 55(3):566–574.
- Cormack, A. (1973). Reconstruction of densities from their projections, with applications in radiological physics. *Physics in Medicine & Biology*, 18(2):195.
- Cuenod, C. and Balvay, D. (2013). Perfusion and vascular permeability: basic concepts and measurement in dce-ct and dce-mri. *Diagnostic and interventional imaging*, 94(12):1187–1204.

- Cutajar, M., Mendichovszky, I., Tofts, P., and Gordon, I. (2010). The importance of aif roi selection in dce-mri renography: reproducibility and variability of renal perfusion and filtration. *European journal of radiology*, 74(3):e154–e160.
- Cutajar, M., Thomas, D. L., Hales, P. W., Banks, T., Clark, C. A., and Gordon, I. (2014). Comparison of asl and dce mri for the non-invasive measurement of renal blood flow: quantification and reproducibility. *European radiology*, 24(6):1300–1308.
- Dai, W., Garcia, D., De Bazelaire, C., and Alsop, D. C. (2008). Continuous flow-driven inversion for arterial spin labeling using pulsed radio frequency and gradient fields. *Magnetic Resonance in Medicine: An Official Journal of the International Society for Magnetic Resonance in Medicine*, 60(6):1488–1497.
- Davenport, M. S., Heye, T., Dale, B. M., Horvath, J. J., Breault, S. R., Feuerlein, S., Bashir, M. R., Boll, D. T., and Merkle, E. M. (2013). Inter-and intra-rater reproducibility of quantitative dynamic contrast enhanced mri using twist perfusion data in a uterine fibroid model. *Journal of Magnetic Resonance Imaging*, 38(2):329–335.
- De Bazelaire, C. M., Duhamel, G. D., Rofsky, N. M., and Alsop, D. C. (2004). Mr imaging relaxation times of abdominal and pelvic tissues measured in vivo at 3.0 t: preliminary results. *Radiology*, 230(3):652–659.
- Detre, J. A., Leigh, J. S., Williams, D. S., and Koretsky, A. P. (1992). Perfusion imaging. *Magnetic resonance in medicine*, 23(1):37–45.
- DeVries, A. F., Griebel, J., Kremser, C., Judmaier, W., Gneiting, T., Kreczy, A., Öfner, D., Pfeiffer, K.-P., Brix, G., and Lukas, P. (2001). Tumor microcirculation evaluated by dynamic magnetic resonance imaging predicts therapy outcome for primary rectal carcinoma. *Cancer research*, 61(6):2513–2516.
- DeVries, A. F., Piringer, G., Kremser, C., Judmaier, W., Saely, C. H., Lukas, P., and Öfner, D. (2014). Pretreatment evaluation of microcirculation by dynamic contrast-enhanced magnetic resonance imaging predicts survival in primary rectal cancer patients. *International Journal of Radiation Oncology* Biology* Physics*, 90(5):1161–1167.
- Dickie, B. R., Banerji, A., Kershaw, L. E., McPartlin, A., Choudhury, A., West, C. M., and Rose, C. J. (2016). Improved accuracy and precision of tracer kinetic parameters by joint fitting to variable flip angle and dynamic contrast enhanced mri data. *Magnetic resonance in medicine*, 76(4):1270–1281.
- Dietrich, O., Freiermuth, M., Willerding, L., Reiser, M. F., and Peller, M. (2015). Flip angle-optimized fast dynamic t1 mapping with a 3d gradient echo sequence. *Magnetic resonance in medicine*, 73(3):1158–1163.

- Dixon, W. T., Du, L. N., Faul, D. D., Gado, M., and Rossnick, S. (1986). Projection angiograms of blood labeled by adiabatic fast passage. *Magnetic resonance in medicine*, 3(3):454–462.
- Donaldson, S. B., West, C. M., Davidson, S. E., Carrington, B. M., Hutchison, G., Jones, A. P., Sourbron, S. P., and Buckley, D. L. (2010). A comparison of tracer kinetic models for t1-weighted dynamic contrast-enhanced mri: Application in carcinoma of the cervix. *Magnetic Resonance in Medicine*, 63(3):691–700.
- Dujardin, M., Sourbron, S., Luypaert, R., Verbeelen, D., and Stadnik, T. (2005). Quantification of renal perfusion and function on a voxel-by-voxel basis: a feasibility study. *Magnetic Resonance in Medicine: An Official Journal of the International Society for Magnetic Resonance in Medicine*, 54(4):841–849.
- Eastwood, J. D., Lev, M. H., Wintermark, M., Fitzek, C., Barboriak, D. P., Delong, D. M., Lee, T.-Y., Azhari, T., Herzau, M., Chilukuri, V. R., et al. (2003). Correlation of early dynamic ct perfusion imaging with whole-brain mr diffusion and perfusion imaging in acute hemispheric stroke. *American Journal of Neuroradiology*, 24(9):1869–1875.
- Edelman, R. R., Siewert, B., Darby, D. G., Thangaraj, V., Nobre, A. C., Mesulam, M. M., and Warach, S. (1994). Qualitative mapping of cerebral blood flow and functional localization with echo-planar mr imaging and signal targeting with alternating radio frequency. *Radiology*, 192(2):513–520.
- Engelstad, B. and Wolf, G. (1988). Contrast agents. *Magnetic resonance imaging*. St Louis: CV Mosby, pages 161–81.
- Fieselmann, A., Kowarschik, M., Ganguly, A., Hornegger, J., and Fahrig, R. (2011). Deconvolution-based ct and mr brain perfusion measurement: theoretical model revisited and practical implementation details. *International Journal of Biomedical Imaging*, 2011.
- Foltz, W., Driscoll, B., Lee, S. L., Nayak, K., Nallapareddy, N., Fatemi, A., Ménard, C., Coolens, C., and Chung, C. (2019). Phantom validation of dce-mri magnitude and phase-based vascular input function measurements. *Tomography*, 5(1):77.
- Fusco, R and Sansone, M., Petrillo, M., Avallone, A., Delrio, P., and Petrillo, A. (2011). *Dynamic Contrast Enhanced Magnetic Resonance Imaging in Rectal Cancer, Rectal Cancer - A Multidisciplinary Approach to Management*. INTECH Open Access Publishe.
- Gaa, T., Neumann, W., Sudarski, S., Attenberger, U. I., Schönberg, S. O., Schad, L. R., and Zöllner, F. G. (2017). Comparison of perfusion models for quantitative t1 weighted dce-mri of rectal cancer. *Scientific reports*, 7(1):12036.

- Gaass, T., Schneider, M. J., Dietrich, O., Ingrisch, M., and Dinkel, J. (2017). Quantitative dynamic contrast-enhanced mri of a 3-dimensional artificial capillary network. *Medical physics*, 44(4):1462–1469.
- Gallagher, T. A., Nemeth, A. J., and Hacein-Bey, L. (2008). An introduction to the fourier transform: relationship to mri. *American journal of roentgenology*, 190(5):1396–1405.
- Ginsburg, S. B., Taimen, P., Merisaari, H., Vainio, P., Boström, P. J., Aronen, H. J., Jambor, I., and Madabhushi, A. (2016). Patient-specific pharmacokinetic parameter estimation on dynamic contrast-enhanced mri of prostate: Preliminary evaluation of a novel aif-free estimation method. *Journal of Magnetic Resonance Imaging*, 44(6):1405–1414.
- Goh, V., Halligan, S., Gharpuray, A., Wellsted, D., Sundin, J., and Bartram, C. I. (2008). Quantitative assessment of colorectal cancer tumor vascular parameters by using perfusion ct: influence of tumor region of interest. *Radiology*, 247(3):726–732.
- Gowland, P., Mansfield, P., Bullock, P., Stehling, M., Worthington, B., and Firth, J. (1992). Dynamic studies of gadolinium uptake in brain tumors using inversion-recovery echo-planar imaging. *Magnetic resonance in medicine*, 26(2):241–258.
- Gregori, J. (2009). *Dynamic Arterial Spin Labeling Measurements of Physiological Parameters-Permeability and Oxygenation*. PhD thesis.
- Griswold, M. A., Jakob, P. M., Heidemann, R. M., Nittka, M., Jellus, V., Wang, J., Kiefer, B., and Haase, A. (2002). Generalized autocalibrating partially parallel acquisitions (grappa). *Magnetic Resonance in Medicine: An Official Journal of the International Society for Magnetic Resonance in Medicine*, 47(6):1202–1210.
- Haacke, E. M., Brown, R. W., Thompson, M. R., Venkatesan, R., et al. (1999). *Magnetic resonance imaging: physical principles and sequence design*, volume 82. Wiley-Liss New York:.
- Hahn, E. L. (1950). Spin echoes. *Physical review*, 80(4):580.
- Hansen, J., Wielpütz, M., Pahn, G., Kauczor, H. U., Stiller, W., et al. (2014). Quantitative dual-energy computed tomography imaging: Evaluation of system performance regarding iodine quantification accuracy. European Congress of Radiology 2014.
- Hayes, C., Padhani, A. R., and Leach, M. O. (2002). Assessing changes in tumour vascular function using dynamic contrast-enhanced magnetic resonance imaging. *NMR in Biomedicine: An International Journal Devoted to the Development and Application of Magnetic Resonance In Vivo*, 15(2):154–163.
- Heilmann, M., Vautier, J., Robert, P., and Volk, A. (2009). In vitro setup to study permeability characteristics of contrast agents by mri. *Contrast media & molecular imaging*, 4(2):66–72.

- Hounsfield, G. N. (1973). Computerized transverse axial scanning (tomography): Part 1. description of system. *The British journal of radiology*, 46(552):1016–1022.
- Ingrisch, M. and Sourbron, S. (2013). Tracer-kinetic modeling of dynamic contrast-enhanced mri and ct: a primer. *Journal of pharmacokinetics and pharmacodynamics*, 40(3):281–300.
- Jerosch-Herold, M., Seethamraju, R. T., Swingen, C. M., Wilke, N. M., and Stillman, A. E. (2004). Analysis of myocardial perfusion mri. *Journal of Magnetic Resonance Imaging: An Official Journal of the International Society for Magnetic Resonance in Medicine*, 19(6):758–770.
- Khalifa, F., Soliman, A., El-Baz, A., Abou El-Ghar, M., El-Diasty, T., Gimel'farb, G., Ouseph, R., and Dwyer, A. C. (2014). Models and methods for analyzing dce-mri: A review. *Medical physics*, 41(12):124301.
- Kierkels, R. G., Backes, W. H., Janssen, M. H., Buijsen, J., Beets-Tan, R. G., Lambin, P., Lammering, G., Oellers, M. C., and Aerts, H. J. (2010). Comparison between perfusion computed tomography and dynamic contrast-enhanced magnetic resonance imaging in rectal cancer. *International Journal of Radiation Oncology* Biology* Physics*, 77(2):400–408.
- Knight, S. P., Browne, J. E., Meaney, J. F. M., and Fagan, A. J. (2017). Quantitative effects of acquisition duration and temporal resolution on the measurement accuracy of prostate dynamic contrast-enhanced mri data: a phantom study. *Magnetic Resonance Materials in Physics, Biology and Medicine*, 30(5):461–471.
- Koh, T. S., Bisdas, S., Koh, D. M., and Thng, C. H. (2011). Fundamentals of tracer kinetics for dynamic contrast-enhanced mri. *Journal of Magnetic Resonance Imaging*, 34(6):1262–1276.
- Koh, T. S., Ng, Q. S., Thng, C. H., Kwek, J. W., Kozarski, R., and Goh, V. (2013). Primary colorectal cancer: use of kinetic modeling of dynamic contrast-enhanced ct data to predict clinical outcome. *Radiology*, 267(1):145–154.
- Krämer, P. (2014). *Entwicklung von Methoden zur schnellen 3D Messung der T1- und T2-Relaxationszeiten in-vivo mit Steady-State Bildgebung bei 3 Tesla*. PhD thesis.
- Kremser, C., Trieb, T., Rudisch, A., Judmaier, W., and de Vries, A. (2007). Dynamic t1 mapping predicts outcome of chemoradiation therapy in primary rectal carcinoma: sequence implementation and data analysis. *Journal of Magnetic Resonance Imaging: An Official Journal of the International Society for Magnetic Resonance in Medicine*, 26(3):662–671.
- Kudo, K., Sasaki, M., Yamada, K., Momoshima, S., Utsunomiya, H., Shirato, H., and Ogasawara, K. (2010). Differences in ct perfusion maps generated by different commercial software: quantitative analysis by using identical source data of acute stroke patients. *Radiology*, 254(1):200–209.

- Kwong, K. K., Belliveau, J. W., Chesler, D. A., Goldberg, I. E., Weisskoff, R. M., Poncelet, B. P., Kennedy, D. N., Hoppel, B. E., Cohen, M. S., and Turner, R. (1992). Dynamic magnetic resonance imaging of human brain activity during primary sensory stimulation. *Proceedings of the National Academy of Sciences*, 89(12):5675–5679.
- Lassen, N. A. and Perl, W. (1979). *Tracer kinetic methods in medical physiology*. Raven Press.
- Laubenberger, T. and Laubenberger, J. (1999). *Technik der medizinischen Radiologie: Diagnostik, Strahlentherapie, Strahlenschutz; für Ärzte, Medizinstudenten und MTRA; [mit 71 Tabellen]*. Deutscher Ärzteverlag.
- Lauterbur, P. C. et al. (1973). *Image formation by induced local interactions: examples employing nuclear magnetic resonance*.
- Levitt, M. H. (2001). *Spin dynamics: basics of nuclear magnetic resonance*. John Wiley & Sons.
- Leyendecker, P., Faucher, V., Labani, A., Noblet, V., Lefebvre, F., Magotteaux, P., Ohana, M., and Roy, C. (2019). Prospective evaluation of ultra-low-dose contrast-enhanced 100-kv abdominal computed tomography with tin filter: effect on radiation dose reduction and image quality with a third-generation dual-source ct system. *European radiology*, 29(4):2107–2116.
- Li, X., Huang, W., and Rooney, W. D. (2012). Signal-to-noise ratio, contrast-to-noise ratio and pharmacokinetic modeling considerations in dynamic contrast-enhanced magnetic resonance imaging. *Magnetic resonance imaging*, 30(9):1313–1322.
- Luypaert, R., Ingrisich, M., Sourbron, S., and de Mey, J. (2012). The akaike information criterion in dce-mri: Does it improve the haemodynamic parameter estimates? *Physics in Medicine & Biology*, 57(11):3609.
- Luypaert, R., Sourbron, S., and de Mey, J. (2011). Validity of perfusion parameters obtained using the modified tofts model: a simulation study. *Magnetic resonance in medicine*, 65(5):1491–1497.
- Mansfield, P. (1977). Multi-planar image formation using nmr spin echoes. *Journal of Physics C: Solid State Physics*, 10(3):L55.
- Meier, P. and Zierler, K. L. (1954). On the theory of the indicator-dilution method for measurement of blood flow and volume. *Journal of applied physiology*, 6(12):731–744.
- Mendichovszky, I., Cutajar, M., and Gordon, I. (2009). Reproducibility of the aortic input function (aif) derived from dynamic contrast-enhanced magnetic resonance imaging (dce-mri) of the kidneys in a volunteer study. *European journal of radiology*, 71(3):576–581.

- Michaely, H. J., Schoenberg, S. O., Oesingmann, N., Ittrich, C., Buhlig, C., Friedrich, D., Struwe, A., Rieger, J., Reininger, C., Samtleben, W., et al. (2006). Renal artery stenosis: functional assessment with dynamic mr perfusion measurements-feasibility study. *Radiology*, 238(2):586–596.
- Mie, M. B. (2011). *Quantification of Brain Tissue Oxygenation: Comparison of Different Gradient Echo/Spin Echo MRI Techniques at 3 Tesla*. PhD thesis.
- Miles, K., Lee, T., Goh, V., et al. (2012). Current status of dynamic contrast enhanced-computed tomography for the assessment of tumour vascular support. *Eur Radiol*, 22:1430–1441.
- Montagne, A., Toga, A. W., and Zlokovic, B. V. (2016). Blood-brain barrier permeability and gadolinium: benefits and potential pitfalls in research. *JAMA neurology*, 73(1):13–14.
- Ning, J., Schubert, T., Johnson, K. M., Roldán-Alzate, A., Chen, H., Yuan, C., and Reeder, S. B. (2018). Vascular input function correction of inflow enhancement for improved pharmacokinetic modeling of liver dce-mri. *Magnetic resonance in medicine*, 79(6):3093–3102.
- Oberholzer, K., Menig, M., Pohlmann, A., Junginger, T., Heintz, A., Kreft, A., Hansen, T., Schneider, A., Lollert, A., Schmidberger, H., et al. (2013). Rectal cancer: Assessment of response to neoadjuvant chemoradiation by dynamic contrast-enhanced mri. *Journal of Magnetic Resonance Imaging*, 38(1):119–126.
- Østergaard, L., Sorensen, A. G., Kwong, K. K., Weisskoff, R. M., Gyldensted, C., and Rosen, B. R. (1996a). High resolution measurement of cerebral blood flow using intravascular tracer bolus passages. part ii: Experimental comparison and preliminary results. *Magnetic resonance in medicine*, 36(5):726–736.
- Østergaard, L., Weisskoff, R. M., Chesler, D. A., Gyldensted, C., and Rosen, B. R. (1996b). High resolution measurement of cerebral blood flow using intravascular tracer bolus passages. part i: Mathematical approach and statistical analysis. *Magnetic resonance in medicine*, 36(5):715–725.
- Østergaard, L., Weisskoff, R. M., Chesler, D. A., Gyldensted, C., and Rosen, B. R. (1996c). High resolution measurement of cerebral blood flow using intravascular tracer bolus passages. part i: Mathematical approach and statistical analysis. *Magnetic resonance in medicine*, 36(5):715–725.
- Otazo, R., Kim, D., Axel, L., and Sodickson, D. K. (2010). Combination of compressed sensing and parallel imaging for highly accelerated first-pass cardiac perfusion mri. *Magnetic resonance in medicine*, 64(3):767–776.
- Othman, A. E., Falkner, F., Weiss, J., Kruck, S., Grimm, R., Martirosian, P., Nikolaou, K., and Notohamiprodjo, M. (2016). Effect of temporal resolution on diagnostic performance of dynamic contrast-enhanced magnetic resonance imaging of the prostate. *Investigative radiology*, 51(5):290–296.

- Otton, J., Morton, G., Schuster, A., Bigalke, B., Marano, R., Olivotti, L., Nagel, E., and Chiribiri, A. (2013). A direct comparison of the sensitivity of ct and mr cardiac perfusion using a myocardial perfusion phantom. *Journal of cardiovascular computed tomography*, 7(2):117–124.
- Parkes, L. M. and Tofts, P. S. (2002). Improved accuracy of human cerebral blood perfusion measurements using arterial spin labeling: accounting for capillary water permeability. *Magnetic Resonance in Medicine: An Official Journal of the International Society for Magnetic Resonance in Medicine*, 48(1):27–41.
- Petersen, E., Zimine, I., Ho, Y. L., and Golay, X. (2006). Non-invasive measurement of perfusion: a critical review of arterial spin labelling techniques. *The British journal of radiology*, 79(944):688–701.
- Pettigrew, R. I., Avruch, L., Dannels, W., Coumans, J., and Bernardino, M. (1986). Fast-field-echo mr imaging with gd-dtpa: physiologic evaluation of the kidney and liver. *Radiology*, 160(2):561–563.
- Purcell, E. M., Torrey, H. C., and Pound, R. V. (1946). Resonance absorption by nuclear magnetic moments in a solid. *Physical review*, 69(1-2):37.
- Radon, J. (1917). On the determination of functions from their integrals along certain manifolds. *Ber. Verh, Sachs Akad Wiss.*, 69:262–277.
- Rajan, S., Herbertson, L., Bernardo, M., and Choyke, P. (2014). A dialyzer-based flow system for validating dynamic contrast enhanced mr image acquisition. *Magnetic resonance in medicine*, 72(1):41–48.
- Rao, R. K., Riffel, P., Meyer, M., Kettner, P. J., Lemke, A., Haneder, S., Schoenberg, S. O., and Michaely, H. J. (2012). Implementation of dual-source rf excitation in 3 t mr-scanners allows for nearly identical adc values compared to 1.5 t mr scanners in the abdomen. *PloS one*, 7(2).
- Rata, M., Collins, D. J., Darcy, J., Messiou, C., Tunariu, N., Desouza, N., Young, H., Leach, M. O., and Orton, M. R. (2016). Assessment of repeatability and treatment response in early phase clinical trials using dce-mri: comparison of parametric analysis using mr-and ct-derived arterial input functions. *European radiology*, 26(7):1991–1998.
- Roemer, P. B., Edelstein, W. A., Hayes, C. E., Souza, S. P., and Mueller, O. M. (1990). The nmr phased array. *Magnetic resonance in medicine*, 16(2):192–225.
- Romain, B., Rouet, L., Ohayon, D., Lucidarme, O., d'Alche Buc, F., and Letort, V. (2017). Parameter estimation of perfusion models in dynamic contrast-enhanced imaging: a unified framework for model comparison. *Medical image analysis*, 35:360–374.
- Röntgen, W. C. (1896). On a new kind of rays. *Science*, 3(59):227–231.
- Ross, B., Chenevert, T., and Rehemtulla, A. (2002). Magnetic resonance imaging in cancer research. *European Journal of Cancer*, 38(16):2147–2156.

- Rowland, M., Benet, L. Z., and Graham, G. G. (1973). Clearance concepts in pharmacokinetics. *Journal of pharmacokinetics and biopharmaceutics*, 1(2):123–136.
- Runge, V. M., Clanton, J. A., Herzer, W., Gibbs, S., Price, A., Partain, C., and James Jr, A. (1984). Intravascular contrast agents suitable for magnetic resonance imaging. *Radiology*, 153(1):171–176.
- Sabiston, D. C., Townsend, C. M., Beauchamp, R., et al. (2001). *Sabiston textbook of surgery: the biological basis of modern surgical practice*. WB Saunders.
- Sahani, D. V., Kalva, S. P., Hamberg, L. M., Hahn, P. F., Willett, C. G., Saini, S., Mueller, P. R., and Lee, T.-Y. (2005). Assessing tumor perfusion and treatment response in rectal cancer with multisection ct: initial observations. *Radiology*, 234(3):785–792.
- Sanghera, B., Banerjee, D., Khan, A., Simcock, I., Stirling, J. J., Glynne-Jones, R., and Goh, V. (2012). Reproducibility of 2d and 3d fractal analysis techniques for the assessment of spatial heterogeneity of regional blood flow in rectal cancer. *Radiology*, 263(3):865–873.
- Sauerbrey, A., Hindel, S., Maaß, M., Krüger, C., Wissmann, A., Kramer, M., Nafz, B., and Lüdemann, L. (2014). Establishment of a swine model for validation of perfusion measurement by dynamic contrast-enhanced magnetic resonance imaging. *BioMed research international*, 2014.
- Shahbazi-Gahrouei, D., Williams, M., and Allen, B. (2001). In vitro study of relationship between signal intensity and gadolinium-dtpa concentration at high magnetic field strength. *Australasian radiology*, 45(3):298–304.
- Shukla-Dave, A., Obuchowski, N. A., Chenevert, T. L., Jambawalikar, S., Schwartz, L. H., Malyarenko, D., Huang, W., Noworolski, S. M., Young, R. J., Shiroishi, M. S., et al. (2019). Quantitative imaging biomarkers alliance (qiba) recommendations for improved precision of dwi and dce-mri derived biomarkers in multicenter oncology trials. *Journal of Magnetic Resonance Imaging*, 49(7):e101–e121.
- Siemens, A. (2004). Magnetom trio operating instruction. 2nd ed., Siemens AG, Wittelsbacher Platz 2, 80333 München.
- Siemens, A. (2012). Magnetom skyra owner's manual. 2nd ed., Siemens AG, Wittelsbacher Platz 2, 80333 München.
- Song, T., Laine, A. F., Chen, Q., Rusinek, H., Bokacheva, L., Lim, R. P., Laub, G., Kroeker, R., and Lee, V. S. (2009). Optimal k-space sampling for dynamic contrast-enhanced mri with an application to mr renography. *Magnetic Resonance in Medicine: An Official Journal of the International Society for Magnetic Resonance in Medicine*, 61(5):1242–1248.
- Sourbron, S. (2010). Technical aspects of mr perfusion. *European journal of radiology*, 76(3):304–313.

- Sourbron, S. and Buckley, D. L. (2011). Tracer kinetic modelling in mri: estimating perfusion and capillary permeability. *Physics in Medicine & Biology*, 57(2):R1.
- Sourbron, S., Luybaert, R., Van Schuerbeek, P., Dujardin, M., and Stadnik, T. (2004). Choice of the regularization parameter for perfusion quantification with mri. *Physics in Medicine & Biology*, 49(14):3307.
- Sourbron, S. P. and Buckley, D. L. (2013). Classic models for dynamic contrast-enhanced mri. *NMR in Biomedicine*, 26(8):1004–1027.
- Stanisz, G. J., Odobina, E. E., Pun, J., Escaravage, M., Graham, S. J., Bronskill, M. J., and Henkelman, R. M. (2005). T1, t2 relaxation and magnetization transfer in tissue at 3t. *Magnetic Resonance in Medicine: An Official Journal of the International Society for Magnetic Resonance in Medicine*, 54(3):507–512.
- Sudarski, S., Henzler, T., Floss, T., Gaa, T., Meyer, M., Haubenreisser, H., Schoenberg, S. O., and Attenberger, U. I. (2018). Variability and reproducibility of 3 rd-generation dual-source dynamic volume perfusion ct parameters in comparison to mr-perfusion parameters in rectal cancer. *Scientific reports*, 8(1):1–9.
- Taheri, S., Shah, N. J., and Rosenberg, G. A. (2016). Analysis of pharmacokinetics of gd-dtpa for dynamic contrast-enhanced magnetic resonance imaging. *Magnetic resonance imaging*, 34(7):1034–1040.
- Tofts, P., Brix, G., Buckley, D., Evelhoch, J., Henderson, E., and Knopp, M. (1999). Estimating kinetic parameters from dynamic contrast-enhanced t (1)-weighted mri of a diffusable tracer: standardized quantities and symbols. *J Magn Reson Imaging*, 10:223–32.
- Tofts, P. S. (2010). T1-weighted dce imaging concepts: modelling, acquisition and analysis. *signal*, 500(450):400.
- Tofts, P. S., Cutajar, M., Mendichovszky, I. A., Peters, A. M., and Gordon, I. (2012). Precise measurement of renal filtration and vascular parameters using a two-compartment model for dynamic contrast-enhanced mri of the kidney gives realistic normal values. *European radiology*, 22(6):1320–1330.
- Tong, T., Sun, Y., Gollub, M. J., Peng, W., Cai, S., Zhang, Z., and Gu, Y. (2015). Dynamic contrast-enhanced mri: Use in predicting pathological complete response to neoadjuvant chemoradiation in locally advanced rectal cancer. *Journal of Magnetic Resonance Imaging*, 42(3):673–680.
- Tönnes, C., Janssen, S., Schnurr, A.-K., Uhrig, T., Chung, K., Schad, L. R., and Zöllner, F. G. (2020). Deterministic arterial input function determination in dce-mri for automation of quantitative perfusion calculation of colorectal cancer. *Submitted to: Computerized Medical Imaging and Graphics*, submission date 27. 03.2020.

- Van Vaals, J. J., Brummer, M. E., Thomas Dixon, W., Tuithof, H. H., Engels, H., Nelson, R. C., Gerety, B. M., Chezmar, J. L., and Den Boer, J. A. (1993). Keyhole method for accelerating imaging of contrast agent uptake. *Journal of Magnetic Resonance Imaging*, 3(4):671–675.
- Vogt, F., Eggebrecht, H., Laub, G., Kroeker, R., Schmidt, M., Barkhausen, J., and Ladd, S. (2007). High spatial and temporal resolution mra (twist) in acute aortic dissection. In *Proc. Int. Soc. Magn. Reson. Med*, volume 15, page 92.
- Williams, D. S., Detre, J. A., Leigh, J. S., and Koretsky, A. P. (1992). Magnetic resonance imaging of perfusion using spin inversion of arterial water. *Proceedings of the National Academy of Sciences*, 89(1):212–216.
- Wu, W.-C., Fernández-Seara, M., Detre, J. A., Wehrli, F. W., and Wang, J. (2007). A theoretical and experimental investigation of the tagging efficiency of pseudocontinuous arterial spin labeling. *Magnetic Resonance in Medicine: An Official Journal of the International Society for Magnetic Resonance in Medicine*, 58(5):1020–1027.
- Yankeelov, T. E., Luci, J. J., Lepage, M., Li, R., Debusk, L., Lin, P. C., Price, R. R., and Gore, J. C. (2005). Quantitative pharmacokinetic analysis of dce-mri data without an arterial input function: a reference region model. *Magnetic resonance imaging*, 23(4):519–529.
- Zahra, M. A., Hollingsworth, K. G., Sala, E., Lomas, D. J., and Tan, L. T. (2007). Dynamic contrast-enhanced mri as a predictor of tumour response to radiotherapy. *The lancet oncology*, 8(1):63–74.
- Zimmer, F. (2014). *Development of Arterial Spin Labeling Techniques for Quantitative Perfusion Measurements at 3 Tesla*. PhD thesis.
- Zöllner, F., Gaa, T., Zimmer, F., Ong, M., Riffel, P., Hausmann, D., Schoenberg, S., and Weis, M. (2016a). Quantitative perfusion imaging in magnetic resonance imaging. *Der Radiologe*, 56(2):113–123.
- Zöllner, F. G., Daab, M., Sourbron, S. P., Schad, L. R., Schoenberg, S. O., and Weisser, G. (2016b). An open source software for analysis of dynamic contrast enhanced magnetic resonance images: Ummperfusion revisited. *BMC medical imaging*, 16(1):7.
- Zwick, S., Brix, G., Tofts, P. S., Strecker, R., Kopp-Schneider, A., Laue, H., Semmler, W., and Kiessling, F. (2010). Simulation-based comparison of two approaches frequently used for dynamic contrast-enhanced mri. *European radiology*, 20(2):432–442.

List of Publications

Peer-Reviewed Journal Articles

T. Uhrig, W. Neumann, M. Malzacher, V. Kossmann, L. Schad and F. Zoellner, Risk assessment of copper containing contraceptives: The impact for women with implanted intrauterine devices during clinical MRI and CT examinations, *Eur Radiol*, 29 (6), pp.2812-2820, 2019.

T. Gaa, W. Neumann, S. Sudarski, U. Attenberger, S. Schoenberg, L. Schad and F. Zoellner, Comparison of perfusion models for quantitative T1 weighted DCE-MRI of rectal cancer, *Sci Rep-UK*, 7, p.12036, 2017.

T. Gaa, M. Reinhart, B. Hartmann, J. Jakubek, P. Soukup, O. Jaekel, and M. Martisikova, Visualization of air and metal inhomogeneities in phantoms irradiated by carbon ion beams using prompt secondary ions, *Physica Medica*, 2017.

P. Illert, B. Waengler, C. Waengler, F. Zoellner, **T. Uhrig**, S. Litau, M. Pretze and T. Roeder, Functionalizable composite nanoparticles as a dual MRI/CT contrast agent for medical imaging, *J. Appl. Polym. Sci*, 136 (19), p.47571 2019.

N. Paschke, W. Neumann, **T. Uhrig**, M. Winkler, E. Probst, M. Fatar, L. Schad and F. Zoellner, Influence of Gadolinium-Based Contrast Agents on Tissue Sodium Quantification in Sodium Magnetic Resonance Imaging, *Invest Radiol*, 53 (9), pp.555-562, 2018.

S. Sudarski, T. Henzler, T. Floss, **T. Gaa**, M. Meyer, H. Haubenreisser, S. Schoenberg and U. Attenberger, Variability and Reproducibility of 3rd-generation dual-source dynamic volume perfusion CT Parameters in Comparison to MR-perfusion Parameters in Rectal Cancer, *Sci Rep*, 8, p.6868, 2018.

F. Zoellner, **T. Gaa**, F. Zimmer, M. Ong, P. Riffel, D. Hausmann, S. Schoenberg and M. Weis, Quantitative Perfusionsbildgebung in der Magnetresonanztomographie, *Radiologe*, 56 (2), pp.113-123, 2016.

Conference Contributions

T. Uhrig, W. Neumann, N. Paschke, M. Siegfarth, A. Rothfuss, G. Kabelitz, K. Chung, A. Schnurr, L. Schad, J. Stallkamp and F. Zoellner. A multiparametric (^1H , ^{23}Na , diffusion, flow) anthropomorphic abdominal phantom for multimodal MR and CT imaging, in Proceedings of the 27th Annual Meeting of ISMRM, Montreal, Canada , p.1121, 2019.

T. Uhrig, S. Hubertus, J. Chacón-Caldera, L. Schad and F. Zoellner, Entwicklung eines Phantoms fuer DCE und ASL Messungen zur Quantifizierung von Perfusionsparametern, Proceedings 49. Jahrestagung der Deutschen Gesellschaft fuer Medizinische Physik (DGMP), Nuernberg, Germany , p.19, 2018.

T. Uhrig, C. Korth, S. Sudarski, L. Schad and F. Zoellner, Comparison of 2D and 3D dynamic contrast enhanced perfusion magnetic resonance imaging in patients with colorectal cancer, in Proceedings of the 26th Annual Meeting of ISMRM, Paris, France, p.3953, 2018.

T. Gaa, W. Neumann, M. Malzacher, L. Schad and F. Zoellner, Safety assessment of copper containing IUDs at 1.5T, 3T and 9.4T, in Proceedings of the 34th Annual Meeting of ESMRMB, Barcelona, Spain, p.258, 2017.

T. Gaa, L. Schad and F. Zoellner, Feasibility Study of a Dialyzer as a Multi-Compartment Perfusion Phantom for Microvascular Tracer Kinetic Modelling, in Proceedings of the 25th Annual Meeting of ISMRM, Hawaii, USA, p. 1922, 2017.

T. Gaa, S. Sudarski, L. Schad and F. Zoellner, Quantitative Perfusion Imaging in Rectal Cancer - Choice and Influence of the Arterial Input Function to Perfusion Parameters, in Proceedings of the 25th Annual Meeting of ISMRM, Hawaii, USA, p. 4382, 2017.

T. Gaa, L. Schad and F. Zoellner, Erstellung eines einfachen multimodalen Perfusionsphantoms zum Vergleich von Perfusionsparametern, in Schoenberg, Rose, Stallkamp, 2nd Image-Guided Intervention Conference, Mannheim, Germany, p.13, 2015.

T. Gaa, S. Sudarski, F. Lietzmann, L. Schad and F. Zoellner, Quantitative DCE-MRI of rectal cancer: influence of multiple blood supplies and its corresponding arterial input functions on perfusion parameters, in Proceedings of 32nd Annual Meeting ESMRMB, Edinburgh, UK, p.597, 2015.

T. Gaa, S. Sudarski, F. Lietzmann, L. Schad and F. Zoellner, Comparison of the two-compartment exchange model and the two-compartment uptake model in quantitative DCE-MRI of rectal cancer, in Proceedings of 32nd Annual Meeting ESMRMB, Edinburgh, UK, p.481, 2015.

T. Gaa, M. Reinhart, G. Arico, B. Hartmann, L. Opalka, J. Jakubek, S. Pospisil, O. Jaekel, and M. Martisikova, PO-0802: Visualization of inhomogeneities in a phantom irradiated by carbon ion beams using prompt secondary ions, in Proceedings of ESTRO 2014, Vienna, Austria, Radiotherapy and Oncology 111, p.60-61, 2014.

T. Gaa, F. Zoellner, F. Lietzmann and L. Schad, 3D BOLD of Kidney: Impact of High PAT Factors, in Proceedings of the 20th Annual Meeting of ISMRM, Melbourne, Australia, p.887, 2012.

I. Brumer, A. Adlung, W. Neumann, **T. Uhrig**, M. Malzacher, L. Schad and F. Zoellner. Novel pixel-based approach for artifact evaluation of passive implants in MRI validated on intrauterine devices at 3T. in Proceedings of the 36th Annual Meeting of ESMRMB, Rotterdam, Netherlands, p.395, 2019.

I. Brumer, J. Chacon-Caldera, S. Hubertus, **T. Uhrig**, M. Dziadosz, M. Barth, L. Schad and F. Zoellner. Investigating the existence of bias in ASL sequences: evaluation of perfusion measurements in phantom with 2D and 3D EPI pseudo-continuous ASL sequences, in Proceedings of the 36th Annual Meeting of ESMRMB, Rotterdam, Netherlands, p.149, 2019.

J. Chacon-Caldera, L. Hatz, A. Kruse, **T. Uhrig**, F. Zimmer, S. Hubertus, I. Hermann, L. Schad and F. Zoellner. Investigating Variability Sources in Kidney Perfusion Measurements with Pulsed ASL: A Phantom and In Vivo Pilot Study, in Proceedings of the 27th Annual Meeting of ISMRM, Montreal, Canada , p.5020, 2019.

I. Hermann, **T. Uhrig**, J. Chacon-Caldera, M. Akcakaya, L. Schad and S. Weingaertner. Flow dependency of blood T1 measurements assessed in a perfusion phantom and in vivo, Proc. SCMR , Bellevue, USA, pp.QF3-005, 2019.

I. Hermann, **T. Uhrig**, J. Chacon-Caldera, M. Akcakaya, L. Schad and S. Weingaertner. Effect of inflow and in-plane saturation in SASHA and MOLLI T1 and T1* maps in a perfusion phantom and in-vivo, in Proceedings of the 27th Annual Meeting of ISMRM, Montreal, Canada , p.1964, 2019.

N. Paschke, W. Neumann, **T. Gaa**, A. Neubauer, L. Schad and F. Zoellner. Influences of MRI Proton Contrast Agent on Sodium MRI at Clinical 3T Field Strengths. in Proceedings of the 25th Annual Meeting of ISMRM, Hawaii, USA, p. 2962, 2017.

Danke

In erster Linie möchte ich mich bei Prof. Dr. Lothar Schad für die Gelegenheit bedanken, meine Promotionsarbeit an seinem Lehrstuhl zu verfassen. Die Möglichkeit in seiner Gruppe zu arbeiten und sich weiter zu entwickeln sowie die Ermutigung zur Teilnahme an Fortbildungen und Konferenzen schätze ich sehr.

Darüber hinaus danke ich Prof. Peter Bachert für seine Bereitschaft, meine Dissertation zu begutachten.

Prof. Dr. Frank Zöllner danke ich für die umfassende Unterstützung und Betreuung dieser Arbeit.

Außerdem möchte ich mich für die Zusammenarbeit mit unseren klinischen Partnern an der Medizinischen Fakultät Mannheim bedanken, insbesondere bei Dr. med. Sonja Janssen von der Abteilung für Radiologie und Nuklearmedizin, für die Koordination der in vivo Messungen sowie deren medizinische Beurteilung.

Nadia Paschke, Simon Hubertus, Ruomin Hu und Sebastian Thomas danke ich für das Korrekturlesen dieser Arbeit. Die Diskussionen mit euch und Jorge Chacón Caldera, Irène Brumer, Wiebke Neumann und Matthias Malzacher haben während meiner Promotionszeit viele neue Ideen hervorgebracht.

Vielen Dank, Matze und Ede, für die Aufnahme in das Hochschul Kompetenzteam und Ruomin und Sebastian für die Aufrechterhaltung von eben diesem. Die Zusammenarbeit mit euch hat mir sehr viel Spaß bereitet.

Schließlich danke ich all meinen Kollegen am CKM, die mich über die letzten 5,5 Jahre begleitet haben. Es ist viel Wert jeden Morgen zu wissen, dass man auf der Arbeit liebe Menschen treffen wird. Danke für die schönen Arbeitstage aber auch die produktiven Kicker Pausen, lustigen Abende, Konferenzen und Urlaube. Aus vielen von euch sind mittlerweile gute Freunde geworden.

Insbesondere danke ich Wiebke, eine bessere Person zum Teilen des Büros, der Konferenz Hotelzimmer, der mehr oder weniger ernsthaften Gedanken zu Feminismus, Psychologie und dem Leben im Allgemeinen, der neuen Sporterfahrungen und des ein oder anderen winzigen Schlückchens nach Feierabend hätte ich mir nicht wünschen können.

Mein Studium wäre ein ganz anderes gewesen ohne den StammtischTM und Martin. Ich danke euch für die schöne und aufregende Zeit, die wir währenddessen mit physikalischen und nicht physikalischen Themen zusammen verbracht haben.

Mein herzlichster Dank geht an die Mädelsabendgruppe für das liebenswürdige und kontinuierliche aus der Physikbubble holen.

Den Uhrigs sowie meiner Familie, insbesondere Opa und Jonas vielen Dank, dass ihr immer für mich da wart, ohne euch wäre ich nicht zu der Person geworden, die ich heute bin.